Fermilab

FERMILAB-THESIS-1998-38

THE SEARCH FOR PHYSICS BEYOND THE STANDARD MODEL IN THE $b\bar{b}$ SPECTRUM OBSERVED IN TEVATRON PROTON-ANTIPROTON COLLISIONS

A Thesis

Submitted to the Faculty

of

Purdue University

by

Kara Dion Hoffman

In Partial Fulfillment of the

Requirements for the Degree

of

Doctor of Philosophy

August 1998

ACKNOWLEDGMENTS

The Ph.D. program is much like an apprenticeship. Where the textbooks leave off, the student must rely on the knowledge and experience of others more senior. Many of my collaborators have patiently answered my questions over the years. In particular I would like to thank my advisor, Daniela Bortoletto, for getting me involved with the CDF Collaboration, and for her guidance and support. I would also like to thank Robert Harris, my collaborator in the analysis presented here, and the conveners of the exotics group, John Conway, David Stuart, Henry Frisch, and Kaori Maeshima, who have given me valuable suggestions and advice. Many members of the SVXII group, especially Jeff Spalding, have also contributed to my professional development. I would also like to express my gratitude to Marcus McEllistrem, my mentor as an undergraduate, who convinced me that I had what it took to be a physicist.

Finally, I would like to thank my family: Mom, Erin, and R.J., for their love, support, and frequent phone calls, and all of the friends, both at Purdue and CDF, who have left me with many fond memories of my years in graduate school.

This work was supported by the U.S. Department of Energy and the Purdue Research Foundation.

TABLE OF CONTENTS

LIST OF TABLES

LIST OF FIGURES

Figure Page

Figure Page

Figure Page

ABSTRACT

Hoffman, Kara Dion, Ph.D., Purdue University, August 1998. The Search for Physics Beyond the Standard Model in the $b\bar{b}$ Spectrum Observed in Tevatron Proton-Antiproton Collisions. Major Professor: Daniela Bortoletto.

Many extensions have been proposed to the Standard Model of fundamental particles and interactions, therefore we have conducted a general search with the Collider Detector at Fermilab (CDF) for particles which would be expected to appear as a resonance in the $b\bar{b}$ mass spectrum produced in proton-antiproton collisions at a center-of-mass energy of $\sqrt{s} = 1.8$ TeV at the Fermilab Tevatron collider. We use 87.3 pb^{-1} of data collected from 1993-1995 during collider Run 1B to reconstruct the $b\bar{b}$ mass spectrum from 150 - 625 GeV/c^2. The spectrum is found to be in good agreement with simulations of direct $b\bar{b}$ production, and is therefore used to set limits on a variety of new phenomena. We present model independent upper limits on the cross section for resonances decaying with a natural width that is narrower than the CDF $b\bar{b}$ mass resolution, which excludes the color octet technirho predicted in walking technicolor theories between 350 and 440 GeV/c^2. In addition, we exclude topgluons, predicted in models of topcolor assisted technicolor, of width , $= 0.3M$ in the mass range $280 < M < 670$ GeV/c^2, of width , $= 0.5M$ in the mass range $340 < M < 640$ GeV/c^2, and of width , $= 0.7M$ in the mass range $375 < M < 560$ GeV/c^2.

"Nothing happens in contradiction to Nature,

Only in contradiction to what we know of it."

- Dana Scully, *The X-Files*

1. INTRODUCTION

1.1 The Standard Model

Our current understanding of the most fundamental particles found in nature and their interactions is based on the $SU(3)_c \otimes SU(2)_L \otimes U(1)_Y$ gauge invariant theory of the strong and electroweak interactions known as the *Standard Model* [2]. Since it was first proposed more than 25 years ago, the Standard Model has enjoyed many phenomenological successes. It is found to be in remarkable agreement with experimental measurements, and with the recent discovery of the top quark [3, 4], the constituents of matter predicted by the SM, which are divided by weak isospin into left-handed doublets and right-handed singlets of quarks,

$$\begin{pmatrix} u \\ d \end{pmatrix}_L \begin{pmatrix} c \\ s \end{pmatrix}_L \begin{pmatrix} t \\ b \end{pmatrix}_L \quad u_R \; d_R \; c_R \; s_R \; t_R \; b_R,$$

and leptons,

$$\begin{pmatrix} e \\ \nu_e \end{pmatrix}_L \begin{pmatrix} \mu \\ \nu_\mu \end{pmatrix}_L \begin{pmatrix} \tau \\ \nu_\tau \end{pmatrix}_L \quad e_R \; \mu_R \; \tau_R,$$

have all been observed, with the exception of the tau neutrino. These particles interact through the exchange of spin one gauge bosons, with the massless photon, γ, and the massive $W^{\pm}$ and Z^0 bosons mediating the electroweak interaction, and eight varieties of massless colored gluons mediating the strong interaction.

The nonzero masses of the $W^{\pm}$ and Z^0 tell us that the electroweak symmetry, $SU(2)_L \otimes U(1)_Y$, is a broken one. In addition, flavor symmetry must be broken to

provide the wide spectrum of fermion masses. The mechanism of electroweak and flavor symmetry breaking is unknown, and is one of the most tantalizing mysteries in particle physics today.

Electroweak symmetry breaking is accomplished in the Standard Model by introducing a weak doublet of scalar bosons

$$\phi = \frac{1}{\sqrt{2}} \begin{pmatrix} \omega_1 + i\omega_2 \\ h_0 + i\omega_0 \end{pmatrix} \quad \text{with potential} \quad V(\phi) = \lambda \left(\phi^\dagger \phi - \frac{1}{2} v^2 \right)^2 \tag{1.1}$$

which spontaneously breaks electroweak symmetry down to electromagnetism: $SU(2)_L \otimes U(1)_Y \to U(1)_Q$. The kinetic term of the Lagrangian:

$$(D_\mu \phi)^\dagger (D^\mu \phi) \tag{1.2}$$

where the covariant derivative is defined as

$$D_\mu = \partial_\mu + ig\,\mathbf{W}_\mu \cdot \mathbf{T} + i\frac{g'}{2} B_\mu Y \tag{1.3}$$

and $\mathbf{T}$ is the isospin operator, endows the heavy gauge bosons with mass. The mass of the $W^\pm$ field, $(W_1 \mp iW_2)/\sqrt{2}$, becomes

$$M_W^2 = g^2 v^2 / 4 \tag{1.4}$$

while the Z field, $Z = (gW_3 - g'B)/\sqrt{g^2 + g'^2}$, receives a mass of

$$M_Z^2 = (g^2 + g'^2) v^2 / 4 \tag{1.5}$$

and the photon field, $A = (g'W_3 + gB)/\sqrt{g^2 + g'^2}$, is a massless orthogonal combination. Thus, three of the four degrees of freedom introduced, one for each of the spin one bosons, $W^\pm$, Z^0, and γ, become the longitudinal components of the three massive gauge bosons, W^+, W^-, and Z^0. Defining the weak mixing angle θ_W as $\tan\theta_W = g'/g$ gives a simple mass relation for the heavy gauge bosons

$$M_W^2 / M_Z^2 = \cos^2 \theta_W \tag{1.6}$$

that has been experimentally tested to better than 1% accuracy. The remaining degree of freedom, h_0, is manifested as the Higgs Boson, H^0, a neutral spin zero particle. The Higgs also provides the fermion masses, m_f, through a coupling of the Higgs to the fermions of strength $gm_f/2M_W$. The physical Higgs Boson, however, has yet to be observed. Recent experimental searches set a lower limit of 77.5 GeV/c^2 [5] on the Higgs mass.

While the existence of the scalar Higgs boson would, in fact, solve the problem of the $W^{\pm}$ and Z^0 masses, it is possible that the Standard Model may just be a low energy manifestation of a more fundamental theory. The minimal Standard Model contains 19 arbitrary parameters, including the fermion masses, the coupling parameters, α_s, α_{EM}, and the mixing angles. It is hoped that a more fundamental theory would have fewer degrees of freedom. The Standard Model does not encompass gravity, nor does it explain why there are three generations of quarks and leptons. In addition to it's lack of predictive power, there is a more compelling (though not fatal) complaint about the Standard Model known as the "gauge hierarchy problem".

In the classical approximation, the mass of the Higgs scalar will be proportional to the vacuum expectation value, $v = (G_F\sqrt{2})^{-\frac{1}{2}} = 246$ GeV, that breaks electroweak symmetry, and the Higgs mass parameter μ can be adjusted to give the appropriate value of M_H. Radiative corrections from fermion, scalar boson, and gauge boson loops, however, will contribute to the Higgs mass renormalization [6] :

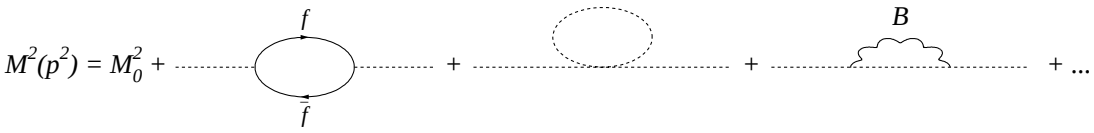

(1.7)

where the loop integrals diverge quadratically as:

$$Cg_i^2 \int_{p^2}^{\Lambda^2} dk^2 \tag{1.8}$$

as the loop momentum increases. Such integrals are only well behaved if the range of integration is limited. When the Standard Model is embedded into the framework of physics at a scale much higher than the electroweak scale ($\Lambda \sim 10^3$GeV), such as physics at the Planck or Grand Unification scale ($\Lambda \sim 10^{15} - 10^{19}$GeV), Equation 1.7 becomes

$$\delta m_H^2 \sim \Lambda^2(-c_1 g_f^2 + c_2 g_s^2 + \cdots) \tag{1.9}$$

introducing an instability of order $\delta m^2 \sim \Lambda^2$. Thus the the mass scales of the two theories could not be reconciled without a precise fine-tuning of the parameters in each of the theories, at each stage of perturbation. This is the gauge hierarchy problem.

In conclusion, it should be noted that the mass of a particle will not be larger than the associated symmetry breaking scale. If a larger symmetry breaking scale exists, the associated particles would have correspondingly larger masses, and thus would not be observed in the particle spectrum at presently attainable energies, making the particles discussed in this section "the tip of the iceberg". So perhaps the most compelling reason to search for physics beyond the Standard Model is simply that we have no reason to believe that symmetry breaking could not occur at higher scales.

1.2 Physics Beyond the Standard Model

Many ideas for the extension of the Standard Model are being studied in pursuit of a more predictive, and in some cases, a more unified theory of the fundamental particles and their interactions. A few of these are:

- Compositeness: Maybe the fundamental particles discussed above aren't so fundamental after all. It is possible that quarks or leptons have a substructure that is not apparent at presently attainable energies.
- Supersymmetry: A class of models where a boson-fermion symmetry is introduced such that their contributions to Equation 1.7 would cancel. This would increase the number of Higgs doublets to two in the minimal model, and the spectrum of fundamental particles would be doubled.
- Technicolor: A class of models developed in analogy to the microscopic BCS theory of the superconducting phase transition where condensates of *technifermions*, like Cooper pairs, break the symmetry of the Lagrangian. The technifermions interact through the technicolor force which behaves like QCD.
- Grand Unified Theories : Theories which unify the strong and electroweak interactions in one simple gauge group, $\mathcal{G}$, at high energies ($> 10^{15}$ GeV).

The diversity of these proposals is a consequence of the fact that, until more experimental evidence is available, it is impossible to guess what form physics will assume at higher energies. Therefore it is useful to perform a model independent search.

Many new particles are expected to have a large branching fraction to $b\bar{b}$, thus, by fitting the b-tagged dijet mass spectrum to a mass resonance superimposed on a smooth background, many new phenomena may be sought in a single distribution. Here we present a search for resonances in the $b\bar{b}$ spectrum using 87.3 pb^{-1} of data taken by the Collider Detector at Fermilab (CDF) from 1993-1995 during Run 1B of the Tevatron collider. A few of the theories which could produce $b\bar{b}$ resonances are introduced below, along with the phenomenology of the resonances we seek.

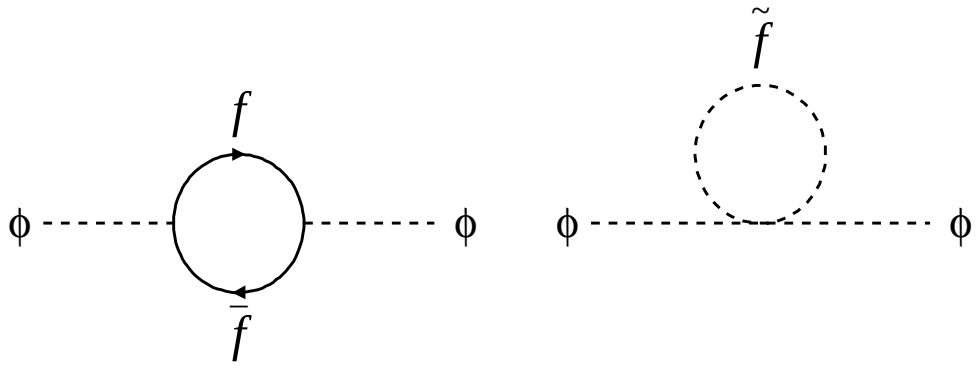

Figure 1.1

Contribution of a fermion and it's bosonic superpartner to the Higgs self energy.

1.3 Supersymmetry

One solution to the gauge hierarchy problem is to introduce a spin $\frac{1}{2}$ generator which changes the angular momentum of a particle by $\frac{1}{2}$:

$$Q\,|\text{boson}>=|\text{fermion}> \qquad Q\,|\text{fermion}>=|\text{boson}> \tag{1.10}$$

changing bosons to fermions and fermions to bosons. This approach, taken in a class of models known as Supersymmetry, doubles the number of particles by predicting that every known particle will have a superpartner with identical mass and identical quantum numbers except for a difference of $\frac{1}{2}$ unit in spin. If the boson and fermion coupling constants are equal, $g_f = g_s$, the contribution to the Higgs self energy of fermion and boson loops , such as the ones shown in Figure 1.1, are exactly canceled, since fermion loops contribute a negative sign to the Higgs mass correction [7]:

$$\delta m_H^2 \sim g_f^2(\Lambda^2 + m_f^2) - g_s^2(\Lambda^2 + m_s^2) \sim g_f^2(m_s^2 - m_f^2). \tag{1.11}$$

It is apparent, however, that Supersymmetry is a broken symmetry, as no superpartners with identical mass to the known Standard Model particles have been observed,

however, the radiative corrections to the Higgs mass remain manageable as long as the mass splitting between the fermion and scalar is not larger than:

$$|m_s^2 - m_f^2| \leq \mathcal{O}(1 \text{ TeV}^2) \tag{1.12}$$

Finally, it should be noted that Supersymmetry, if treated as a local gauge symmetry, has the added advantage of being easily coupled to the theory of gravity, since the generator of Supersymmetry will give a space-time transformation when applied twice to any fermion or boson field [8].

The Minimal Supersymmetric Model requires two Higgs doublets, with precisely opposite $U(1)$ quantum numbers to cancel the gauge anomalies introduced by the *higgsinos*, the fermionic superpartners of the Higgs. The two Higgs doublets are also necessary to provide the up and down quark masses. Supersymmetry, therefore, has a rich phenomenology of Higgs scalars. The particle spectrum predicted by the Minimal Supersymmetric Model is shown in Table 1.1.

Supersymmetry must introduce a new symmetry called R-symmetry to forbid lepton and baryon number violating interactions which could mediate proton decay (which, of course, has not been experimentally observed, with current limits setting the proton's lifetime at no less than 1.6×10^{25} years [9]). Most supersymmetric models require the conservation of the associated multiplicative quantum number, R-parity, defined as

$$R \equiv (-1)^{3(B-L)+2S} \tag{1.13}$$

for a particle of spin S with baryon number B and lepton number L. Standard Model particles thus carry even R-parity while its corresponding superpartners carry odd R-parity. This has far-ranging implications on the phenomenology of the production and decay of supersymmetric partners [8]. First, superpartners can only be pair-produced from non-SUSY particles. Second, the lightest supersymmetric particle

Particle		**Superpartner**	
quarks, spin: $\frac{1}{2}$	$q_L,\ q_R$	squarks, spin: 0	$\tilde{q}_L,\ \tilde{q}_R$
leptons, spin: $\frac{1}{2}$	$\ell_L,\ \ell_R$; $\nu_{\ell\,R}$	sleptons, spin: 0	$\tilde{\ell}_L,\ \tilde{\ell}_R$; $\tilde{\nu}_{\ell\,L}$
gauge bosons, spin: 1	g; γ; Z; $W^{\pm}$	gauginos, spin: $\frac{1}{2}$	gluino $\tilde{g}$; photino $\tilde{\gamma}$; zino $\tilde{Z}$; wino $\tilde{W^{\pm}}$
Higgs, spin: 0	$\begin{pmatrix} H_1^0 \\ H_1^- \end{pmatrix}$ $\begin{pmatrix} H_2^+ \\ H_2^0 \end{pmatrix}$	Shiggs, spin: $\frac{1}{2}$	$\begin{pmatrix} \tilde{H}_1^0 \\ \tilde{H}_1^- \end{pmatrix}$ $\begin{pmatrix} \tilde{H}_2^+ \\ \tilde{H}_2^0 \end{pmatrix}$

Table 1.1

The particle spectrum predicted by the Minimal Supersymmetric Model.

(LSP) will be stable, since there must remain at least one particle with odd R-parity at the end of a decay chain initiated by a SUSY particle. The LSP will therefore escape detection, making an apparent momentum imbalance a classic signature for Supersymmetry.

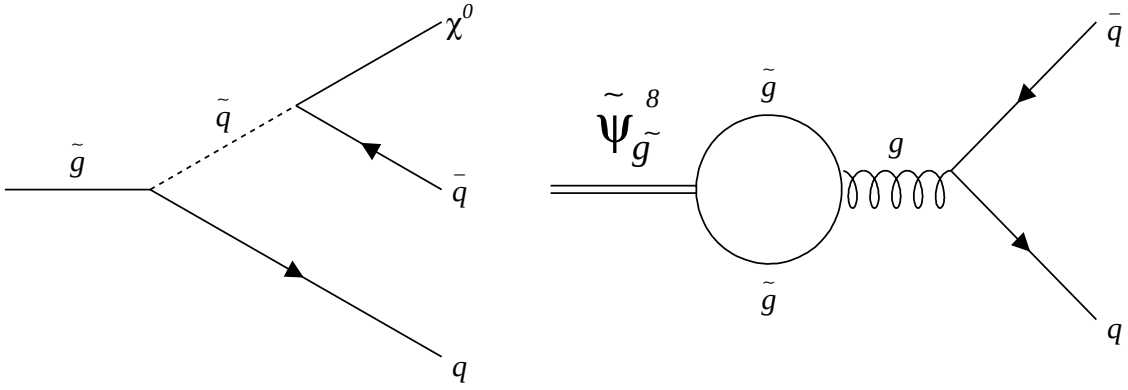

Figure 1.2

Diagrams of gluino decays. If $m_{\tilde{g}} > m_{\tilde{q}}$, the decay chain of the gluino will include the LSP, a neutralino (χ^0) (left). If $m_{\tilde{q}} > m_{\tilde{g}}$, the gluinos will live long enough to form a bound state which decay via gluino annihilation (right).

1.3.1 Vector Gluinonium

In R-parity conserving Supersymmetry models, if the mass of the bosonic superpartner of the quark, called a *squark*, is lighter than the mass of the fermionic superpartner of the gluon, or *gluino*, the gluino will decay strongly to a squark and an antiquark, with the lightest supersymmetric particle appearing as a final decay product (see Figure 1.2, left). If the squark mass is heavier than the gluino mass, on the other hand, the gluino can only decay weakly. This makes the direct detection of the gluino difficult, however, since the gluino, like the gluon, has no basic electroweak couplings, it may live long enough to form a gluino-gluino bound state (as shown in Figure 1.2) which could couple via a gluon to dijets, making it possible to observe the gluino indirectly. The antisymmetric color-octet state of gluinonium could be produced at the Tevatron via $q\bar{q}$ annihilation and would decay

predominantly via gluino annihilation with a width of [10]

$$, (\psi_{\tilde{g}}^{8} \rightarrow q\bar{q}) \approx N_q \frac{27}{64} \alpha_s^5 M \tag{1.14}$$

where M is the gluinonium mass ($M \approx 2m_{\tilde{g}}$) and N_q is the number of quark flavors to which gluinonium is kinematically allowed to decay. This has the advantage of yielding a relatively precise determination of the gluino mass, since the gluinos annihilate leaving no need for an R-parity conserving LSP in the decay chain that will escape undetected. In the case where the final state jets are nearly back-to-back the ratio of heavy quark decays (c, b, t) to light quark decays is 3:2, making $b\bar{b}$ a promising decay channel to investigate.

1.3.2 Current Limits on Gluinos

The most stringent limits on the gluino mass to date come from a search by the CDF collaboration for a momentum imbalance signature that assumes a decay to the lightest supersymmetric particle [11]. A summary of the current limits in the squark-gluino mass plane is shown in Figure 1.3. Note that the limits are much weaker for the case where the squark mass is greater than the gluino mass, which is the region covered by gluinonium searches.

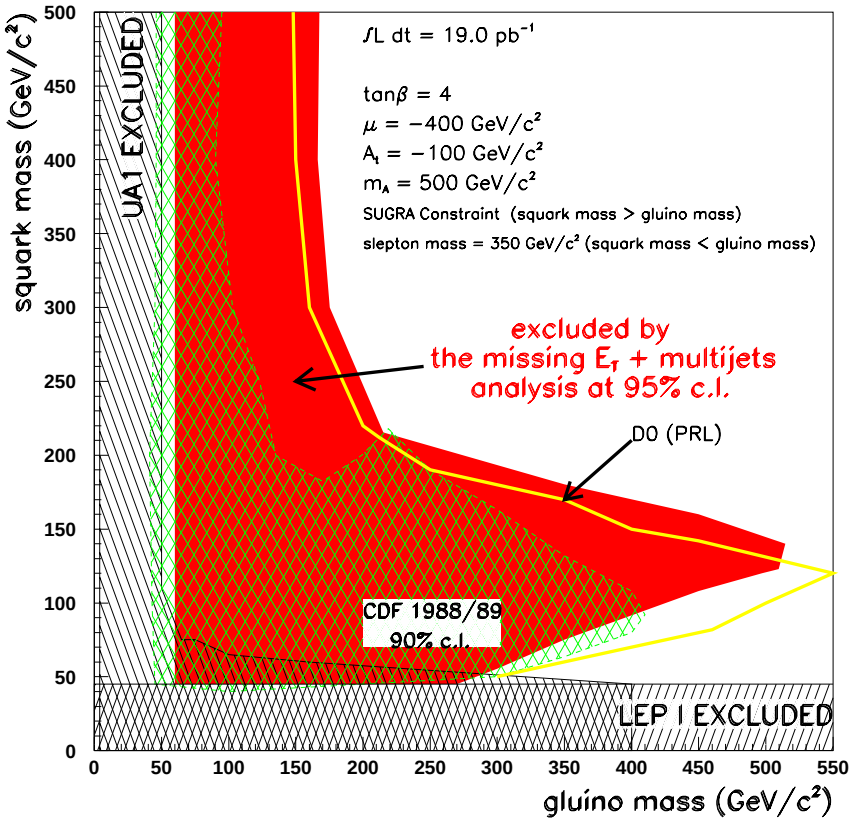

Figure 1.3

Summary of 95% confidence level exclusion regions of the squark-gluino mass plane from various experiments.

1.4 Dynamical Symmetry Breaking: Technicolor

An alternative to Higgs scalars is suggested by the observation that the strong dynamics of QCD is all that is needed to break electroweak symmetry and endow the gauge bosons with mass. This approach was suggested by the BCS theory of superconductivity, where the order parameter (non-vanishing vacuum expectation value) is dynamically generated by the formation of scalar bound states of electrons, known as "Cooper pairs", which form a low temperature condensate of bosons. Such a condensate of fermions and antifermions could be used to break electroweak symmetry and generate nonzero gauge boson masses. To see this, imagine the world as described in Section 1.1, but with only one generation of quarks, and without the electroweak interactions. The quarks, if assumed to be massless, exhibit a chiral symmetry [12],

$$\mathcal{G} = SU(2)_L \otimes SU(2)_R. \tag{1.15}$$

However, in the ground state of QCD, this symmetry is spontaneously broken by the strong interactions of the quarks. Suppose two quarks which have the combined quantum numbers of the vacuum are attracted at long distances by gluon exchange. The potential energy of the ground state can be lowered by producing additional $q\bar{q}$ pairs, which fill up the ground state. This quark-antiquark condensate acquires a nonzero vacuum expectation value [13]:

$$< 0 \mid q\bar{q} \mid 0 > \sim \Lambda_{QCD}^3 \tag{1.16}$$

which breaks the left-right symmetry and leaves the ground state only symmetric under the subgroup $\mathcal{G}' = SU(2)_{isospin}$. The ground state is therefore less symmetric than the Lagrangian. Goldstone's theorem states that massless scalars appear when spontaneous symmetry breaking occurs. Note that when only the first generation of quarks is considered, the pions, $\pi^{\pm}$ and π^0, have the quantum numbers of the

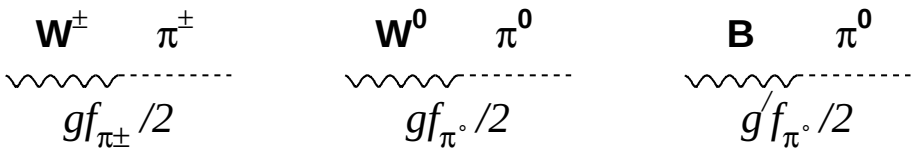

Figure 1.4

Diagrams in which gauge bosons turn into Goldstone bosons.

Goldstone bosons. The broken generators give rise to axial-vector currents, j_i, which couple to the massless goldstone bosons, the pions, with strength [14]:

$$< 0 \mid j^{\mu}_{5a} \mid \pi_b > = i f_{\pi} q^{\mu} \delta_{ab} \tag{1.17}$$

where

$$j^{\mu}_{5a} = f_{\pi} \partial^{\mu} \pi_a = \bar{q} \gamma_{\mu} \gamma_5 \frac{\tau^a}{2} q, \tag{1.18}$$

τ^a are the Pauli matrices, $f_{\pi} = 93$ MeV is the pion decay constant, and q is the momentum transfer.

If the electroweak interaction, without the Higgs scalar, is introduced as a perturbation, the electroweak gauge bosons couple to the axial currents, as shown in Figure 1.4. As in the Higgs mechanism, the Goldstone bosons (here pions) do not appear in the physical spectrum but become the longitudinal components of the electroweak gauge bosons, endowing them with masses on the order of $\sim g f_{\pi}$. To

see this, consider the propagator for the $W^{\pm}$ [14]:

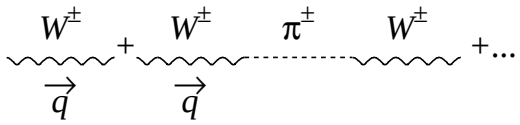

(1.19)

Summing the diagrams we get [14]:

$$\begin{aligned} \text{full propagator} &= \tfrac{1}{p^2} + \tfrac{1}{p^2}(gf_{\pi^\pm}/2)^2 \tfrac{1}{p^2} + \cdots \\ &= \tfrac{1}{p^2}\left[1 + \tfrac{(gf_{\pi^\pm}/2)^2}{p^2} + \cdots\right] \\ &= \tfrac{1}{p^2}\left[1 - \tfrac{(gf_{\pi^\pm}/2)^2}{p^2}\right]^{-1} \\ &= \tfrac{1}{p^2 - (gf_{\pi^\pm}/2)^2} \end{aligned} \tag{1.20}$$

Thus the $W^{\pm}$ boson thus acquires a mass of

$$m_W^2 = (gf_{\pi^\pm}/2)^2. \tag{1.21}$$

A similar calculation for the W^0 and B propagators which include mixing gives the mass matrix:

$$\begin{pmatrix} M_{W^0}^2 & M_{W^0\,B}^2 \\ M_{W^0\,B}^2 & M_{B\,B}^2 \end{pmatrix} = \frac{f_{\pi^0}^2}{4} \begin{pmatrix} g^2 & gg' \\ gg' & g'^2 \end{pmatrix} \tag{1.22}$$

The matrix eigenvalues give the massless photon and the Z^0 of mass

$$m_Z^2 = (g + g'^2) f_{\pi^0}^2/4 \tag{1.23}$$

Thus the $W^{\pm}$ and Z^0 masses are related by

$$\frac{m_W}{m_Z} = \frac{f_{\pi^\pm}}{f_{\pi^0}} \cos\theta_W \tag{1.24}$$

which is exactly the relation given in Equation 1.6 if $f_{\pi^\pm} = f_{\pi^0}$, which is guaranteed by isospin symmetry. Although this model is successful in recovering the mass relation, $m_W/m_Z = cos\,\theta_W$, the masses are scaled down by a factor of ~ 2600.

We can conclude, then, that QCD is not strong enough to account for the $W^\pm$ and Z^0 masses, but the mechanism, known as *dynamical symmetry breaking*, seems plausible. It has been proposed that a new, asymptotically free interaction called *Technicolor* that mimics QCD could account for the gauge boson masses if its interactions become strong at an energy scale that is related to Λ_{QCD} by:

$$\frac{\Lambda_{TC}}{\Lambda_{QCD}} \sim 2600. \tag{1.25}$$

Electroweak doublets of massless technifermions would feel the technicolor force, and at high energies, where α_{TC} becomes strong, technifermion condensates would form, breaking the chiral technicolor flavor group

$$\mathcal{G}_{TC} = SU(2N)_{LEFT} \otimes SU(2N)_{RIGHT} \tag{1.26}$$

down to $SU(2N)$, where N is the number of technifermion generations. The electroweak bosons acquire their masses as described in the QCD scenario, only now their masses are proportional to the technipion (π_T) decay constant, F_π, which is chosen to be on the order of the weak scale (~ 246 GeV).

This model succeeds in yielding the appropriate masses for the electroweak bosons while avoiding the arbitrary parameters that were necessary in the Higgs model discussed in Section 1.1, but the problem of fermion masses still remains. In the spirit of the above discussion, this would suggest that more interactions are needed to break the flavor symmetries of quarks, leptons, and technifermions. If we embed all of these particles into a larger gauge group, G_{ETC}, which breaks down to the technicolor group, G_{TC}, at high energy scales [12],

$$\Lambda_{ETC} \gg \Lambda_{TC}, \tag{1.27}$$

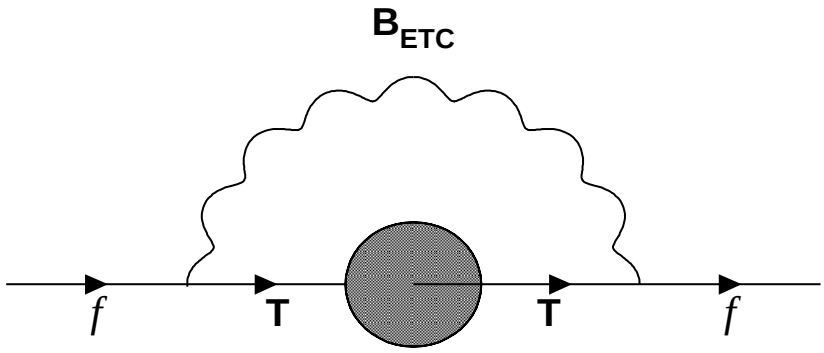

Figure 1.5

The generation of fermion masses through the exchange of an extended technicolor boson. The filled area represents a techniquark condensate. The exchange of an extended technicolor boson couples the fermions to the techniquarks, inducing fermion masses.

the resulting massive gauge bosons would mediate transitions from technicolored to non-technicolored particles, in an interaction known as *extended technicolor*. These models are still incomplete, since it is not known what interactions are responsible for breaking extended technicolor, but the boson exchange would generate quark and lepton masses on the order of [15],

$$m \sim \frac{\Lambda_{TC}^3}{\Lambda_{ETC}^2}. \tag{1.28}$$

as shown in Figure 1.5.

Unfortunately, even this model runs into immediate problems. Extended technicolor bosons, in addition to coupling technifermions to technifermions, and fermions to technifermions, also couples fermions to fermions, and could therefore mediate transitions between fermions of different flavors. Unless $\Lambda_{ETC} \geq 500$ TeV, this leads to large flavor-changing neutral currents that are not observed at present energy

scales. The large Λ_{ETC} needed to suppress flavor-changing neutral currents would result in quark and lepton masses that are too small according to Equation 1.28. Some models of "walking technicolor" attempt to minimize this problem by requiring that the gauge coupling α_{TC}, runs slowly, or "walks", above the energy scale Λ_{TC}, such that flavor-changing neutral currents are no longer a concern [16], while the quark masses are maintained. The wide spectrum of fermion masses provide another challenge. This leads to the implementation "multi-scale" extended technicolor models, which instead of breaking down to the technicolor group at a discrete energy, breaks over a hierarchy of scales to reflect the hierarchy of fermion masses.

A number of models of technicolor have been proposed and, although they are all too simple to describe the world as we know it, they are useful in predicting the observable effects that would be typical of such an interaction. For example, since the longitudinal degrees of freedom that give the Z^0, and $W^{\pm}$ their masses in minimal technicolor models are composite technihadrons, the Z^0, and $W^{\pm}$ are expected to have a strongly interacting component. Since technicolor is similar in character to QCD, there will be a spectrum of technihadrons that can be inferred from the familiar spectrum of ordinary hadrons, for example, technirhos, $\rho_T^+, \rho_T^0, \rho_T^-$, techniomega, ω_T, and technieta, η_T. If this model is extended to include a doublet of technileptons, N and E, which also feel the techniforce, there would exist $Q\bar{L}$ bound states known as leptoquarks [15]. Note that if the techniquarks are color triplets, the leptoquarks would not be color neutral, but would also be color triplets, and technimesons, $Q\bar{Q}$, that are color octets could also exist.

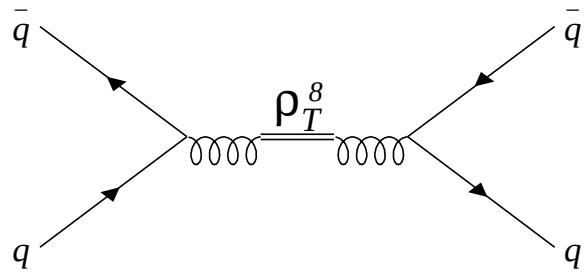

Figure 1.6

The production and decay of a color octet technirho via its coupling to an intermediate gluon.

1.4.1 Color Octet Technirho

In a specific model of multi-scale Walking Technicolor [17, 1], based on the gauge group

$$\mathcal{G}_{ETC} = SU(N_{ETC})_1 \otimes SU(N_{ETC})_2 \tag{1.29}$$

the spectrum of technifermions includes one doublet of color singlet technifermions, $\Psi = (\Psi_U, \Psi_D)$, one doublet of color triplet techniquarks, $Q = (U, D)$, and N_L doublets of color singlet technileptons, $L_i = (N_i, E_i), i = 1, ..., N_L$, providing a rich phenomenology of technimesons. Since these technifermions carry ordinary color, there will be a spectrum of color octet technirhos with wavefunctions:

$$\begin{aligned} \rho_T^+ &\qquad |U_\alpha \overline{D}_\beta > \\ \rho_T^0 &\qquad |U_\alpha \overline{U}_\beta - D_\alpha \overline{D}_\beta > \\ \rho_T^- &\qquad |D_\beta \overline{U}_\alpha > \\ \rho_T^{0'} &\qquad |U_\alpha \overline{U}_\beta + D_\alpha \overline{D}_\beta > \end{aligned} \tag{1.30}$$

that will be strongly produced at hadron colliders at rates on the order of $\mathcal{O}(\alpha_{QCD}^2)$. Because a hierarchy of technifermion chiral symmetry breaking is employed, the technimesons associated with the lightest scales may be within discovery reach of the Tevatron. The walking scale introduced to suppress flavor-changing neutral currents will enhance the mass of the technipions relative to the technirho, which may kinematically close the decay mode $\rho_T \to \pi_T \pi_T$ leading to an appreciable branching fraction to quark-antiquark, and two gluon final states. Finally, the large mass splitting between the U and D techniquarks required to produce the observed mass splitting between the t and b quarks suggest that the ρ_T's are likely appear as well-separated, ideally mixed narrow resonances in the dijet spectrum. Furthermore, the $b\bar{b}$ spectrum will have a higher signal to background than the dijet spectrum, as shown in Figure 1.7.

The color octet technirho would be produced in hadron collision via its coupling to gluons, as shown in Figure 1.6. The width of the ρ_T^8 would be narrow

$$, = \left(1 + \frac{5}{3}\right) \cdot \frac{\alpha_s^2}{\alpha_{\rho_T}} M_{\rho_T^8} \approx .02 M_{\rho_T^8} \tag{1.31}$$

where

$$\alpha_{\rho_T} \equiv \frac{g_{\rho_T}^2}{4\pi} \cong 2.97 \left(\frac{3}{N_{TC}}\right) \tag{1.32}$$

N_{TC} is the number of technicolors and the $\rho_T \to \pi_T \pi_T$ decay constant is assumed to be scaled from the decay constant for $\rho \to \pi\pi$ in QCD.

1.4.2 Previous Technicolor Searches

Two previous searches for technicolor have been performed at CDF. The first search uses a technique to similar the one presented in this thesis to search for particles decaying to common dijets [18]. As shown in Figure 1.7, the color octet technirho would produce a resonance in the dijet channel. The signal to background

FIGURE 3

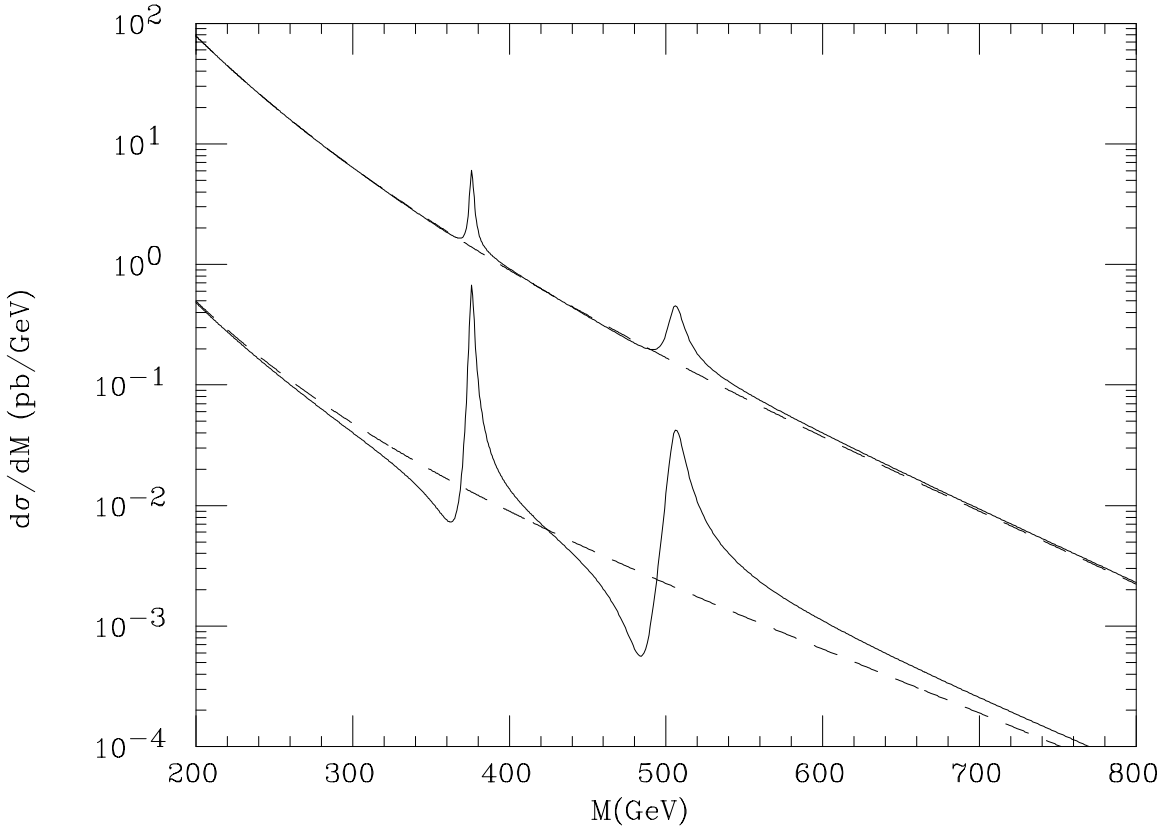

Figure 1.7

Technirho resonances in the dijet mass spectrum (solid line, top), and the $b\bar{b}$ mass spectrum (solid line, bottom) in $p\bar{p}$ collisions at $\sqrt{s} = 1800$ GeV. The dashed lines show the expected background. Taken from Reference [1].

would be smaller for a dijet signal, but dijets are copiously produced in Tevatron collisions and are reconstructed with nearly 100% efficiency, therefore, that search was able to exclude color-octet technirhos between 260 and 480 GeV/c^2 as shown in Figure 1.8 (left). The second analysis sought a color-singlet technirho that would decay to a W plus a technipion. The search looked for a signature of two heavy-flavor

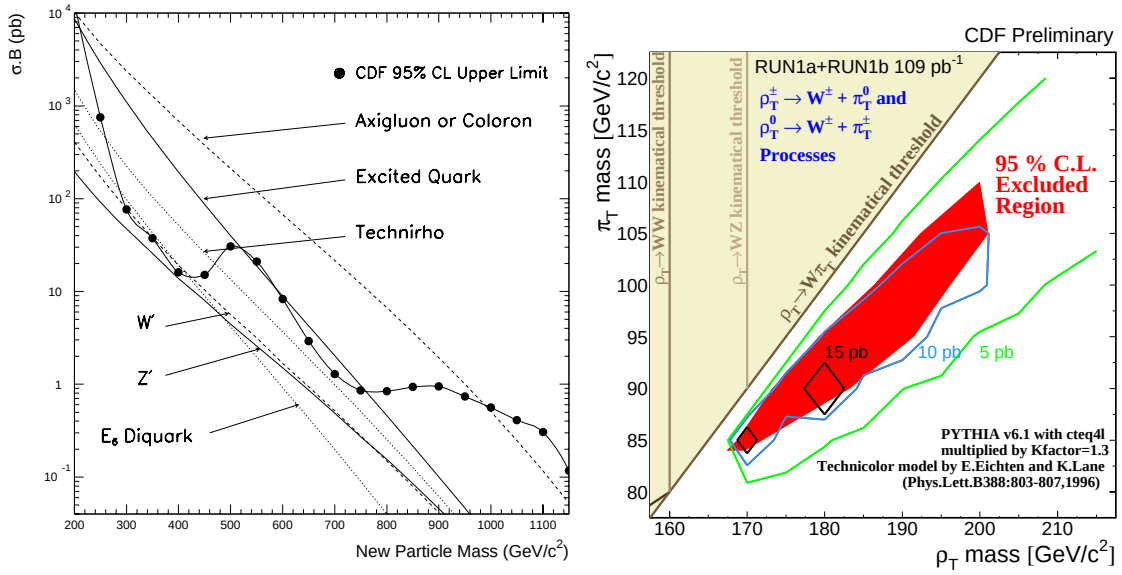

Figure 1.8

Previous CDF limits on Technicolor. The limit shown on the left is for a color-octet technirho in the generic dijet channel that assumes the decay $\rho_T \to \pi_T \pi_T$ decay channel is closed. The limit shown on the right in the technirho-technipion mass plane in the $W + b$-jet channel is for a color singlet technirho.

jets from the decay of the technipion, produced in association with a semileptonic W decay [19]. The limits from this search depend on the relative mass of the technirho and the technipion and are shown in the technirho, technipion mass plane in Figure 1.8 (right).

1.5 Top and Electroweak Symmetry Breaking: Topcolor

The top quark has recently been discovered, and with a mass of 175.9 ± 6.9 GeV/c^2 [20], it has the largest mass of any known fundamental particle (see Table 1.2), and it is the only fermion to have a mass on the order of the electroweak symmetry breaking scale. Since particles are thought to acquire their masses through

their coupling to the messenger of electroweak symmetry breaking, top is the most strongly coupled to the EWSB physics, and may prove a useful subject in studies of the dynamics of EWSB. This suggests new models of physics which intimately ties the third generation to electroweak symmetry breaking.

Models of "Topcolor" and "Topcolor Assisted Technicolor" employ a dynamical condensate to generate the largest component of the top mass, with Technicolor or a Higgs sector contributing a smaller component. The dynamics of Topcolor is described by [21]

$$SU(3)_1 \otimes SU(3)_2 \otimes U(1)_{Y_1} \otimes U(1)_{Y_2} \otimes SU(2)_L \tag{1.33}$$

where the third generation transforms under $SU(3)_1 \otimes U(1)_{Y_1}$ and the first two generations transform under a separate group, $SU(3)_2 \otimes U(1)_{Y_2}$. This breaks down to

$$SU(3)_{QCD} \otimes U(1)_{EM} \tag{1.34}$$

at ~ 1 TeV. Above this scale $SU(3)_1 \otimes U(1)_{Y_1}$ couplings are strong while $SU(3)_2 \otimes U(1)_{Y_2}$ are weak. The $U(1)$ symmetry accounts for the large mass difference between the t and b quarks.

1.5.1 The Topcolor Bosons: Topgluons and the Topcolor Z'

The particle manifestation of topcolor dynamics includes the topgluon, g_T, a new

Quarks				**Leptons**				**Bosons**	
u	$0.0015 - 0.005$	d	$0.003 - 0.009$	e	0.00051	ν_e	~ 0	$W^{\pm}$	80.4
c	$1.1 - 1.4$	s	$0.06 - .17$	μ	0.106	ν_μ	~ 0	Z^0	91.2
t	**176**	b	4.1 -4.4	τ	1.778	ν_τ	~ 0	γ	0

Table 1.2

The masses of the known particles in GeV/c^2.

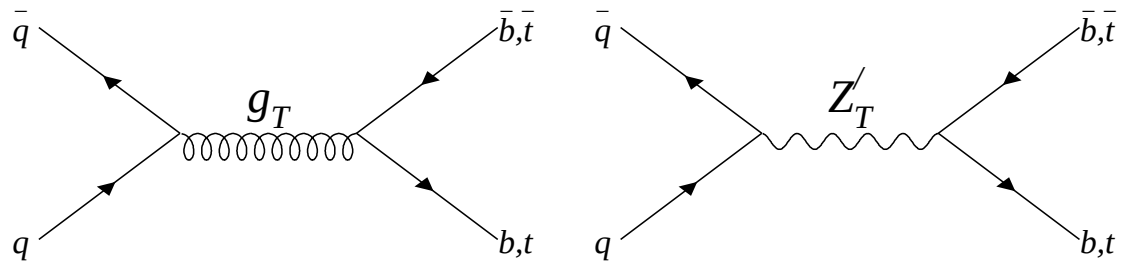

Figure 1.9

Feynman diagrams for Topcolor particles, the topgluon (left), and the Topcolor Z' (right).

vector boson that couples preferentially to the third generation, and the Topcolor Z', a new neutral gauge boson resulting from the $U(1)$ symmetry added in Topcolor models to maintain the large mass splitting between the top and bottom quarks. The topgluon would be produced in hadron colliders via a small coupling to the light quarks, and would decay preferentially to third generation quarks. The sub-process cross section for $q\bar{q} \to b\bar{b}$ from a topgluon resonance superimposed on the QCD $b\bar{b}$ spectrum is given by [22]

$$\frac{d\hat{\sigma}}{d\hat{t}} = \frac{2\pi\alpha_s^2}{9\hat{s}^2}(1-\cos^2\theta^*)\left|1-\frac{\hat{s}}{\hat{s}-M^2+i\sqrt{\hat{s}},}\right|^2 \tag{1.35}$$

for a topgluon of mass M and width , given by

$$, = \frac{\alpha_s M}{6}\left[4\tan^2\theta+\cot^2\theta\left(1+\beta_t\left(1-\frac{m_t^2}{M^2}\right)\right)\right] \tag{1.36}$$

where α_s is the strong coupling, $\hat{s}$ and $\hat{t}$ are subprocess Mandelstam variables, θ is the mixing angle between $SU(3)_1$ and $SU(3)_2$, θ^* is the scattering angle between the bottom quark and the initial state quark in the center of mass frame, $\beta_t = \sqrt{1-4m_t^2/M^2}$, and m_t is the top quark mass. In Equation 1.35, the 1 inside the

square brackets gives the contribution to the cross section from $q\bar{q} \to g \to b\bar{b}$, while the other term is the contribution from topgluon production. The two processes will interfere constructively below the topgluon mass peak and destructively above the topgluon mass peak. In order to make the top quark heavy, topcolor requires $\cot^2\theta \gg 1$.

The $U(1)$ symmetry added in topcolor models to provide the large mass splitting between the top and bottom quarks will give rise to the topcolor Z', a new heavy gauge boson which may couple preferentially to the third generation. The Z' is expected to be heavy and produce high E_T central jets.

1.5.2 Constraints on Topcolor-Assisted Technicolor

Although there have been no previous direct searches for Topcolor, models that call for a Z' which couples strongly to first and second generation fermions, as well as the third in order to achieve generational mixing (in contrast to the model we seek here, where the Z' couples preferentially to the third generation) would have an impact on the distribution of high invariant mass dilepton and dijets. Some (very model dependent) constraints on the Topcolor Z' can therefore be inferred from existing measurements of the Drell-Yan dilepton pair production cross-section [23], the dijet angular distribution [24], and the dijet production cross section [25] with CDF data. The most stringent limit comes from Drell-Yan data, which constrains $\alpha_{Z'}/M^2_{Z'}$ to < 0.021 TeV^{-2} which requires that either $M_{Z'} > 4$ TeV or $\alpha_{Z'} \ll 1$ [26] where $\alpha_{Z'} = gZ'/4\pi$.

1.6 Higher Symmetries

It is commonly believed that the Standard Model gauge symmetry is a low energy manifestation of a much simpler gauge group that unifies the strong and electroweak interactions at some very high energy scale, $E > E_{GUT}$. One prediction of GUT models that can be tested experimentally is that the proton has a finite lifetime. Current experimental limits on proton decay therefore set the GUT scale at $E_{GUT} > 10^{15}$ GeV. Another prediction of GUT models is that the running couplings of the Standard Model will become equal at the GUT scale. The lowest rank simple gauge group that can accommodate the Standard Model is $\mathcal{G} = SU(5)$, which predicts four neutral gauge bosons, the number of neutral gauge bosons in the Standard Model, therefore adding no additional neutral gauge bosons to the spectrum. The unification scale for the Standard Model couplings calculated from $SU(5)$ models, however, is in direct conflict with experimental measurements of the proton lifetime, and precision measurements show that the running couplings evolved from an SU(5) GUT do not meet at a single value, so larger gauge groups must be considered as candidates for the unification group.

1.6.1 New Neutral Gauge Bosons

All grand unification groups with groups larger than $SU(5)$ imply the existence of at least one additional neutral gauge boson. Assuming the same mass width-ratio as the Standard Model Z^0

$$\frac{\Gamma_{Z'}}{M_{Z'}} = \frac{\Gamma_{Z^0}}{M_{Z^0}} \tag{1.37}$$

the half width of the Standard Z' is

$$\frac{\Gamma}{2} = \frac{2.5\text{GeV}}{2}\frac{M_{Z'}}{M_{Z^0}}\,. \tag{1.38}$$

Since many extensions of Standard Model physics include a Z' in the particle spec-

trum, it is useful to do a model independent search. By limiting theoretical assumptions, the results from a single data analysis can be compared with predictions from a number of models to extract a limit, although the limits will, in general, be weaker than in a more specific search.

1.6.2 History of Z' Searches

CDF has searched for both ee and $\mu\mu$ decays of new heavy neutral particles by fitting the ee and $\mu\mu$ mass spectra to the expected backgrounds. The expected background in the $Z' \to \mu\mu$ channel comes from Z^0 and Drell-Yan production. The $\mu\mu$ spectrum is fit to the predicted background distributions normalized to the height of the Z^0 peak, and is found to be consistent with Standard Model processes. Misidentified dijet events contribute an additional background in the $Z' \to ee$ channel. Rather than subtract these events, they are fit to a parametric form and included the background. Combining these two analyses using a binned maximum likelihood method, a lower mass limit of 690 GeV is found for a Z' with Standard Model couplings [23].

The D0 collaboration has searched for $Z' \to ee$ by counting the number of observed events with a mass window of $M_{Z'} \pm 4$, $_{Z'}$ for each Z' value tested, and comparing to the expected number of events from Z^0 and Drell Yan in that window. This yields a mass limit of 660 GeV assuming Standard Model couplings [27].

1.7 Philosophy of this Search

Here, we reconstruct the $b\bar{b}$ spectrum and look for deviations from a smoothly falling background that could be produced by new physics. We first select a sample of common dijet events, then identify jets which have a displaced vertex consistent

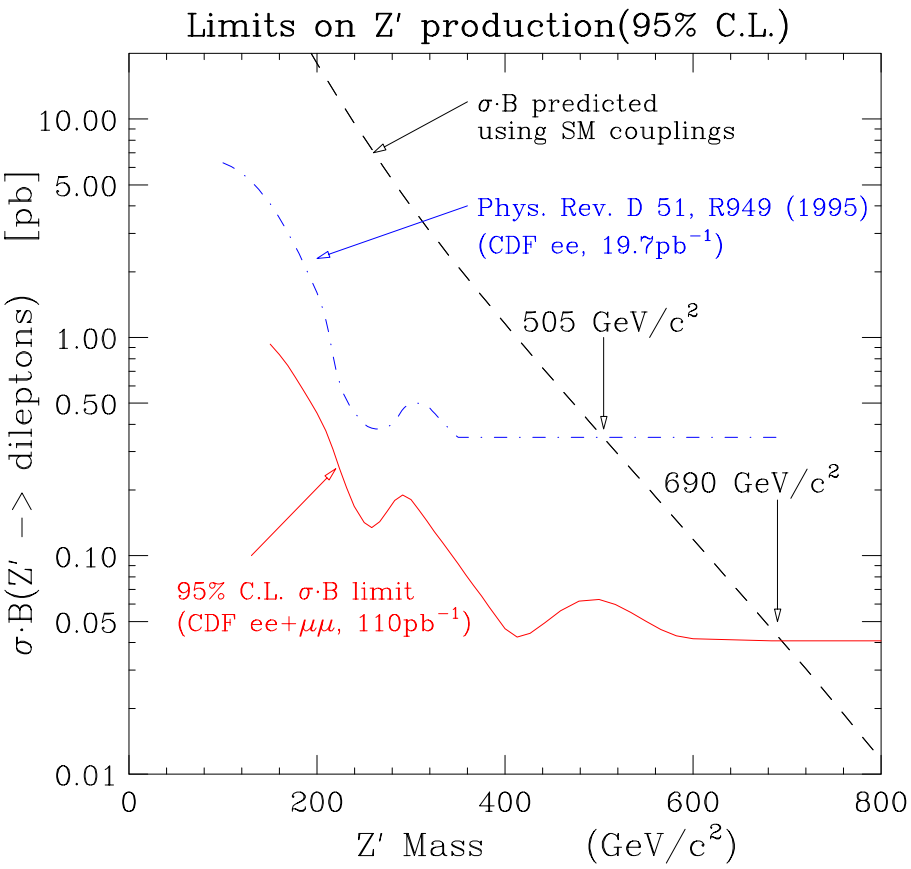

Figure 1.10

95% confidence level limit on Z' cross section in the dilepton decay channel assuming Standard Model couplings.

with a b-hadron decay. We then parameterize the shape of the $b\bar{b}$ spectrum and the shape of a simulated new particle resonance, and perform a best fit to the resonance plus a background. Using this fit we can make a quantitative statement about the inclusion or exclusion of new physics.

2. THE TEVATRON AND COLLIDER DETECTOR

With the capability of producing proton-antiproton collisions with a center-of-mass energy of 1.8 TeV, the Tevatron is, and will continue to be, the world's highest energy accelerator until the Large Hadron Collider comes online early in the next century. Until then, our best hope of producing heavy exotic particles lies with the Tevatron. With the aid of the Collider Detector, the CDF collaboration is making every effort to exploit this potential.

2.1 The Fermilab Tevatron and Accelerator Complex

In order to search for particles with a large mass and small production cross section, it is necessary to employ a machine that not only delivers collisions at high energy, but also delivers these collisions at a high rate or luminosity, since the number of events produced per second in some final state is given by $N = \sigma\mathcal{L}$, where σ is the cross section of the final state and $\mathcal{L}$ is the luminosity. The Tevatron is a superconducting proton synchrotron which accelerates a clockwise revolving beam of protons and a counterclockwise revolving beam of antiprotons to an energy of 900 GeV before colliding them head on for a total center-of-mass energy of $\sqrt{s} =$ 1.8 TeV. During collider Run IB, the Tevatron was operated with the colliding beams grouped into six bunches each of protons and antiprotons which traverse the Tevatron's 6 km circumference at a rate of 50 kHz. Electrostatic separators keep the proton and antiproton beams in different helical orbits to minimize the spreading of the beams from interaction. Quadrupole magnets focus the beams to collide

N_p	$N_{\overline{p}}$	$\mathcal{F}$	β^*	σ_l
2.32×10^{11}	5.50×10^{10}	0.59	0.35 m	0.6 m

Table 2.1

Typical values of parameters determining the luminosity of the Tevatron during Run IB.

at the interaction points. These "low beta quadrupoles" minimize the beam's beta function, β, which is used to characterize the beam's width and how the width of the beam changes as it moves around the accelerator. The luminosity of the Tevatron is thus given by:

$$\mathcal{L} = \frac{N_p N_{\overline{p}} B f}{2\pi(\sigma_p^2 + \sigma_{\overline{p}}^2)} \mathcal{F}(\sigma_l/\beta^*) \tag{2.1}$$

where B is the number of bunches, N_p and $N_{\overline{p}}$ are the number of protons and antiprotons per bunch, f is the revolution frequency, σ_p and $\sigma_{\overline{p}}$ are the RMS proton and antiproton beam size at the interaction point, and $\mathcal{F}$ is a form factor which is a function of the bunch length, σ_l, and the value of the beta function at the interaction point, β^*. Typical values of these parameters are given in Table 2.1. During Run IB, luminosities as high as $2.50 \times 10^{31}\text{cm}^{-2}\text{s}^{-1}$ were achieved with average luminosities around $1.58 \times 10^{31}\text{cm}^{-2}\text{s}^{-1}$ [28], producing an average 2.5 interactions per beam crossing with beam crossings occurring every 3.5 μs. Beams are kept circulating in the Tevatron for 10 - 12 hours. During this time, the luminosity will drop by an order of magnitude due to losses from collisions and transverse spreading of the beam. When the luminosity becomes unacceptably low, the remaining beam is dumped, and the process of preparing a new "store" of protons and antiprotons for

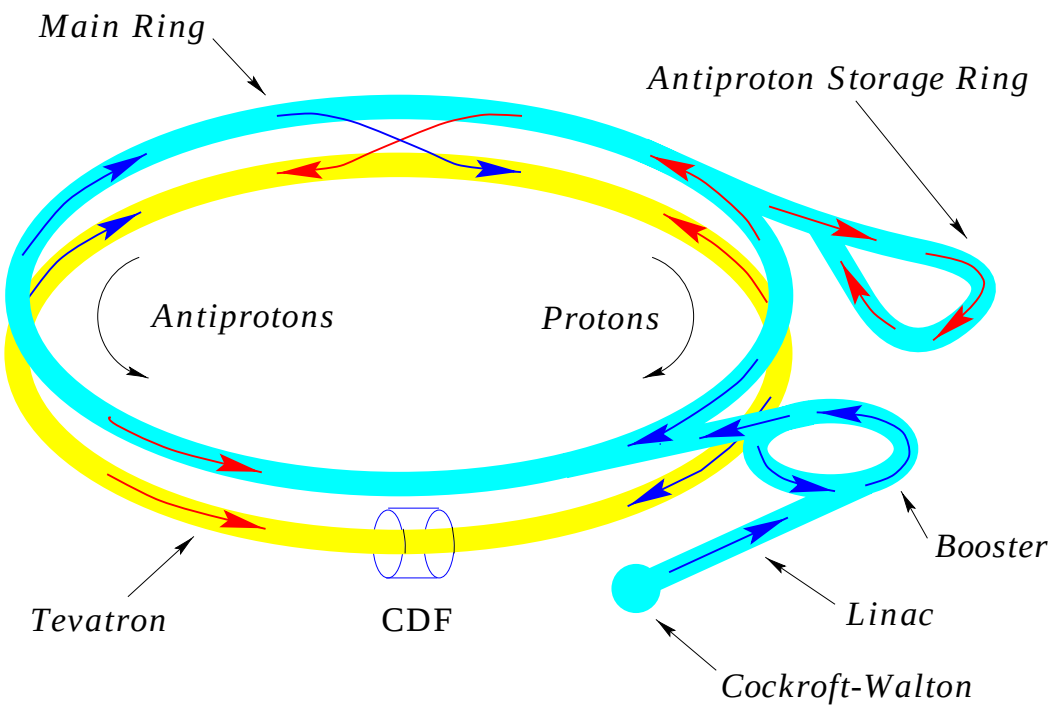

Figure 2.1

Schematic of the Fermilab accelerator complex. The radius of the Main Ring and the Tevatron is 1 km.

injection into the Tevatron commences.

The Tevatron provides the final stage of acceleration in a chain, shown in Figure 2.1, that begins with a commercial electrostatic Cockroft-Walton generator [29]. There the protons start their journey as a beam of negatively charged hydrogen ions which is accelerated across a series of voltage gaps to a modest energy of 750 keV. These ions are then fed via a transport line into a series of Linacs. A single gap RF cavity in the transport line divides the beam into bunches to optimize the capture efficiency of the Linac, since the Linac and all subsequently encountered accelerators, including the Tevatron, are designed as resonating RF cavities.

The acceleration in these cavities is accomplished by using a grounded drift tube to shield the particle beam in the regions of the cavity where the electric field is negative, the particles are accelerated across gaps in the drift tube where the field is positive. The advantage of this design is that it screens out noise by resonating at a specific design frequency, any frequency other than the design frequency will not resonate in the cavity. The Linacs boost the energy of the H^- ions to 400 MeV before feeding them into the *Booster*, an 8 GeV synchrotron with a 75.5 m radius. As the ion beam enters the Booster, it passes through a thin carbon foil which strips off the electrons. A magnet is then used to merge the remaining protons with the passing beam. Once at 8 GeV, the protons bunches are extracted and transferred to the Tevatron's predecessor, the Main Ring, which occupies the same tunnel as the Tevatron and is similar to the Tevatron in every way except that it's conventional magnets are much weaker than the Tevatron's superconducting magnets. This confines it's operation to lower energies. The Main Ring now has a dual purpose: it is used to accelerate protons and antiprotons to 150 GeV and then coalesce them into a single bunch for injection into the Tevatron, and it provides a source of 120 GeV protons used in the production of antiprotons.

The process of producing antiprotons and preparing them for later use is much more difficult and time consuming than the production and preparation of protons. The limited availability of antiprotons is one of the factors restricting the luminosity of the Tevatron. Antiprotons are created when a 120 GeV beam of protons extracted from the Main Ring strikes a thin, disc-shaped nickel target as shown in Figure 2.2. The energy of the antiprotons produced is determined by the energy of the incoming proton beam and is expected to be 8 GeV for a proton beam energy of 120 GeV [30]. The antiprotons and other secondary particles produced are focussed by a conducting lens, which is constructed of lithium, the lowest density conductor,

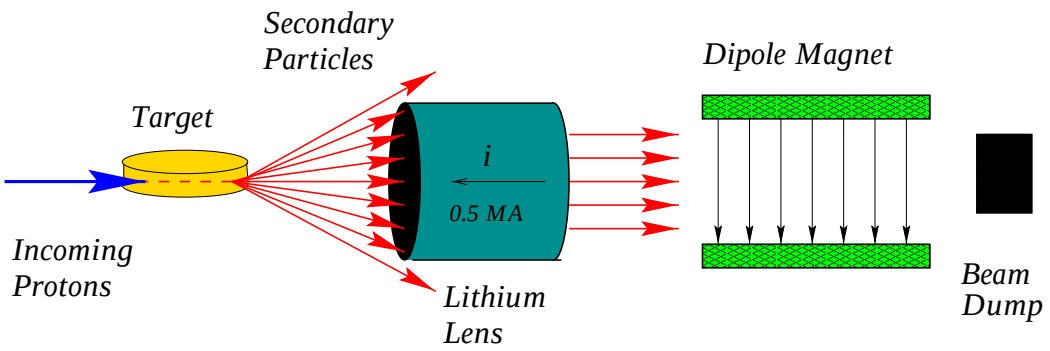

Figure 2.2

Schematic of the target station for producing antiprotons. Secondary particles produced when incoming protons strike the target are focussed by a lithium lens. Particles of the desired charge and energy are deflected away from the beam dump by a pulsed dipole magnet.

to minimize multiple scattering and antiproton absorption. An analyzing dipole magnet located downstream from the lens is then used to deflect 8 GeV negatively charged particles away from a beam dump and into the *Debuncher*. The role of the Debuncher is to reduce the momentum spread of newly produced antiprotons while maintaining their energy at a constant 8 GeV in order to maximize the capture efficiency when they are finally transferred to the Main Ring for injection. When the momentum spread of the antiprotons has been sufficiently reduced, the antiprotons are transferred to the *Accumulator* where they are stored and their momentum spread further reduced until they are needed for injection into the Tevatron. While a store of protons and antiprotons are being circulated into the Tevatron, the production of antiprotons continues in order to accumulate enough antiprotons for the next "run" of the Tevatron.

2.2 The Collider Detector

The Collider Detector was originally designed to extract information from Tevatron collisions for a broad range of particle physics analyses with particular emphasis on particle tracking, magnetic momentum analysis, and fine-grained calorimetry [31]. It was later upgraded for Run I (1992-1996) to include additional muon detectors as well as a silicon vertex detector [32]. The detector is best described by a cylindrical coordinate system with the z axis along beamline where the positive direction is defined by the direction of travel of the proton beam, and the origin is fixed at the nominal interaction point. The detector geometry was chosen for maximum solid angle coverage of the interaction region with cylindrical and forward-backward symmetry about the interaction point, as shown in Figure 2.3. The polar angle, θ, is usually given in terms of *pseudorapidity*, η, which is defined to be:

$$\eta \equiv -\ln\left(\tan\frac{\theta}{2}\right). \tag{2.2}$$

For $p \gg m$, pseudorapidity is approximately equal to rapidity, y,

$$y = \frac{1}{2}\ln\left(\frac{E+p_z}{E-p_z}\right) = \tanh^{-1}\left(\frac{p_z}{E}\right) \tag{2.3}$$

making pseudorapidity a convenient variable to use in describing particle collisions, since a Lorentz transformation in the z-direction to a frame with velocity β, shifts the rapidities of all particles by a constant amount, $y \to y + \tanh^{-1}\beta$, when viewed in the lab frame. The detector components are layered around the interaction point such that a particle produced in a collision will encounter, moving radially outward from the beam line:

- The silicon vertex detector: 4 layers of silicon microstrip detectors with inner radii between 3 and 8 cm of the beamline, used in identification of secondary vertices associated with the decay of long-lived particles.

Figure 2.3

Top: Isometric view of the CDF detector illustrating it's cylindrical and backward-forward symmetry. Bottom: Cross section of one quarter of the Run I CDF detector, with emphasis on the central detector and the projective geometry of the calorimeter towers. For scale, the radial distance from the beamline to the inner surface of the Central Electromagnetic Calorimeter is 1.73 m.

- The tracking system: The vertex time-projection chamber, central tracking chamber, and central drift tubes, located inside of a 1.4 Tesla superconducting solenoidal magnet that is 5 m long and 3 m in diameter, for precise momentum spectroscopy.
- Calorimeters: Divided into central, plug, and forward regions, the calorimeters are segmented into *towers* in increments of η and ϕ, with each tower consisting of an electromagnetic shower counter in front of a hadron calorimeter. The towers thus have a projective geometry that points back to the interaction region as shown on the bottom panel of Figure 2.3.
- The muon system: The central muon detector identifies muons with sufficient energy to reach the muon chambers ($p_T >\sim 1.5$ GeV/c), and the forward muon detector measures the position and momentum of muons at large η.

Paramount to any analysis involving jets associated with a b quark decay are the silicon vertex detector, the tracking system, and the calorimeters. The design and operation of these systems is detailed further below.

2.2.1 The Silicon Vertex Detector

The SVX' silicon microstrip detector was designed to provide precise secondary vertex information in a high radiation environment [32]. The detector consists of two barrels of single-sided AC-coupled silicon strip sensors. Each sensor is a 300 μm thick multisourced FOXFET (field oxide field effect transistor) sharing a common gate and drain, with each strip's longitudinal p^+ implant acting as the source. AC-coupling is achieved by isolating the p^+-implants from the aluminum readout strips by a 200 nm layer of SiO_2, preventing leakage currents (which increase with radiation

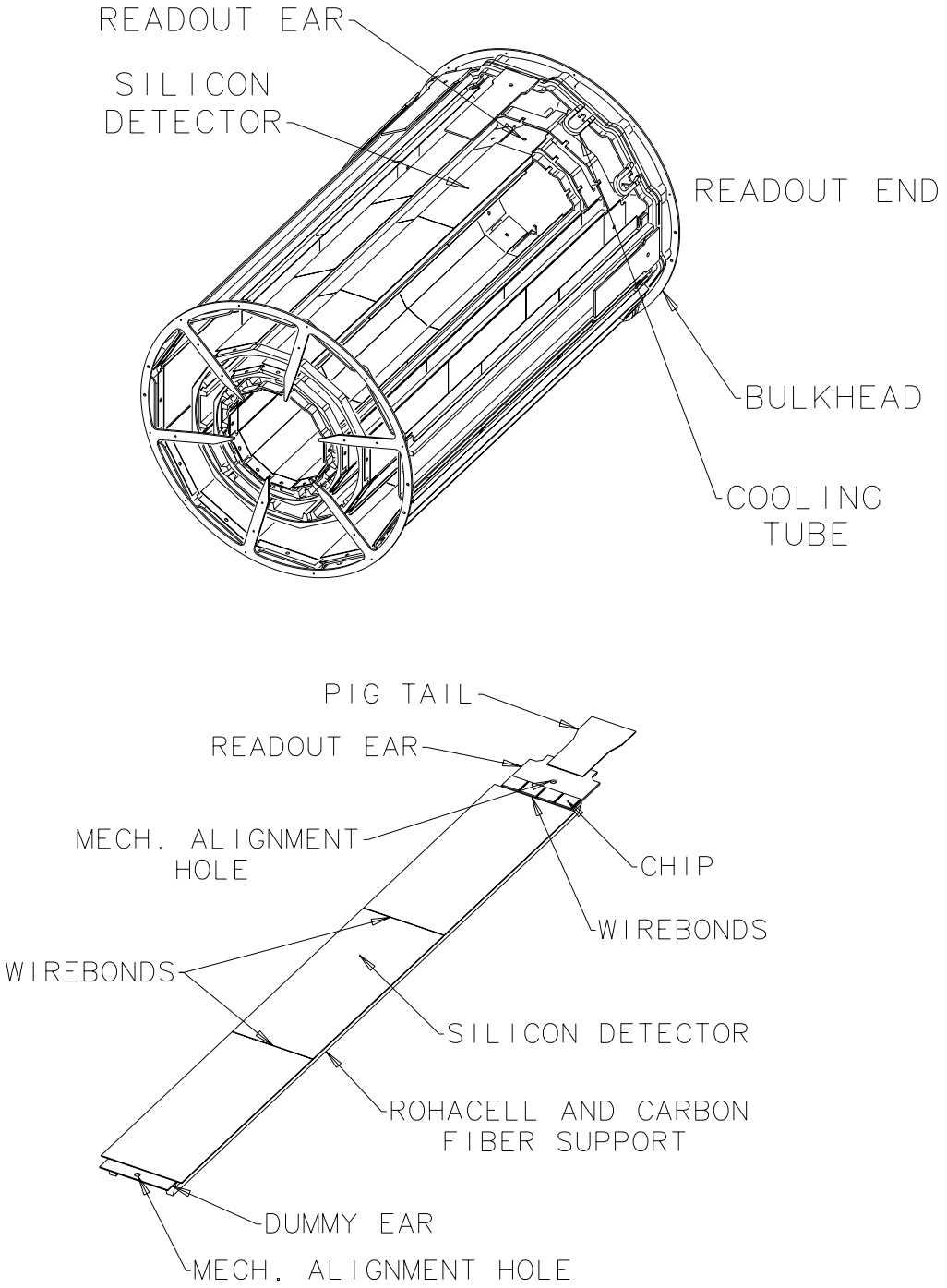

Figure 2.4

Top: Schematic of a single barrel of the SVX detector. Bottom: Schematic of an SVX ladder, a unit of three microbonded silicon strip detectors sharing a common readout.

exposure) from saturating the input amplifier. The wafers are microbonded together in groups of three (a *ladder*), sharing a common readout as shown in on the bottom of Figure 2.4. Four ladders arranged at 2.861 cm, 4.256 cm, 5.687 cm, and 7.866 cm from the beamline to form a *wedge* that subtends an azimuthal angle of 30^o. Each barrel, shown in Figure 2.4, is 25.5 cm in length, and consists of 12 such wedges. The inner three layers have a strip pitch of 60 μm, while the outer layer has a strip pitch of 50 μm. The two barrels, aligned back-to-back along the beam direction on either side of the nominal interaction point, have a total active length of 51 cm. Since the interaction point has an R.M.S. spread of 30 cm, the track acceptance is only about 60 %. The resolution as a function of p_T is given by

$$\sigma = \sqrt{19^2 + \left(\frac{41}{p_T}\right)^2} \; . \tag{2.4}$$

The typical asymptotic impact parameter resolution achieved is ~ 16 μm.

The detector is read out with the radiation hard SVXH chip. To minimize the readout time, the chip is operated in *sparse* mode, reading out only those channels registering a signal above a preset threshold (typically 5% of the total 46,080 channels). The signal to noise seen by the chip for the effective strip length of 25.5 cm is 15:1.

2.2.2 The Vertex Time Projection Chamber

Surrounding the silicon vertex detector is the vertex time projection chamber, or VTX, which is primarily an $r-z$ device used to locate the interaction vertices [33]. The VTX is an Argon/Ethane filled gas chamber that is divided along its length into 28 modules. To minimize drift times, each module is divided into two drift regions, as shown on the right side of Figure 2.5. Each module is further subdivided into eight wedges, or octants (see Figure 2.5, right). In each octant, sense wires

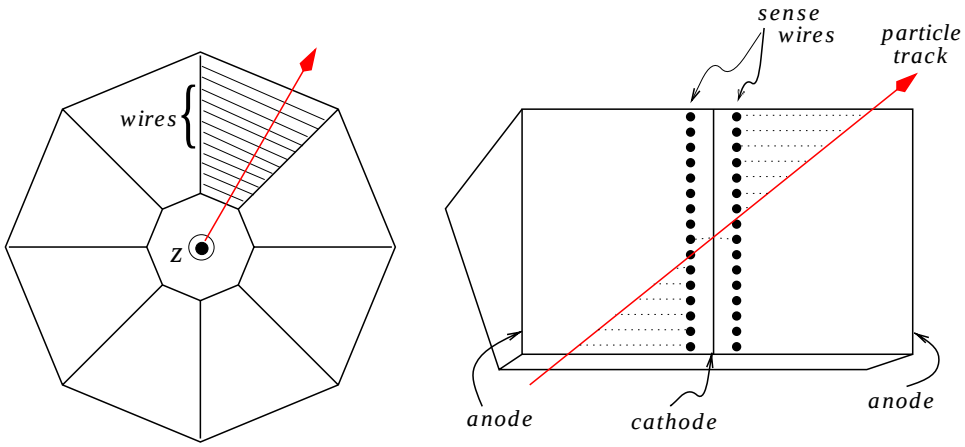

Figure 2.5

Schematic of the vertex time projection chamber. Left: Cross section of one module in the plane perpendicular to the beam pipe showing the orientation of the sense wires. Right: Side view of one octant of one module. Ions drift toward the cathode along the path shown by the dotted lines, and are collected by the sense wires.

are strung tangent the the azimuthal direction in the plane perpendicular to the beamline. Each module contains two such sets of wires which are located on either side of a central cathode. When a particle traverses a module, the ions produced in the gas drift parallel to the beam toward the cathode and are collected by the sense wires. In regions of the module where the track passes further from the sense wire plane, the pulse arrives at the sense wires later, and this timing information can be used to reconstruct an $r - z$ profile of the track. In order to endow the VTX with some limited $r - \phi$ tracking information, each module is rotated 15^o with respect to the neighboring modules. Using the VTX, the z-vertex of tracks can be resolved to 2 mm.

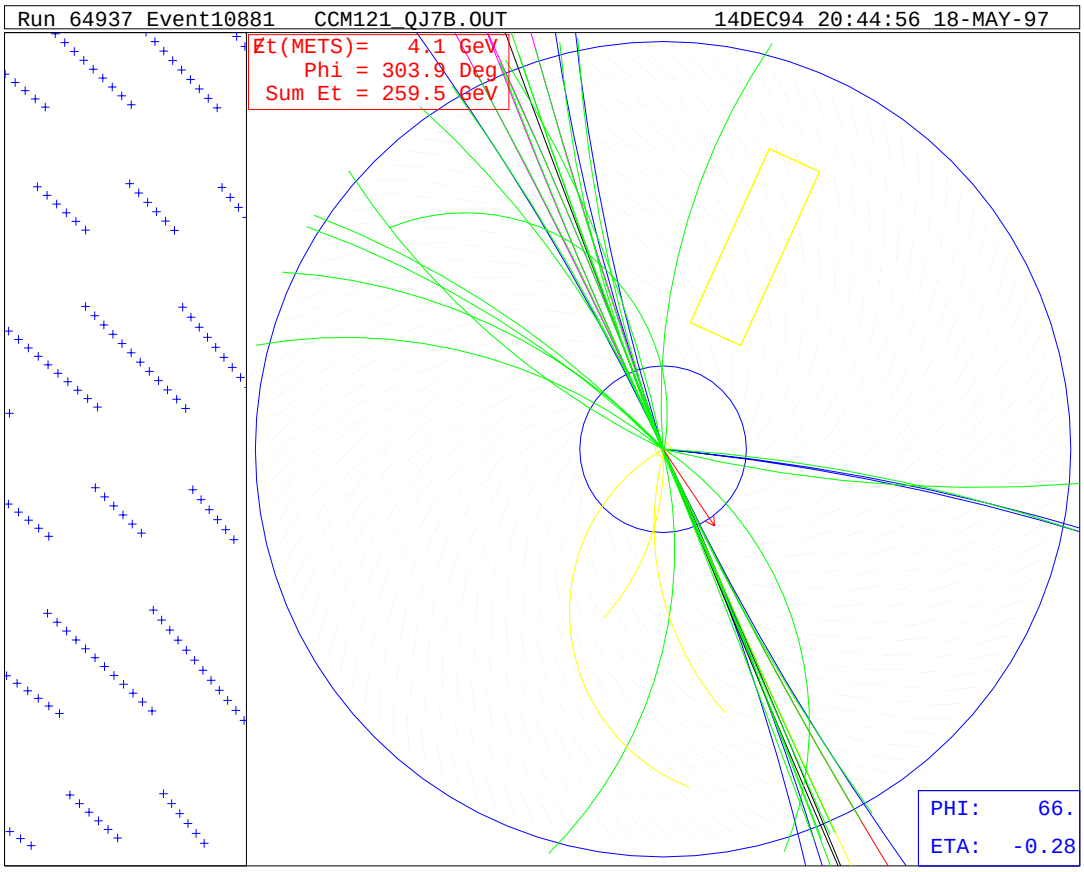

Figure 2.6

The end view of an event in the Central Tracking Chamber. Left: A magnification of the boxed area shows the configuration of the sense wires. Each "+" indicates the location of a sense wire, which is strung perpendicular to the plane of the paper. The groups of 6 wires are stereo "superlayers" while the groups of 12 wires are parallel to the beamline.

2.2.3 The Central Tracking Chamber

The Central Tracking Chamber (CTC) is a large drift chamber that was originally designed to complement the calorimetry by providing precise momentum spectroscopy for isolated high p_T particles [34]. With the installation of the SVX, it's role has expanded to additionally provide a seed for SVX tracks. Located just in-

side of CDF's 15 kG superconducting solenoidal magnet, the CTC is a right cylinder with an outer radius of 2760 mm and an inner radius of 554 mm which surrounds the SVX and VTX. It's 3201 mm length is necessary to provide adequate coverage of CDF's interaction region. Strung along it's length are 9 "superlayers" of sense wires as shown in Figure 2.6. The wires in 5 of the superlayers are strung parallel to the beamline to provide $r-\phi$ information and are interleaved with the remaining 4 superlayers which alternate between $\pm 3^o$ stereo to supply an $r-z$ coordinate. Each superlayer is divided into coplanar groups of wires called "cells" that are tilted $\approx 45^o$ from the radial plane. Each axial superlayer cell consists of 12 sense wires while 6 wires comprise each stereo cell. The tilt angle of the cells was chosen to minimize the dead space because for large tilt angles, the plane of each cell subtends a large enough azimuthal angle to overlap the next cell. Therefore the track of a high p_T particle which bends very little in the magnetic field will intersect at least one sense wire in each superlayer. This choice of angles also has the advantage of compensating for the large Lorentz angle, β of electrons with respect to the electric field which is given by [34]:

$$\tan \beta = \frac{vB}{kE} \tag{2.5}$$

where v is the drift velocity without the magnetic field and k is a parameter. The tilt of the cells was chosen to make the drift trajectories approximately azimuthal. The CTC momentum resolution in the transverse plane is $\frac{\delta p_T}{p_T^2} \approx 0.002 \mathrm{GeV}^{-1}c$. When tracking information from the SVX is added, this improves to $\frac{\delta p_T}{p_T^2} \approx 0.001 \mathrm{GeV}^{-1}c$.

2.2.4 The Calorimeters

The calorimeters, divided into the central, plug, and forward regions, are each finely segmented into projective towers that point back to the interaction region. Each tower is composed of an electromagnetic shower counter and a hadron calorime-

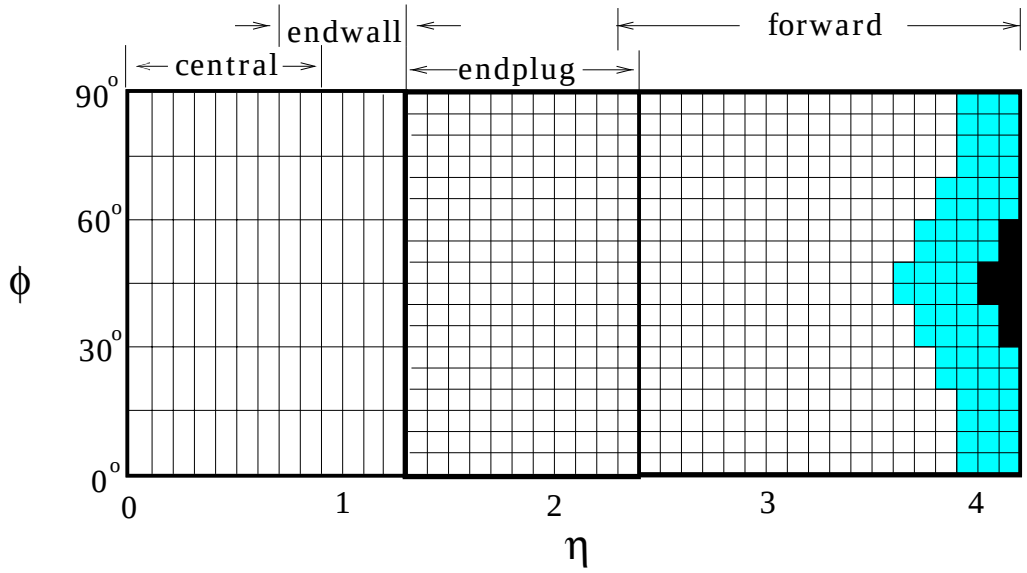

Figure 2.7

Schematic map of the hadronic calorimeter towers in one of eight $\eta - \phi$ quadrants ($\Delta\phi = 90^o, \eta > 0$). The black areas are not covered, while the shaded area has only partial coverage due to geometrical obstruction by the low beta quadrupoles. The thicker lines indicate module or chamber boundaries.

ter, so that the ratio of electromagnetic to hadronic energy can be determined precisely for each tower. Figure 2.7 maps the segmentation of the hadron calorimeters in η and ϕ space [‡], and Table 2.2 summarizes the properties of each calorimeter.

The electromagnetic calorimeters are all composed of alternating layers of lead and an active detector medium. In the central region polystyrene scintillator is used, and in order to maintain an approximately constant effective thickness in radiation lengths as polar angle varies, acrylic is substituted for lead in a portion of the layers [35]. The charge deposition on orthogonal strips and wires inserted between layers at the depth of maximum average shower development provides a

[‡]Here ϕ is the azimuthal angle where the positive z direction coincides with the direction of the proton beam.

Calorimeter		$\lvert\eta\rvert$ coverage	Tower size $\Delta\eta \times \Delta\phi$	Energy resolution GeV	Thickness
Central	EM	$\lvert\eta\rvert < 1.1$	$\sim 0.1 \times 15^o$	$13.7\%/\sqrt{E_T} \oplus 2\%$	18 X_0
	Had	$\lvert\eta\rvert < 0.9$	$\sim 0.1 \times 15^o$	$50\%/\sqrt{E_T} \oplus 3\%$	4.5 λ_0
Endwall	Had	$0.7 < \lvert\eta\rvert < 1.3$	$\sim 0.1 \times 15^o$	$75\%/\sqrt{E_T} \oplus 4\%$	4.5 λ_0
Endplug	EM	$1.1 < \lvert\eta\rvert < 2.4$	0.09×5^o	$22\%/\sqrt{E_T} \oplus 2\%$	$18 - 21$ X_0
	Had	$1.3 < \lvert\eta\rvert < 2.4$	0.09×5^o	$106\%/\sqrt{E_T} \oplus 6\%$	5.7 λ_0
Forward	EM	$2.2 < \lvert\eta\rvert < 4.2$	0.1×5^o	$26\%/\sqrt{E_T} \oplus 2\%$	25 X_0
	Had	$2.4 < \lvert\eta\rvert < 4.2$	0.1×5^o	$137\%/\sqrt{E_T} \oplus 3\%$	7.7 λ_0

Table 2.2

Summary of CDF calorimeter properties. The symbol $\oplus$ indicates that the constant term is added in quadrature. For the hadronic calorimeters, The thickness is given in interaction lengths (λ_0) for the hadronic calorimeters, and radiation lengths (X_0) for the electromagnetic calorimeters.

profile of shower position and transverse development. In the plug electromagnetic region [36], the showers are detected by 34 planes of gas proportional chambers. Each plane is digitized by quadrant to give a detailed shower profile while sampling the entire solid angle at three depths yields the energy measurement.

The hadron calorimeters consist of steel plates alternating with acrylic scintillator in the central and endwall regions and gas proportional chambers in the plug region. All of the hadronic calorimeters measure energy from a single depth sample. In the plug region, each plane is digitized individually to provide a shower profile, and finer strips were used in the layers around the shower maximum to assist in the rejection of background from π^0's and γ's [37].

2.3 Jet Triggers

Over the course of Run I, the collider detector was spectator to an estimated 12.5 trillion proton-antiproton collisions [38], with only 3.5 μs elapsing between beam crossings. Since the data acquisition rate is limited to the rate at which data can be written to tape, about 8 Hz while the beam crossing rate is 280 kHz, it must be decided which events are of particular interest while, at the same time, minimizing the dead time introduced in making the decision. CDF uses a three level trigger system to sift through these events, with more information being used, and thus more time consumed, at each level [39].

The lowest level trigger is a hardware trigger that passes events at a rate of a few kHz and introduces no dead time. Level 1 makes its decision based on:

- electromagnetic, hadronic, and total transverse energy ‡
- the transverse energy imbalance
- stiff tracks in the central tracking chamber
- muon candidates in the muon chambers

The Level 1 calorimeter trigger is based on the energy recorded in two calorimeter towers that are logically summed to reduce the number of signals, called *trigger towers*. To pass the calorimeter trigger, an individual trigger tower must have an energy above a threshold of 8 GeV in the central electromagnetic calorimeter, 11 GeV in the central hadronic calorimeter, 11 GeV in the plug electromagnetic calorimeter, or 51 GeV in either the plug hadronic calorimeter, or one of the forward calorimeters. Also relevant to the jet sample is the prescale 40 trigger, which randomly passes one of every 40 events to limit statistics for more common signatures. There are other Level 1 triggers, and although only those most important in selecting jets

‡Transverse energy is defined as $E_T \equiv E \sin\theta$. It is essentially a calorimeter based measurement of momentum transverse to the beamline.

are discussed here, it should be emphasized that any event passing Level 1 will be considered by the jet triggers at the next level.

The Level 2 trigger is more sophisticated and requires $\sim 10\mu$s to make a decision. Level 2 distinguishes jet events based on the energy measured in single clusters. [40] If an event deposits an energy of at least 3 GeV in a single electromagnetic or hadron calorimeter tower, the jet clustering algorithm starts. Level 2 then looks to see if any of the four neighboring electromagnetic or hadron towers recorded more than 1 GeV. If so, it is included in the cluster. This process continues until no more contiguous towers are found, and the energy is summed to give the total energy of the cluster. There are four jet triggers, each requiring a different minimum energy, and, for all but the Jet 100 trigger, a prescale factor. If an event passes the energy requirement for either the Jet 20 or Jet 50 triggers, Level 2 then looks to see if the event passed the prescale trigger at Level 1. Additional prescale factors are added in Level 2 for events passing the Jet 20 and Jet 70 energy requirements. The prescale factors for each jet trigger introduced at each trigger level along with the total prescale factor are summarized in Table 2.3.

Trigger	Level 1	Level 2	Total
Jet 20	must pass prescale 40 trigger	25	1000
Jet 50	must pass prescale 40 trigger	1	40
Jet 70	must pass calorimeter trigger	8	8
Jet 100	-	1	1

Table 2.3

Total prescale factor for jet events from Level 1 triggers combined with prescaling introduced in level 2.

The highest level trigger is a software trigger that executes FORTRAN algorithms on the full dataset. Level 3 runs the same jet clustering algorithm that is used in offline analysis, which will be described in more detail in Section 3.1. It looks for jets with a cone size of 0.7, and starting with a 1 GeV seed tower, sums all towers with an energy greater than 100 MeV. It cuts less stringently on energy than Level 2 and is thus fully efficient for events passing the Level 2 jet trigger.

3. DIJET EVENT SELECTION

In hard scattering processes produced in hadron collisions, a parton (a quark, antiquark, or gluon) from each of the hadrons collide to produce two partons which emerge with equal and opposite momentum in the interaction center of mass frame, while the spectator partons continue along the beam direction. Since Quantum Chromodynamics is an asymptotically free theory, the constituent partons in a hadron can be treated as free in high energy collisions, however, as the scattered parton moves further from the recoiling system, their color interaction becomes stronger. Their potential energy increases with separation until it becomes energetically favorable to create a new quark-antiquark pair from the vacuum, breaking the color lines of force in a process called *fragmentation*. New quark-antiquark pairs continue to materialize until the momentum of the initial parton dissipated, and the quarks and gluons produced are clustered or *hadronized* into color neutral states. This process creates plumes of hadronic matter which travel in approximately the same direction as the partons that initiated them. These *jets* were first observed in hadronic collisions at the Intersecting Storage Rings (ISR) [41] and the $Sp\bar{p}S$ collider at CERN in 1982 [42], and are produced copiously in collisions at the Tevatron. At CDF, they appear as localized energy depositions in the calorimeter.

When a heavy particle is formed in the collision of two partons and subsequently decays to a b-quark pair, the two b-quarks produced will initiate the fragmentation process forming two jets, each with a large momentum transverse to the beam[‡]. We

[‡]Four jets, really, but the jets formed by the spectator partons will be lost down the beam pipe.

therefore begin our search by selecting a sample of dijet events with a large invariant mass. Since this search uses a single spectrum to seek a variety of new phenomena, the selection cuts are minimal. We don't attempt to isolate events with a particular signature, but instead construct a spectrum and seek deviations from a smoothly falling background.

We use 87 pb^{-1} of data collected by the jet triggers described in Section 2.3 filtered to fit on disk as described Appendix A.

3.1 Jet clustering

A jet is a somewhat poorly defined phenomenon, since the color lines of force will correlate all of the jets in an event: both the jets resulting from the hard scattering, as well as the *underlying event*, which are jets formed from the remnants of the colliding hadrons that are lost down the beam pipe. The exact boundaries of a jet are often ambiguous, although these boundaries become more distinct as the p_T of the jet increases. CDF uses a *cone algorithm* for defining jets which sums the energy deposited in a fixed solid angle around the jet's core.

The algorithm [43] starts by ganging the colorimeter towers in the forward and endplug calorimeters together in groups of 3 in ϕ, so that the ϕ segmentation matches that of the central calorimeters (see Figure 2.7). Contiguous ganged towers are used to form *preclusters* using towers above a threshold of 1 GeV as seeds. The E_T weighted centroid is calculated for each precluster, and a cone of radius R in $\eta - \phi$ space is drawn around the centroid as shown in Figure 3.1, where

$$\text{R} = \sqrt{\Delta\eta^2 + \Delta\phi^2} \tag{3.1}$$

and ϕ is in radians. Then, using the actual tower segmentation, each tower with at least 100 MeV with a centroid lying inside the cone is included in the *cluster*.

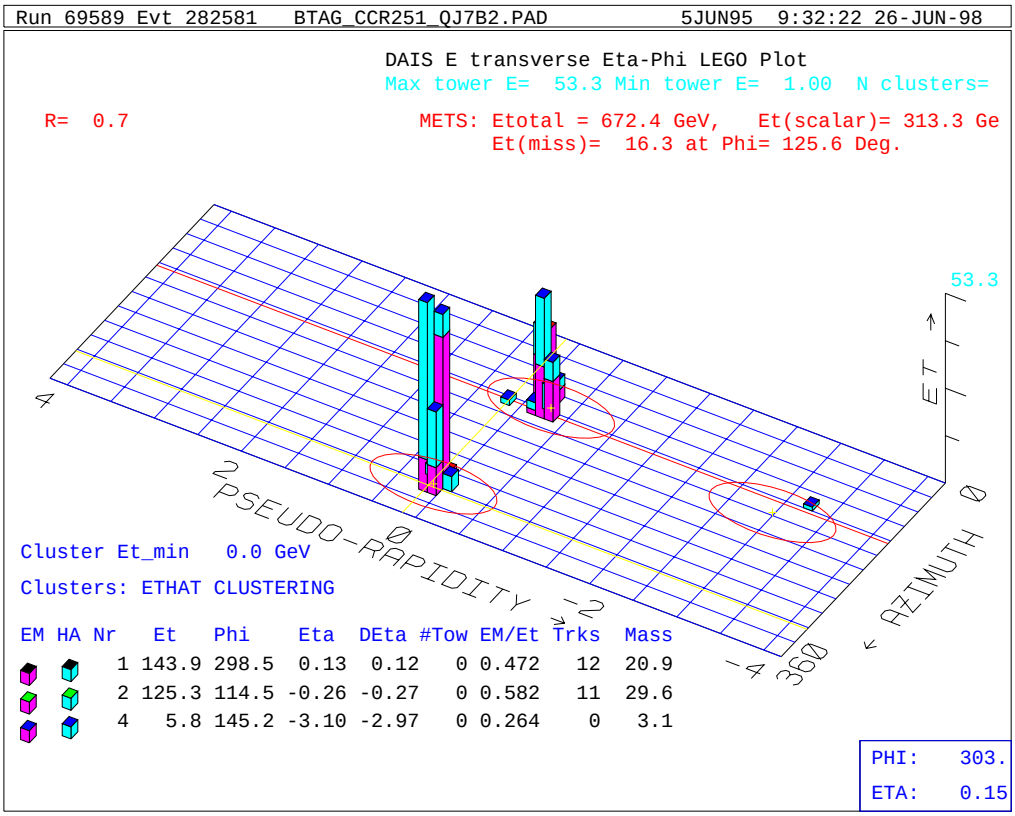

Figure 3.1

A dijet event in the CDF calorimeter as shown in a flattened $\eta - \phi$ plane. The electromagnetic energy is shown in gray and the hadronic energy is shown in black. The ovals drawn around each energy outlines the boundary of the jet cone. The (uncorrected) energy and $\eta - \phi$ location of each jet is listed in the bottom of the figure.

The E_T weighted centroid is recalculated, and a new cone is drawn. This process is repeated until the towers in the cone remains unchanged. The Level 3 trigger uses the same algorithm (see Section 2.3).

CDF analyses use standard cone sizes of R = 0.4 or 0.7. If we plot the energy deposited in the calorimeter versus the azimuthal angle for a dijet event, there

will be two maxima, at $\phi = 0$ and $\phi = \pi$ radians. The energy deposition has a broad minimum between the jets which is nonzero due contributions from the beam remnants, which leave an azimuthally symmetric energy deposition at high η [43]. The optimal cone size will maximize the percentage of the jet enveloped while minimizing contributions from recoiling spectator partons and other jets. A cone of 0.4 is often used to study processes with multijet final states, as in hadronic top decays, where the jets may overlap if a larger cone size is used. Since the physics we seek is expected to produce 2 back-to-back high E_T jets, therefore we opt for a cone size of 0.7, and correct for contributions from soft processes and energy deposited outside of the cone, as discussed below.

Figure 3.1 plots the p_T of a real dijet event as it appears in the CDF calorimeter. The energy deposition of the jets is fairly localized since the jets have very high p_T. The oval drawn around the jets define the cone used for clustering.

3.2 Jet corrections

The accurate measurement of jet energies is vital to this analysis, since the $b\bar{b}$ mass must be inferred from jet energy deposited in the calorimeters. The raw energies calculated at the trigger level generally yield a reading that differs from the true energy of the jet due to:

- deposition of jet energy outside of the jet cone,
- low p_T charged particles ($p_T \leq 400$ MeV/c) that spiral in the magnetic field surrounding the tracking chamber and therefore never reach the calorimeters,
- energy that escapes undetected through cracks in the calorimeter,
- energy carried away by muons and neutrinos that escape detection,
- nonlinearity in detector response to low energy charged hadrons ($E < 10$ GeV).

In order to reconstruct the initial partons as closely as possible, the measured jet energy in each event must be corrected for these effects.

The correction for detector effects is accomplished using a two stage routine [44, 45] which first corrects the jets relative to one another, thus removing variations in detector response, then applies an absolute energy correction to the η corrected jets. Since the jets in a two jet system should balance each other in p_T, the relative energy correction is accomplished by requiring that the p_T of the two jets in dijet events are equal. Using dijets with at least one jet in the central region of the detector, the detector response is parameterized as a function of detector η and jet p_T. This parameterization can be used to correct any jet to an equivalent central jet, which can then be corrected for nonlinear calorimeter response. The absolute energy scale correction compensates primarily for a nonlinear calorimeter response to low energy hadrons, thus, to measure this effect it is necessary accurately reproduce the energy spectrum of particles produced in fragmentation. To do this, the fragmentation properties of jets were parameterized using information from the Central Tracking Chamber (described in Section 2.2.3). This parameterization was then used to tune a Feynman-Field fragmentation routine to fragment partons to agree with the fragmentation observed in data. The simulation is then used to determine the ratio of the p_T of a particle at parton level to the sum of the p_T of the particles in the associated jet cluster.

The correction for the energy deposited outside of the jet cone is estimated using the same Monte Carlo used for the absolute energy scale correction. The amount of energy outside the cone is

$$\text{correction} = \Sigma p_T(\text{all particles}) - \Sigma p_T(\text{inside cone}) \tag{3.2}$$

and has functional dependence on jet p_T of the form $A(1 - Be^{-C \cdot p_T})$. Corrections for

Jet p_T	Cone correction
100 GeV	4.96 GeV
200 GeV	6.74 GeV
300 GeV	7.58 GeV
500 GeV	8.19 GeV

Table 3.1

Corrections for energy deposited outside of a cone of 0.7 for various jet p_T's.

energy deposited outside of a cone of 0.7 for various jet p_T's are shown in Table 3.1

In addition, the jet may also include particles contributed by the fragmentation of spectator particles which further obscures the energy of the initial partons. An estimate of this effect can be made by measuring the ΣE_T for minimum bias events (those events which result from soft hadronic processes) and calculating the energy density deposited in the calorimeters by such soft scattering processes [45]. Multiplying this quantity by the cone area gives the "underlying event" E_T, which can be subtracted from the p_T of the jet. The contribution from underlying events will vary depending on the number of interactions in the beam crossing [46], since each interaction will contribute to the calorimeter noise. The correction is therefore based on the number of vertices observed by the detector for a particular beam crossing. For a jet clustering cone of 0.7, the amount subtracted is typically 2.0 GeV for the primary vertex, and 1.5 GeV for each additional vertex.

After the corrections are applied to the jet energy (which increase the jet energies by an average 24% (19%) for 50 GeV (500 GeV) jets [47]), the two jets with the

Level 2 Trigger	Mass Cut (GeV)	Efficiency	Prescale
Jet 20	150	∼1.00	1000
Jet 50	217	0.93	40
Jet 70	292	0.95	8
Jet 100	388	0.94	1

Table 3.2

Level 2 prescale factors and trigger efficiencies at threshold for dijet mass cuts.

largest corrected E_T is defined to be the dijet. The dijet mass is calculated from the standard four vector definition:

$$\mathrm{m} = \sqrt{(E_1 + E_2)^2 - (\vec{P}_1 + \vec{P}_2)^2}. \tag{3.3}$$

3.3 Trigger Efficiencies and Mass Cuts

Since our aim is to reconstruct the $b\overline{b}$ spectrum over a broad range of masses, events from the four inclusive jet triggers described in Section 2.3 with transverse energy thresholds of 20, 50, 70, and 100 GeV (uncorrected) are used. Since any event passing the E_T threshold of a particular trigger will also pass the E_T threshold of the next lower trigger, cuts must be made to ensure that a particular mass region is not multiply covered. Since the prescaling is less severe for the higher triggers (see Table 3.2), better statistics can be gained by using data from the next highest trigger as close to threshold as possible. Therefore, for each trigger, data is used beginning with the dijet mass at which that trigger becomes reasonably efficient

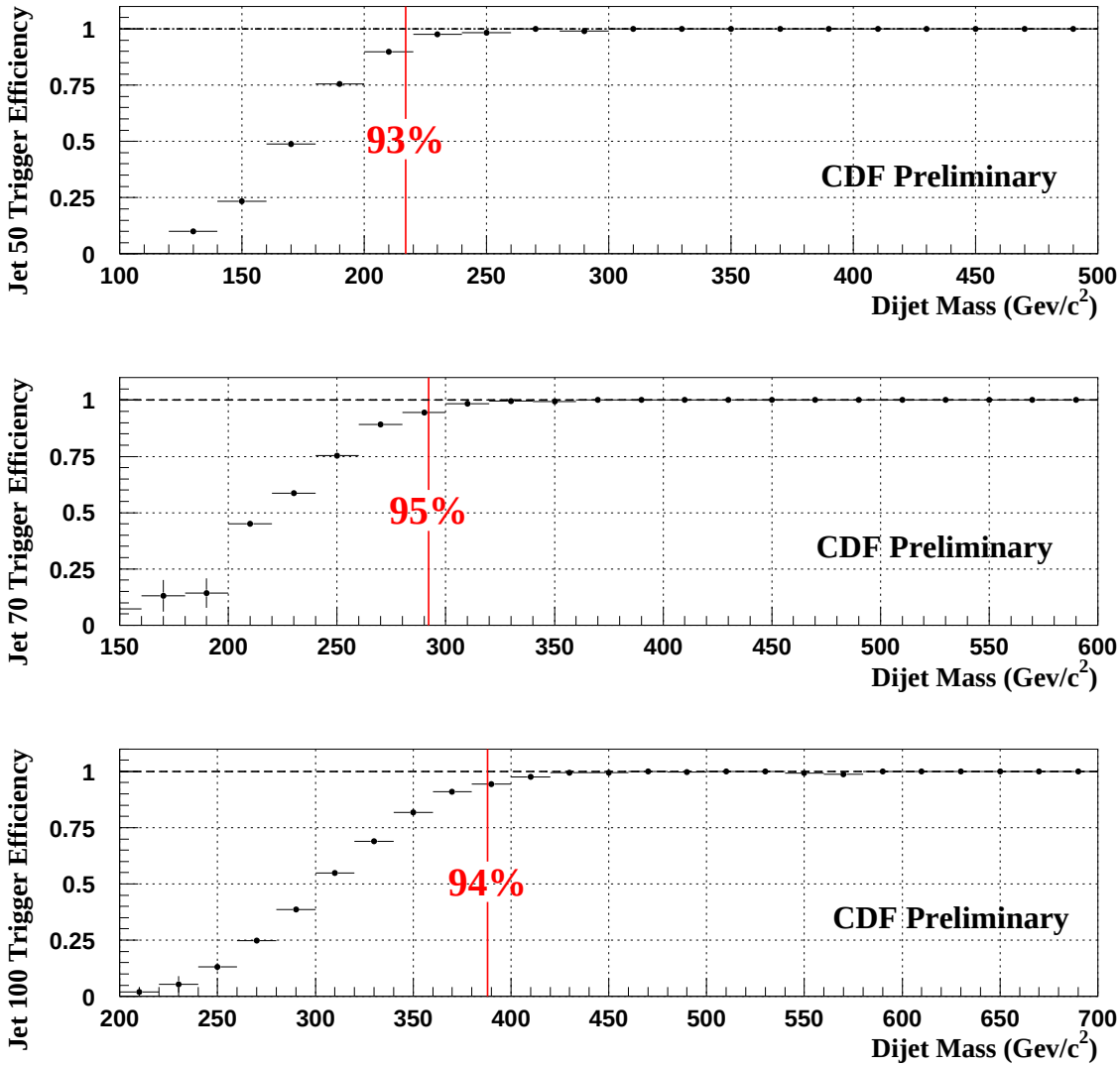

Figure 3.2

The trigger efficiency as a function of dijet mass for the JET50, JET70, and JET 100 triggers. The vertical lines represent the mass cuts chosen for each trigger.

and ending at the dijet mass where the next trigger becomes efficient. We are able to determine the trigger efficiency as a function of dijet mass by exploiting the multiple coverage of a particular mass region: by dividing the dijet mass distribution of events passing a particular trigger whose leading jet has an uncorrected E_T that is above the threshold of the next trigger by the dijet mass distribution of events in the lower trigger, we obtain a fraction of events passing the higher trigger as a function of dijet mass. Plots of trigger efficiency as a function of dijet mass for the Jet 50, 70 and 100 triggers obtained using this method are shown in Figure 3.2. The vertical line represents the dijet mass cut chosen for each trigger. Table 3.2 lists the efficiency of each trigger at the chosen cut. For the Jet 20 trigger, we chose a dijet mass cut that was safely above the dijet mass region where the Jet 20 trigger becomes fully efficient, since the lower end of the mass spectrum is not covered by multiple triggers.

3.4 Cosmic ray removal

When a cosmic ray traverses the detector, the resulting signature will characteristically contain a large amount of *missing energy*[‡], $\not\!\!E_t$, since the energy deposition of a particle originating outside of the detector will not generally be symmetric with respect to the interaction point. We therefore place a cut on the missing energy significance [48], which is defined to be

$$S_{\not\!\!E_t} \equiv \frac{\not\!\!E_t}{\sqrt{\sum E_t}}, \tag{3.4}$$

of $S_{\not\!\!E_t} < 6$ GeV$^{1/2}$. We also require that the total transverse energy, $\sum E_t$, in an

[‡]Missing energy, defined to be the negative vector sum of all transverse energy, is a measure of momentum imbalance in the detector. $\not\!\!E_t$ is often used to detect the presence of neutrinos (or more exotically the lightest supersymmetric particle) since such particles are expected to escape the detector without depositing their energy.

event be less than 2.0 TeV. These cuts are fully efficient for the new particles sought in this analysis, since their decay chain is not expected to contain large numbers of neutrinos.

3.5 Geometrical Cuts

One useful quantity in characterizing dijet production is the center-of-mass scattering angle, θ^*, which is given by

$$\cos\theta^* = \frac{p_z^*}{E_z^*} = \tanh\eta^* = \tanh\left(\frac{\eta_{jet_1} - \eta_{jet_2}}{2}\right) \tag{3.5}$$

in the limit of a massless parton. The dijet production cross-section is dominated by the t-channel exchange of gluons, causing the angular distribution to peak at small θ^*,

$$\frac{d\sigma}{d\cos\theta^*} \sim \frac{1}{\sin^4(\theta^*/2)} \tag{3.6}$$

as in Rutherford scattering [49]. The quantity measurable in the laboratory frame, $\cos\theta^*$, will therefore peak at 1 for production of common quarks and gluons [50]. Since we seek s-channel resonances, which are expected to produce back-to-back jets with large transverse energy, a cut on $\cos\theta^*$ can provide powerful background suppression, therefore, we require that $|\cos\theta^*| < 2/3$. This also ensures uniform acceptance as a function of dijet mass, since we trigger on transverse energy. We also require that the pseudorapidity, η, of both jets in the dijet satisfy $|\eta| < 2$. This restricts the jets to the fiducial region of the detector, and is complimentary to the cut on $\cos\theta^*$ in background reduction.

Since the interaction point has an RMS spread of 30 cm, we require that an event vertex lie within 60 cm of the nominal interaction point in order to exploit CDF's projective calorimeter tower geometry (see Figure 2.3). The efficiency of this cut can be determined by simply dividing the number of events in the sample

which lie in this region by the total number of events. 93% of event vertices lie in this region along the beam line.

3.6 Dijet Mass Spectrum

Finally, the dijet mass spectrum, the differential of the dijet cross-section with respect to the dijet invariant mass, is shown in Figure 3.3. The plotted differential cross sections, $d\sigma/dm$, are derived from the measured number of events, N, in each mass bin of width Δm, by $d\sigma/dm = N/(\Delta m \cdot \mathcal{L} \cdot \epsilon)$, where $\mathcal{L}$ is the luminosity (the integrated luminosity divided by the prescale factor) for that bin and ϵ is the trigger efficiency. The spectrum is binned in units of dijet mass resolution, $\sim 10\%$. To illustrate the effect of the jet corrections, the raw data is also plotted in the same figure.

There are a number of leading order $2 \to 2$ scattering subprocesses, listed in Table 3.3, that contribute to dijet production. These processes can each be characterized by a matrix element $\mathcal{M}$ which can be calculated from Feynman rules for quark and gluon propagators and vertices in QCD. Assuming massless quarks, the cross section of each subprocess can be expressed in terms of $\mathcal{M}$ and the Mandelstam variables:

$$\begin{aligned} \hat{s} &= (p_1 + p_2)^2 \\ \hat{t} &= (p_1 - p_3)^2 \\ \hat{u} &= (p_2 - p_3)^2 \end{aligned} \tag{3.7}$$

as [51]:

$$\frac{d\sigma}{d\hat{t}}(ij \to kl) = \frac{\overline{\sum}|\mathcal{M}(ij \to kl)|^2}{16\pi\hat{s}^2} \tag{3.8}$$

where $\overline{\sum}$ indicates that the matrix elements are averaged over spin and color, and i, j (k, l) denote the incoming (outgoing) partons. Table 3.3 lists the form of matrix

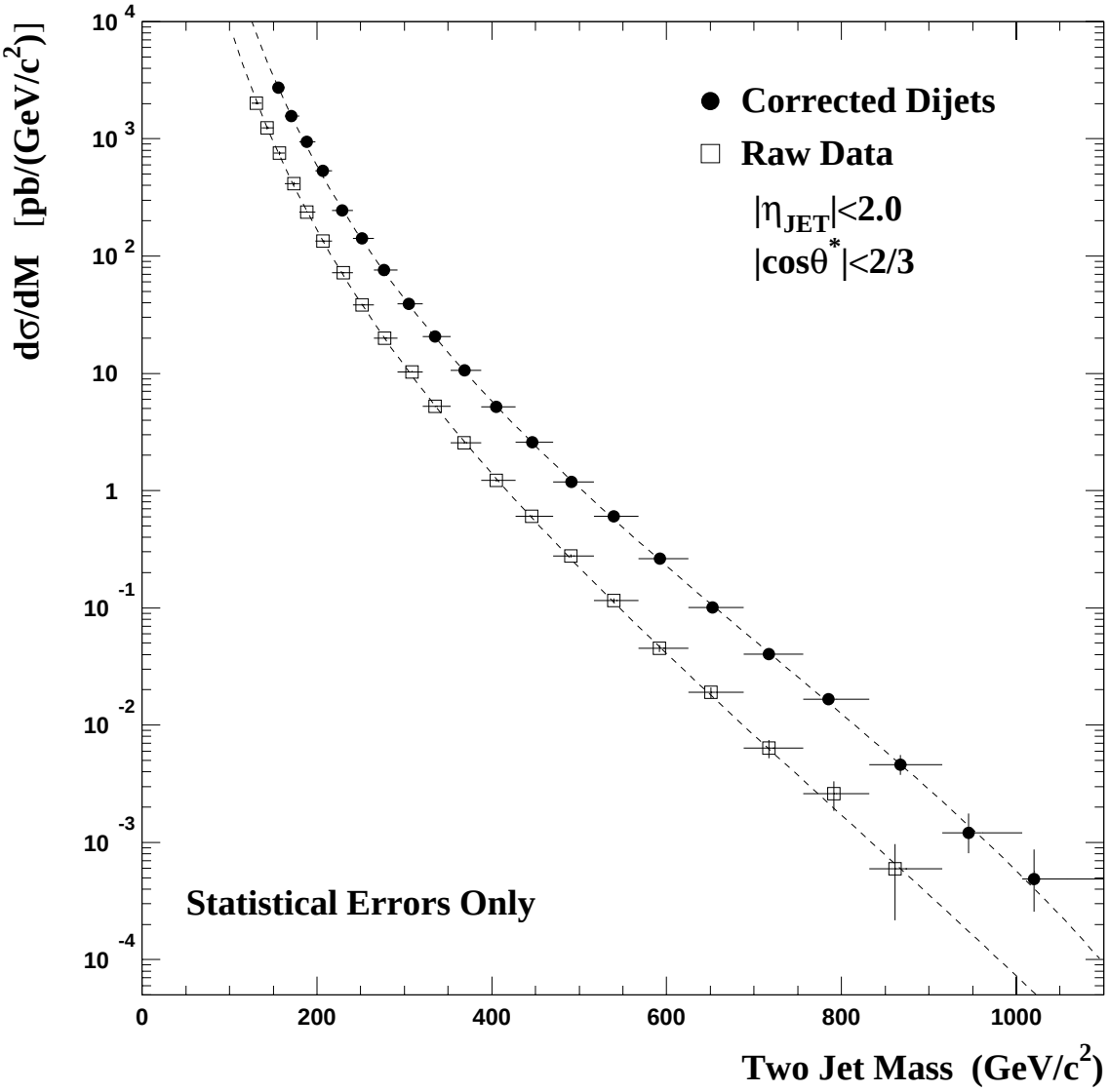

Figure 3.3

The CDF Run IB dijet mass distribution (circles) superimposed over a smooth background fit. The horizontal bars represent the bin width, with the point plotted at the mass weighted centroid of each bin, and the vertical bars show the statistical errors. The raw data (squares) is also shown to illustrate the effect of jet corrections.

Subprocess	$\overline{\sum}\lvert\mathcal{M}\rvert^2/g^4$	$\theta^* = \pi/2$
$q\bar{q}' \to q\bar{q}'$ $qq' \to qq'$	$\frac{4}{9}\,\frac{\hat{s}^2+\hat{u}^2}{\hat{t}^2}$	2.22
$qq \to qq$	$\frac{4}{9}\left(\frac{\hat{s}^2+\hat{u}^2}{\hat{t}^2} + \frac{\hat{s}^2+\hat{t}^2}{\hat{u}^2}\right) - \frac{8}{27}\,\frac{\hat{s}^2}{\hat{u}\hat{t}}$	3.3
$q\bar{q} \to q'\bar{q}'$	$\frac{4}{9}\,\frac{\hat{t}^2+\hat{u}^2}{\hat{s}^2}$	0.22
$q\bar{q} \to q\bar{q}$	$\frac{4}{9}\left(\frac{\hat{s}^2+\hat{u}^2}{\hat{t}^2} + \frac{\hat{t}^2+\hat{u}^2}{\hat{s}^2}\right) - \frac{8}{27}\,\frac{\hat{u}^2}{\hat{s}\hat{t}}$	2.59
$q\bar{q} \to gg$	$\frac{32}{27}\,\frac{\hat{t}^2+\hat{u}^2}{\hat{t}\hat{u}} - \frac{8}{3}\,\frac{\hat{t}^2+\hat{u}^2}{\hat{s}^2}$	1.04
$gg \to q\bar{q}$	$\frac{1}{6}\,\frac{\hat{t}^2+\hat{u}^2}{\hat{t}\hat{u}} - \frac{3}{8}\,\frac{\hat{t}^2+\hat{u}^2}{\hat{s}^2}$	0.15
$gq \to gq$	$-\frac{4}{9}\,\frac{\hat{s}^2+\hat{u}^2}{\hat{s}\hat{u}} + \frac{\hat{u}^2+\hat{s}^2}{\hat{t}^2}$	6.11
$gg \to gg$	$\frac{9}{2}\left(3 - \frac{\hat{t}\hat{u}}{\hat{s}^2} - \frac{\hat{s}\hat{u}}{\hat{t}^2} - \frac{\hat{s}\hat{t}}{\hat{u}^2}\right)$	30.4

Table 3.3

Squared matrix elements (averaged over spin and color) for leading order $2 \to 2$ subprocesses for massless partons, where q and q' represent distinct quark flavors. The values of the matrix elements at a center-of-mass scattering angle of 90^o is shown in the last column.

elements along with their numerical value calculated at $\theta^* = 90^o$ as a comparison of their relative importance. Another quantity that influences the dijet cross section are the parton distribution functions, f_i, which characterize the probability of finding a parton within the incoming hadron carrying a fraction, x, of the hadron's momentum. There is one such function for each type of parton. In terms of these ingredients, the dijet production cross section can be written as [52]

$$\frac{d^3\sigma}{dy_3 dy_4 dp_T^2} = \frac{1}{16\pi s^2} \sum_{i,j,k,l=q,\bar{q},g} \frac{f_i(x_1,\mu^2)}{x_1} \frac{f_j(x_2,\mu^2)}{x_2} \times \overline{\sum} |\mathcal{M}(ij \to kl)|^2 \frac{1}{1+\delta_{kl}} \quad (3.9)$$

where y_3 and y_4 are the rapidities of the final state partons, and the Kronecker delta gives an additional factor of $\frac{1}{2}$ to identical final state partons, since they are summed twice.

Based on this description, a few qualitative statements can be made about the shape and content of our mass distribution. First, from the last column of Table 3.3 we see that processes with initial state gluons dominate the matrix elements. From Figure 3.4 we see that they dominate the parton distribution functions at low x as well. At low p_T, or dijet mass since the two are related by

$$M_{JJ}^2 = \hat{s} = 4p_T^2 \cosh^2 y^*, \quad (3.10)$$

we therefore expect for processes with initial state gluons to dominate the spectrum. As we move toward the high p_T end of the spectrum, however, subprocesses with quarks in the initial state will increase in relative importance, since the valence quarks dominate the parton distribution functions at high x. Second, the falling shape of the distribution reflects the parton falloff at high x. The momentum fraction required to produce dijets of a given summed p_T, $\sum |p_T|$, is $x \sim p_T/E_p$, where E_p is the proton collision energy, thus, as the $\sum |p_T|$ approaches E_p, the number of partons carrying the required momentum fraction falls rapidly.

Since our proposed method for a model-independent search involves a simple analysis of the shape of the distribution, we need a parameterization of the observed form of the dijet cross section. From Equation 3.9 we know that the differential cross section is directly proportional to the parton distribution functions, which can be parameterized by $q(x) = x^n(1-x)^p$, where x can be approximated as $x \sim m/E_p$, and E_p is the proton collision energy. It is also inversely proportional to $\hat{s}^2$, where $\hat{s}^2 \sim m^2$, where m is the dijet mass. Thus we choose a smooth parameterization of the form:

$$\frac{d\sigma}{dm} = \frac{A(1 - m/\sqrt{s} + Cm^2/s)^N}{m^p} \tag{3.11}$$

where A, C, N, and p are parameters, and we use s here to denote the square of the proton center of mass collision energy. This parameterization gives a good fit to the data, as shown in Figure 3.3.

Now that we have selected a high p_T dijet sample, we need to identify jets emanating from heavy flavor decays, since, from the discussion above, we expect $b\bar{b}$ final states to contribute only a minute portion of the dijets in our spectrum. The next chapter describes a method of *tagging* heavy flavor jets using the tracking system, and, in particular, the silicon vertex detector, to reconstruct secondary vertices from B-hadron decays.

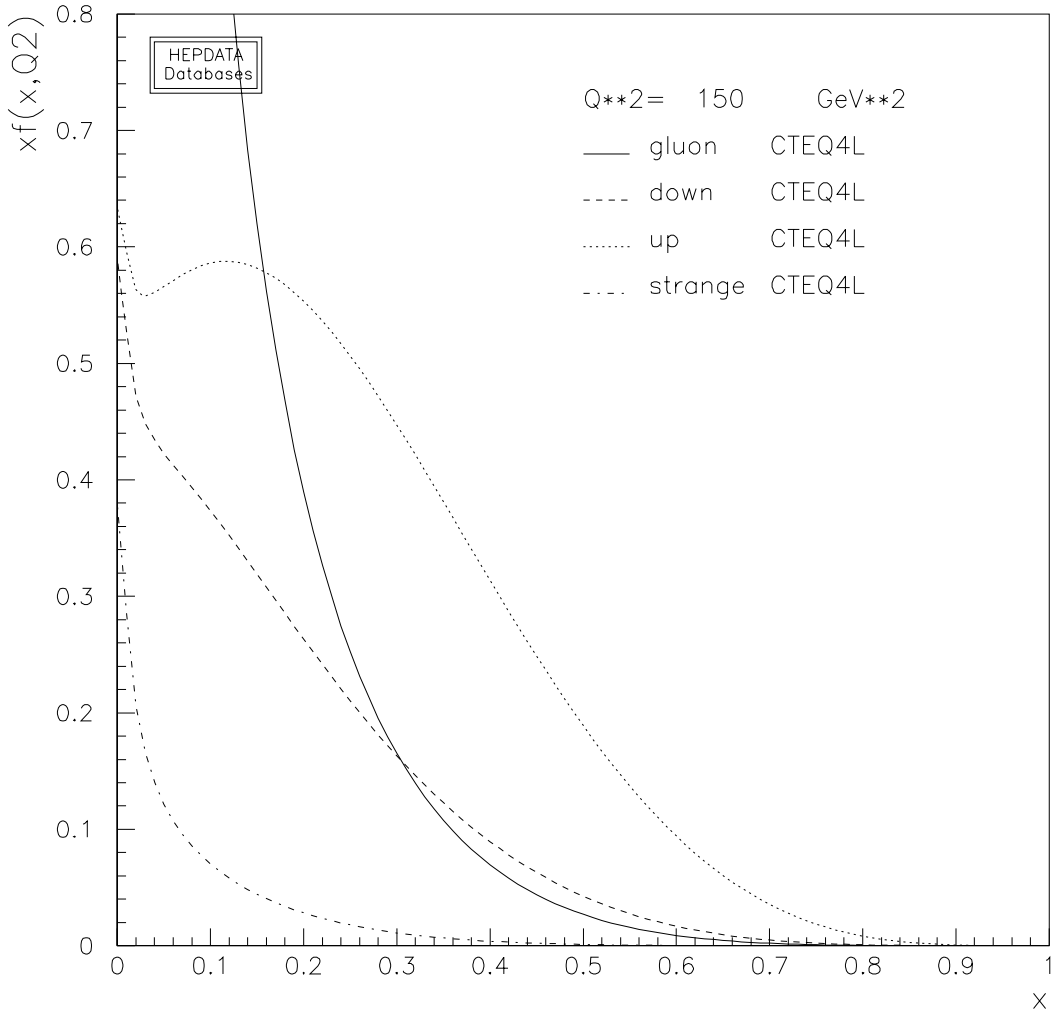

Figure 3.4

The momentum distribution of gluons and valence quarks in a proton expressed as a fraction of the proton's total momentum, x. The valence quarks carry the largest momentum at high x. Up carries the larger fraction of the valence quarks since there are twice as many valence up quarks as down in a proton.

4. $b\bar{b}$ MASS SPECTRUM

Daughters produced in a heavy particle decay will have a large momentum transverse to the beam, or p_T. Since this p_T will be large compared to the scale set by the b-quark mass, $b\bar{b}$ pairs produced in such a decay will receive large boost, thus, given the long b quark lifetime of 1.5 ps, $b\bar{b}$ pairs produced with a large transverse momentum are expected to travel a measurable distance in the plane transverse to the beam before decaying themselves, leaving in their wake a *secondary vertex* that is significantly displaced from the interaction point, or *primary vertex*. This property can be exploited in identifying jets containing a b-quark decay, allowing us to select a sample of jet events that are enriched with b jets that can be used to reconstruct the $b\bar{b}$ mass spectrum.

4.1 The search for displaced vertices using the SVX

A schematic of an event containing a high p_T b hadron decay is illustrated in Figure 4.1. The b travels a distance L_{xy} from its point of origin in the plane perpendicular to the beam axis before decaying. The tracks from the event can be precisely reconstructed using the sensitive $r-\phi$ position resolution of the silicon vertex detector described in Section 2.2.1 along with a three dimensional profile from the CTC. The final track parameter measurements are made by finding a track in the CTC which is then matched to the corresponding SVX clusters. At CDF, the primary interaction vertex has a Gaussian distribution $\sigma \sim 30$ cm along the beam axis and $\sigma \sim 23$ μm transverse to the beam axis [53]. In addition, the detector has a

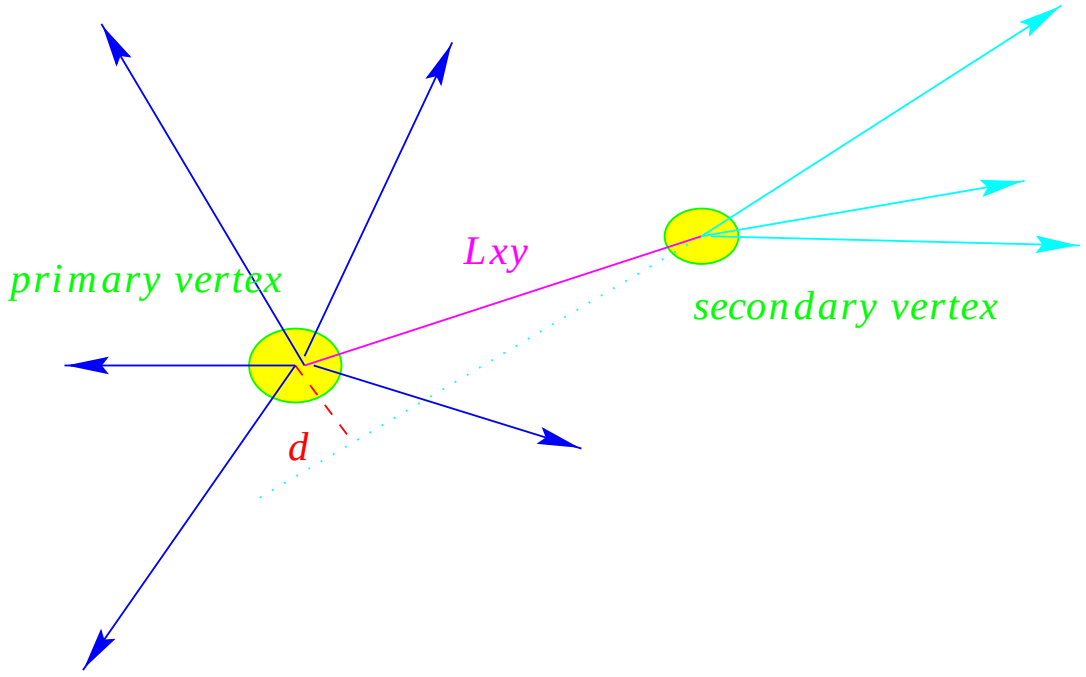

Figure 4.1

Simplified view of an event containing a secondary vertex shown in the transverse $r-\phi$ plane. The solid lines are charged particle reconstructed by the SVX. L_{xy} is the two dimensional distance from the primary to the secondary vertex. The impact parameter, d, is the distance of closest approach of a track to the primary vertex in the $r-\phi$ plane.

small slope relative to the beam, ~ 6 μm/cm in the horizontal plane and -3 μm/cm in the vertical plane, which drift over the course of data taking due to changes in the Tevatron parameters. Thus, a precise measurement of the primary interaction vertex is a prerequisite for the identification of displaced vertices. A measurement of the alignment of the beam axis relative to the detector, accurate to .4 μm/cm, was made on a run-by-run basis. A weighted fit of SVX tracks can be used along with the z event position measured in the VTX (described in Section 2.2.2) and the measured detector offset to locate the primary vertex. Tracks emanating from the

b hadron decay are measurably displaced from the point of the $p\overline{p}$ collision, thus, tracks with a large impact parameter are removed from the primary vertex fit. The impact parameter, d, is the distance of closest approach to the interaction point measured in the $r-\phi$ plane. Using significantly displaced tracks, the position of the secondary vertex can be reconstructed.

SECVTX [54, 55] is a seed vertexing algorithm originally developed for the top search that tags jets using track information from the silicon vertex detector. It attempts to optimize b-tagging efficiency without enhancing the mistag rate by loosening track quality and kinematic cuts for tags with a higher track multiplicity than the minimum two tracks needed to define a secondary vertex. The algorithm therefore consists of two passes, the first pass attempts to find three or more tracks pointing back to the same vertex using a two track seed, otherwise, a second pass is made to search for a two track vertex using only those tracks that pass tighter quality cuts.

On the first pass (Pass 1), the two track seed is chosen by ranking the candidate tracks within a jet according to their p_T, impact parameter significance, S_d [‡], and the number of unambiguous SVX hits in the track. Candidate tracks are required to have $p_T > 0.5$ GeV and $S_d > 2.5$, and at least one of the tracks in the seed must have $p_T > 2.0$ GeV. The program then constrains these tracks to a vertex and attempts to associate this vertex with other tracks. If this procedure fails to find at least one other correlated track, the process starts again, using another pair of tracks as a seed. If no secondary vertex candidate is found after all combinations of tracks have been used as seeds, the algorithm proceeds to the second pass.

On the second pass (Pass 2), the program requires candidate tracks to have $p_T > 1.0$ GeV and $S_d > 3.0$. All tracks meeting these criteria are constrained to

[‡]The impact parameter significance is defined as $S_d \equiv \frac{d}{\sigma_d}$.

form a vertex. Tracks contributing $\chi^2 > 50$ to the fit are rejected, and a new fit is performed. After all such tracks are excluded, at least two tracks must remain, and at least one of the remaining tracks must have $p_T > 2$ GeV.

After vertexing, a jet is considered tagged if:

- The secondary vertex is significantly displaced: $\frac{|L_{xy}|}{\sigma_{L_{xy}}} > 3$ and $\chi^2 < 50$.
- The vertex lies in the region inside of the inner radius of silicon $|L_{xy}| < 2.5$ cm. This reduces background from interactions with the silicon.
- The tag is not consistent with the decay $K_s^0 \to \pi\pi$. Such decays are explicitly removed by discarding two-track tags with an invariant mass of 497.6 ± 20.0 MeV when the charge of the tracks sum to 0.

4.2 Simulations

To determine our efficiency for tagging a b emanating from a heavy particle decay, we apply the SECVTX algorithm to Monte Carlo simulations of $Z' \to b\overline{b}$ using events generated by PYTHIA with the B-hadrons decayed by the CLEO Monte Carlo QQ which are then fed to a detector simulation. A description of these simulation packages can be found in Appendix B. The tagging efficiency is expected to vary as a function of jet E_T due to kinematic effects: higher E_T jets will be more collimated, making it less likely that the tracking chambers can resolve neighboring tracks, the track multiplicity of the jet will increase, and the more energetic B hadrons will receive a boost that will, on average, increase their 2-dimensional decay length, L_{xy}. Monte Carlo samples were therefore generated at masses of 200, 300, 400, 500, 600, and 700 GeV, so that the tagging efficiency could be parameterized as a function of mass. Because the detector reconstruction packages use an idealized model of detector response, however, the efficiency determined from Monte Carlo is taken to be an upper bound and must be used with a correction factor.

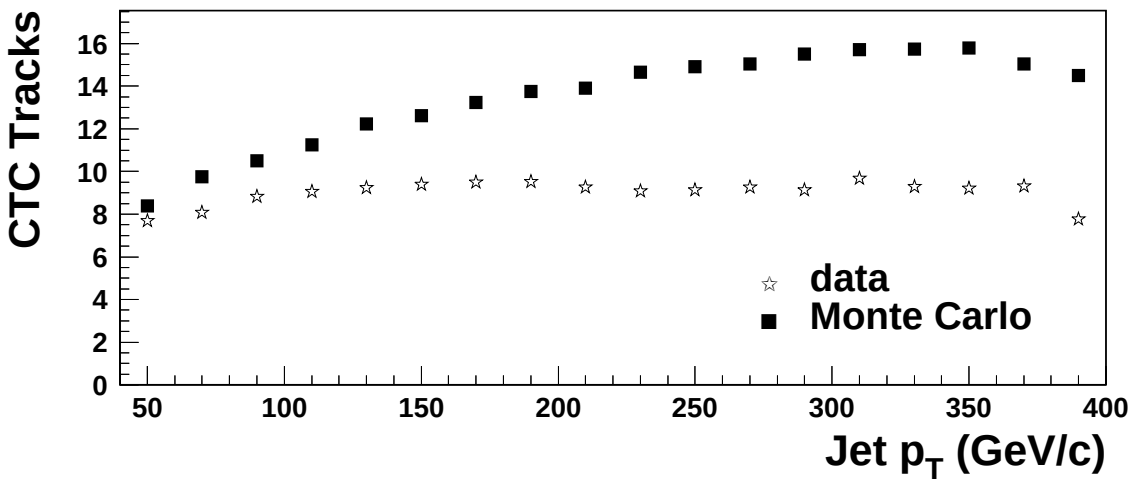

Figure 4.2

The multiplicity of CTC tracks in central jets ($-1 < \eta < 1$) in data (stars) and Monte Carlo (squares).

The b-tagging efficiency has previously been studied using an electron sample [56], which is enriched with b-jets from semileptonic B decays, $b \to \ell\nu c$. The b fraction of the electron sample has been accurately measured, thus the efficiency can be calculated by simply dividing the fraction of b-tagged jets by the measured b fraction. Comparing this efficiency to the tagging efficiency determined from Monte Carlo gives a scale factor which can then be applied to a Monte Carlo sample (top, for example) to get the efficiency for the process under study. The statistics in the lepton data samples at the energies considered here are limited, however, and we need to understand the efficiency as a function of dijet mass, thus we must rely solely on Monte Carlo for an estimate of our tagging efficiency.

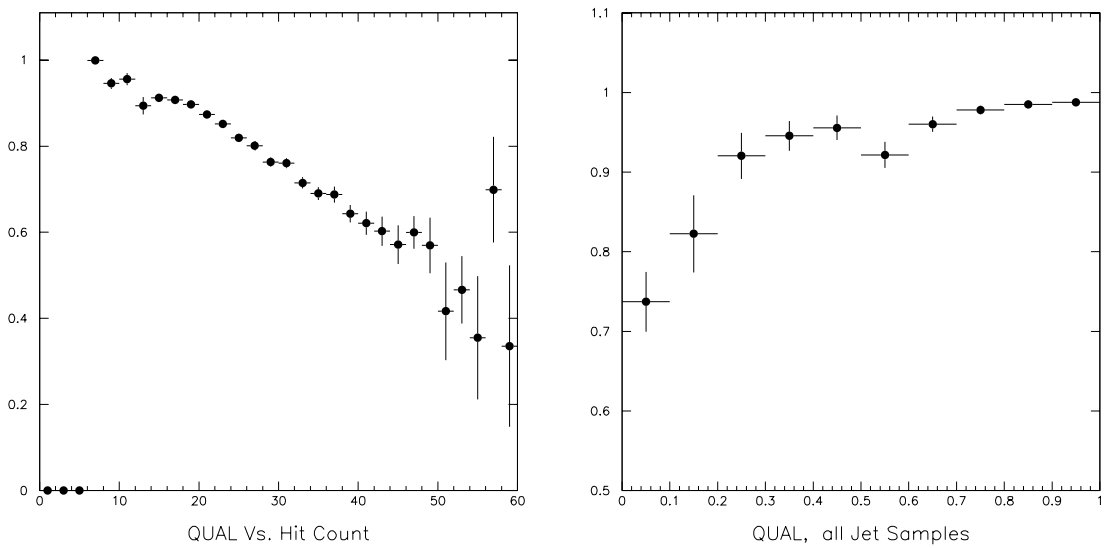

Figure 4.3

The track quality, Q, as a function of the number of obscured hits in the Central Tracking Chamber (left), and the track reconstruction efficiency as a function of Q (right).

4.3 Tracking Efficiency

A comparison of the jet track multiplicities in Monte Carlo and data indicate that the discrepancy between the tagging efficiencies in data and Monte Carlo result from an overestimate of the track reconstruction efficiency in the Central Tracking Chamber by the CDF detector simulation packages as illustrated in Figure 4.2 which compares the track multiplicity of central ($-1.0 < \eta < 1.0$) jets as a function of E_T in a cone size of 0.7 in our Monte Carlo and data samples. This has a measurable impact on the b-tagging efficiency because tracking information from both the CTC and the SVX is required for accurate track reconstruction. The separation at which the detector can resolve two tracks with 50% efficiency is 0.15 mm in the SVX, 2 mm in the inner layers of the CTC, and 3 mm in the outer

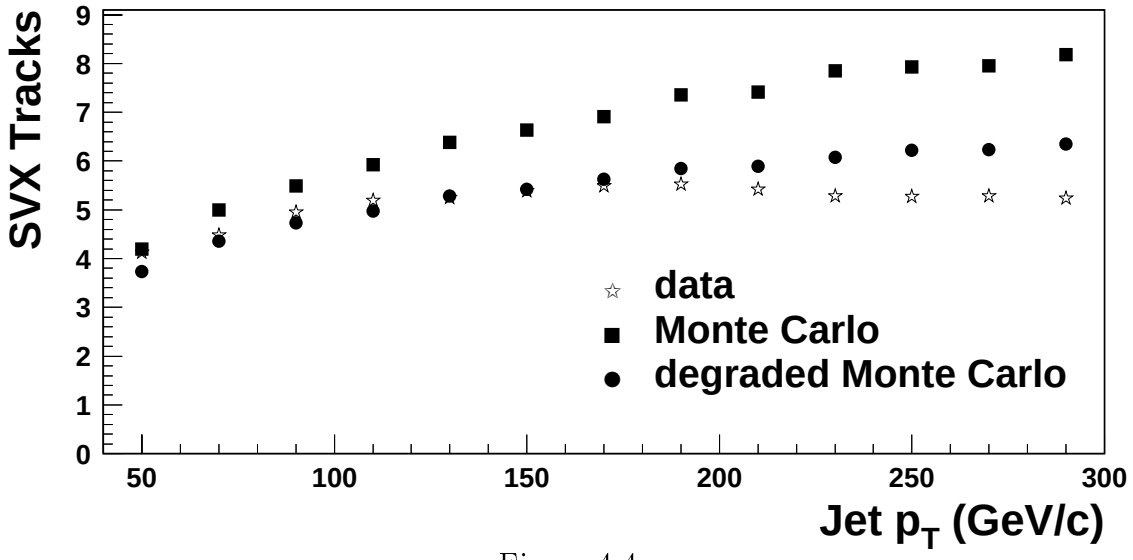

Figure 4.4

The number of SVX tracks with a CTC match per jet for central ($-1 < \eta < 1$) jets in data (stars), Monte Carlo corrected for luminosity effects only (squares), and Monte Carlo which has been corrected for tracking degradation effects.

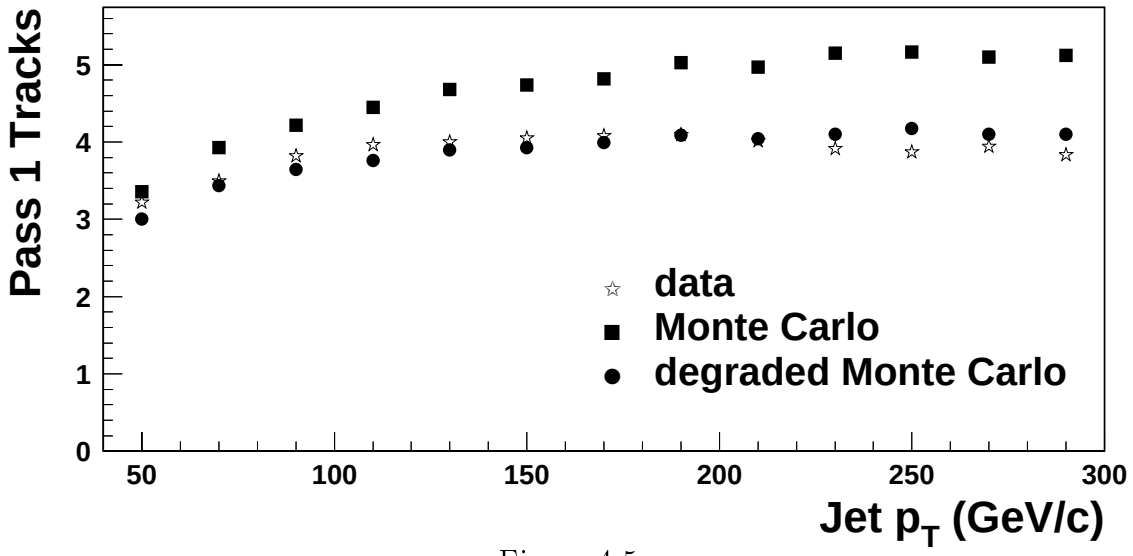

Figure 4.5

The number of SVX tracks per jet for central ($-1 < \eta < 1$) jets passing quality cuts for Pass 1 of the SECVTX tagging algorithm in data (stars), Monte Carlo corrected for luminosity effects only (squares), and Monte Carlo which has been corrected for tracking degradation effects.

layer of the CTC. The probability of reconstructing a track therefore depends on its immediate environment: well isolated, high p_T tracks are reconstructed accurately, and with very high efficiency, while tracks in a dense environment (near the axis of a jet, for example) are more likely to be merged with a neighboring track or to be reconstructed incorrectly. This effect was parameterized by generating Monte Carlo tracks, embedding them in real jet events, and measuring what fraction of the time the generated track was accurately reconstructed [57, 58]. Every Monte Carlo track is assigned a value of "Q" which is dependent on the density of tracks in the area around the track and the number of shared hits as shown in the left hand plot of Figure 4.3. A parameterization of the probability of reconstructing a track in the CTC as a function of its quality, Q, is shown in the right hand plot of Figure 4.3.

The efficiency for matching reconstructed CTC tracks to the corresponding track in the SVX is ($\sim 88\%$). In addition, the instantaneous luminosity also contributes a 5% degradation to the tracking efficiency [58]. The effect of the luminosity is measured directly from data by measuring the track multiplicity in jet data as a function of instantaneous luminosity.

The measured tracking efficiency is applied to the generated Monte Carlo events by calculating Q for each track in the event, then randomly discarding Monte Carlo tracks based on the probability that a track of similar quality would be reconstructed in the data using the parameterization of the efficiency vs. Q. This reproduces the tracking efficiency observed in data as shown in Figures 4.15 and 4.5 which plot the number of tracks SVX tracks as a function of jet p_T before and after imposing the loose track quality requirements for the first pass of SECVTX. The tracks are fed to SECVTX only after the tracking degradation is applied. The resulting b-tagging efficiency measured from Monte Carlo is found to be in good agreement with the efficiency measured from lepton data at low mass [59]. Figure 4.6 shows

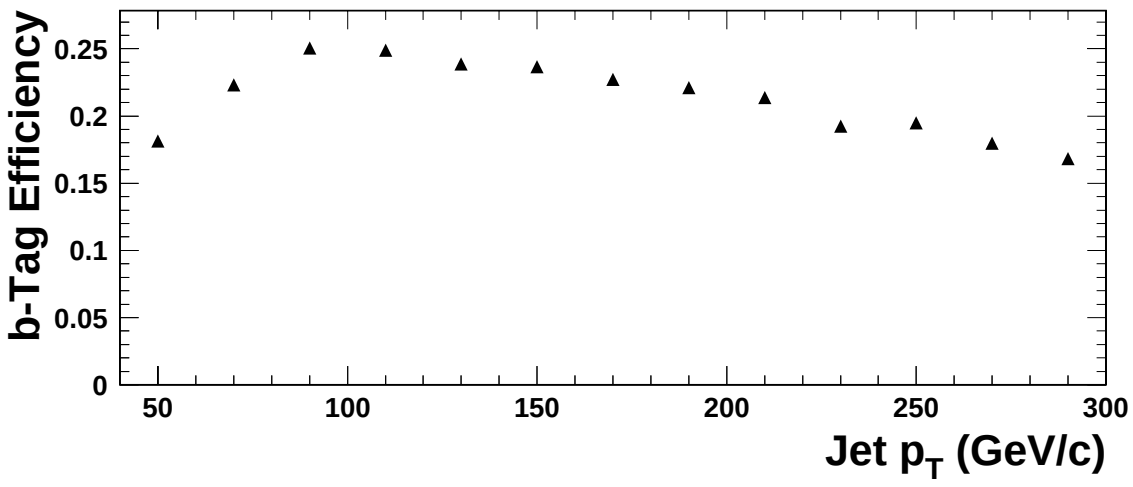

Figure 4.6

The efficiency for tagging a b-jet from the decay $Z' \to b\bar{b}$.

the simulated efficiency as a function of jet p_T.

4.4 Composition of the tagged sample

Heavy flavor generic jets are produced in hadronic collisions predominantly via three subprocesses:

- Direct production: the production of two heavy quarks in the hard scattering process.
- Gluon splitting: the next-to-leading order production of a heavy quark pair from the splitting of a final state gluon.
- Flavor excitation: a class of next-to-leading order processes that arises from gluon splitting in the initial state.

Examples of Feynman diagrams for each subprocess is shown in Figure 4.7. In addition to real heavy flavor, which includes contributions from charm as well as

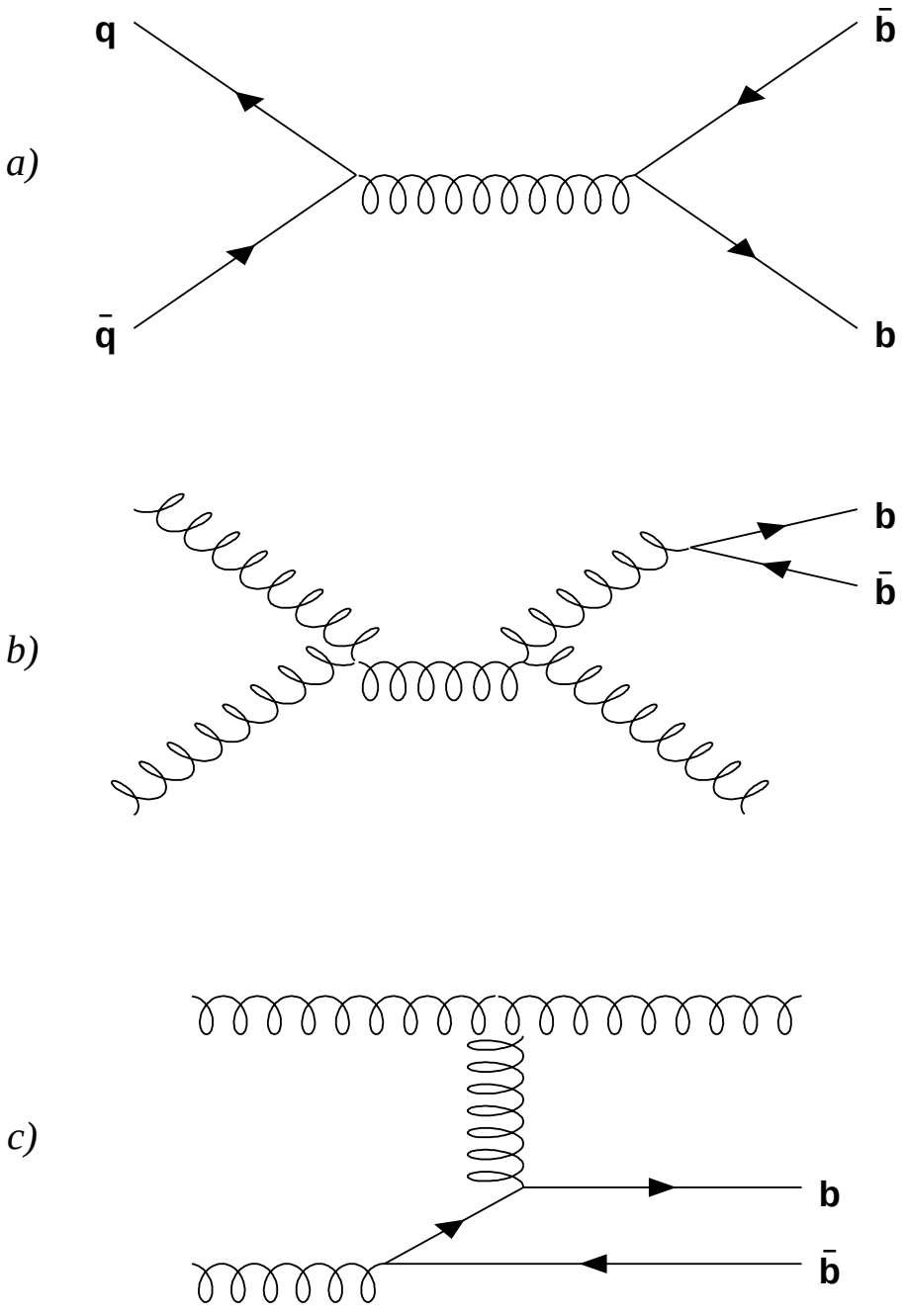

Figure 4.7

Examples of Feynman diagrams for three different phenomenological $b\overline{b}$ production mechanisms in generic jet events: a) direct $b\overline{b}$ production, b) gluon splitting, and c) flavor excitation.

bottom, the sample of jets tagged by the SECVTX algorithm contains a background contribution from non heavy-flavor jets.

Like b-quarks, charm quarks also have an appreciable lifetime, about $\tau_c \approx .15$ ps. Since the decay length of a particle is given by $\beta\gamma c\tau$, where β is the particle velocity and γ is the Lorentz factor $(1-\beta^2)^{-\frac{1}{2}}$ in the lab frame, it's convenient to use the variable $c\tau$, the particle's *proper decay length*:

$$c\tau = L_{xyz} \cdot \frac{M}{p} \tag{4.1}$$

since the decay length can be directly measured. L_{xyz} is the particle's three dimensional decay length in the lab frame and $\frac{M}{p}$ gives the Lorentz factor $\frac{1}{\beta\gamma}$ [‡]. B-hadrons typically have a proper decay length of ~ 460 μm while the proper decay length of C-hadrons is somewhat less: $c\tau(D^{\pm}) = 317\mu$m and $c\tau(D^0) = 124.4\mu$m [60]. Because C-hadrons have a shorter lifetime (and thus decay length), the charm tagging efficiency is expected to be smaller than the bottom tagging efficiency. The smaller decay length means the tracks emanating from a c decay will be less displaced, and therefore less likely to pass the cut on impact parameter significance imposed by the SECVTX algorithm. Also, B-decays generally have higher track multiplicities, and cascade $b \to c$ decays will result in a tertiary vertex that will indirectly contribute to the total number of displaced tracks in b-jets. A previous study of tagging efficiencies in the JET 20 and JET 50 samples using a similar algorithm found the

[‡]Due to CDF's inferior resolution of the z-coordinate compared to the precise $r-\phi$ resolution obtained from the SVX, the *effective decay length*, $c\tau_{eff}$, calculated from the two dimensional decay length, L_{xy}:

$$c\tau = L_{xy} \cdot \frac{M}{p_T F} \tag{4.2}$$

is used instead where L_{xy} and $\frac{M}{p_T}$ are the decay length and the Lorentz boost in the plane perpendicular to the beam line and F is a factor used to correct for decay products that are not reconstructed.

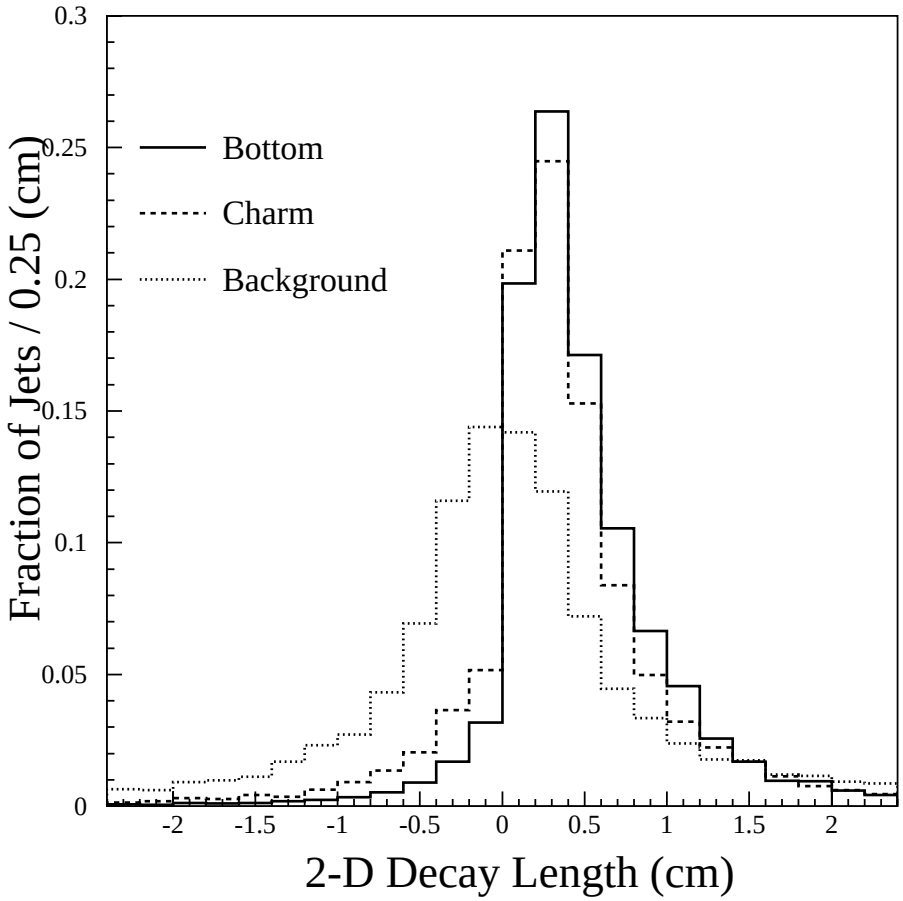

Figure 4.8

The two-dimensional decay length (L_{xy}) distributions, from simulations of tagged b-jets (solid line), c-jets (dashed line), and non heavy flavor jets (dotted line).

ratio of b to c tagging efficiencies to be ≥ 4 [61], while the ratio of b to c jets clustered with a cone size of 0.7 is expected to be ≥ 0.6 in the jet E_T range considered here [62], thus it can be concluded that charmed particles comprise a small portion but non-negligible portion of the tagged sample of jets.

Background tags from non heavy-flavor jets result from poorly measured tracks, and low p_T stray tracks from minimum bias events. The distribution of secondary

vertices from non-heavy flavor jets in the azimuthal plane will be symmetrically distributed about the primary vertex since vertices that appear to be displaced from the primary vertex due to poor resolution are just as likely to be displaced in the direction opposite the jet's momentum as they are to be displaced in the direction of the jet momentum. A long lived particle, on the other hand, will travel in the direction of the jet before decaying, and will nearly always leave a secondary vertex that is displaced from the primary vertex in the direction of the jet's momentum, unless it is mismeasured. This suggests a simple method for estimating the number of mistags: if we attribute a sign to the 2-dimensional decay length, where the sign is taken to be the dot product of a vector pointing from the primary vertex to the secondary vertex with the direction of the jet axis, then assuming that tags with a negative-signed L_{xy} are all background, and that the background distribution is symmetric about $L_{xy} = 0$, as shown in Figure 4.8, the number of positive tags from real heavy flavor can be estimated by subtracting the number of negative tags from the number of positive tags. The L_{xy} distribution of tagged jets from events passing the dijet event selection cuts described in Chapter 3 are shown in Figure 4.9, where the excess of positive tags indicates the presence of real heavy flavor.

The azimuthal separation of pair-produced B-hadrons can distinguish between different heavy-flavor different production mechanisms. Since gluon splitting arises from the splitting of a gluon within a jet, both b quarks produced are expected to be collinear and will thus occupy the same jet. The azimuthal separation ($\Delta\phi$) of b-jets from gluon splitting is therefore peaked at small angles, as shown on the bottom of Figure 4.10. When gluon splitting occurs within a dijet, it usually results in only one tagged jet, except in the rare case where gluon splitting occurs in both jets. Flavor excitation results in a flat $\Delta\phi$ distribution, as shown in the center of Figure 4.10, while direct production produces b-jets that are peaked back-to-back.

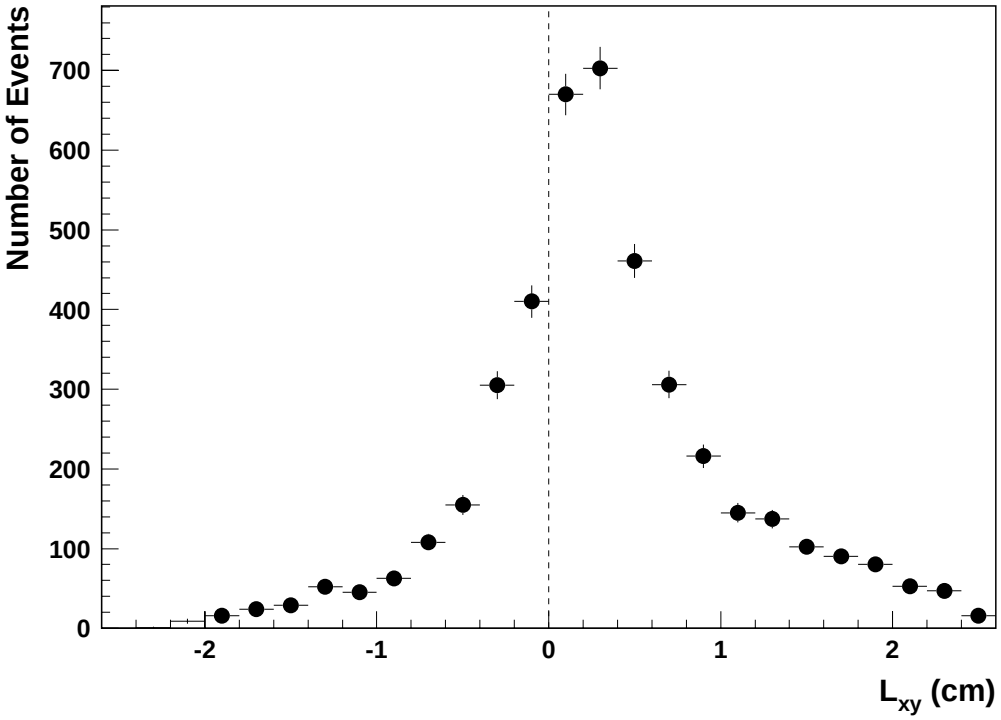

Figure 4.9

The two-dimensional decay length (L_{xy}) measured from single tagged data events.

4.5 Optimization

While the exact amount of background is not crucial to the analysis, since we do not perform an explicit background subtraction but instead look for deviations in the expected shape of the smoothly falling $b\bar{b}$ distributions, any reduction in background will increase the sensitivity of the method. Since we seek a final state with two high p_T b-jets, we seek here to minimize the contribution from mistags and charm, and favor b-production mechanisms that result in two distinct b-jets in the final state.

We require both jets in the dijet to be tagged by SECVTX [54, 55]. This sig-

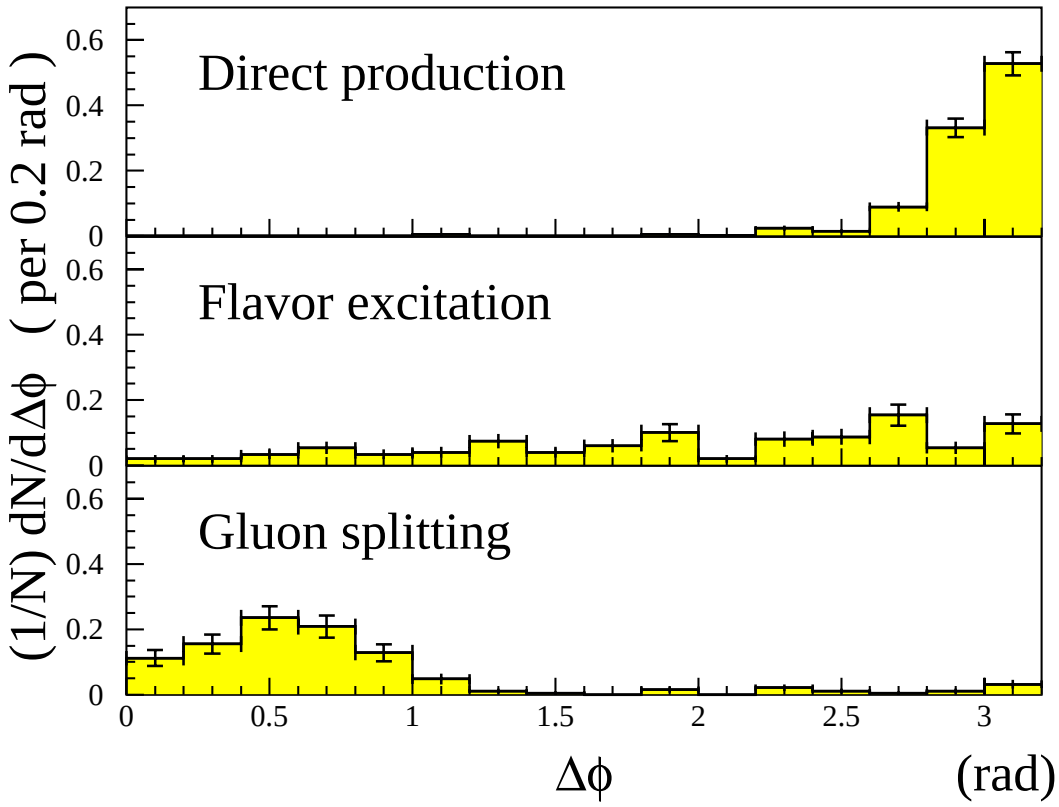

Figure 4.10

The $\Delta\phi$ distribution of simulated double-tagged dijet events from three different production mechanisms: direct production (top), flavor excitation (middle), and gluon splitting (bottom).

nificantly reduces the number of mistags, and, since the charm tagging efficiency is lower than the b-tagging efficiency, we expect that requiring both jets to be tagged will increase the b to c ratio in the sample. Since, as described above, gluon splitting will tend to produce collinear B-hadrons, this requirement will remove much of the contribution from that process. The double tagged spectrum is dominated by directly produced $b\bar{b}$ pairs as shown in Figure 4.11.

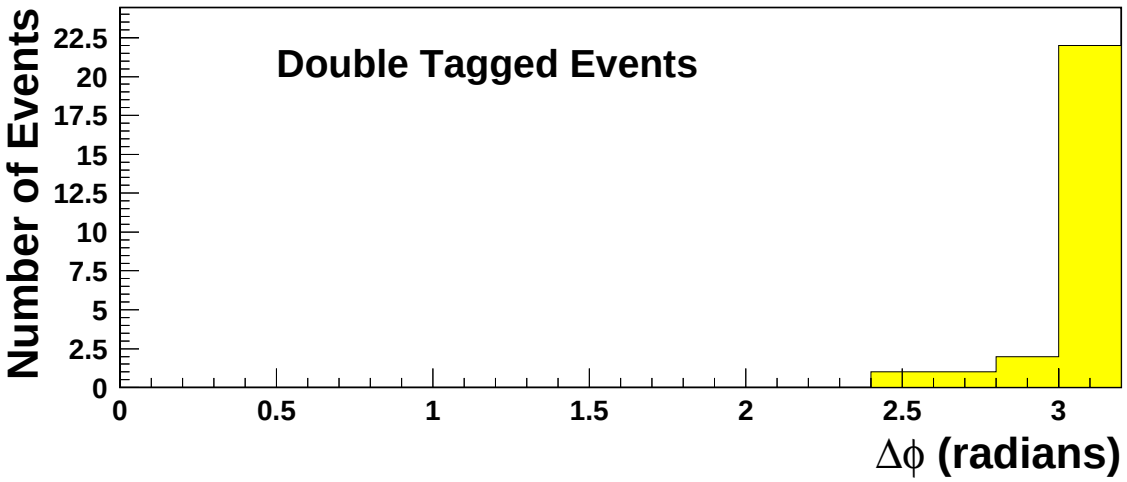

Figure 4.11

The azimuthal separation of the jets in the dijet in the double-tagged spectrum. The jets are back-to-back, indicating that the cuts favor direct b production.

Although for optimal energy resolution a cone size of 0.7 was used to cluster jets, only tracks within a cone radius of 0.4 were used by SECVTX to form a secondary vertex, since the high E_T jets used in this analysis are expected to be very collimated. For additional background suppression, we tightened the default P_T cuts for tracks used in a secondary vertex for high mass dijets. Since the dijets in our spectrum span a broad range of masses, the track p_T cuts are incremented as a function of dijet mass as shown in Table 4.2. Because we gradually vary the P_T requirements, the efficiency remains a smooth function of dijet mass. For the E_T of the jets considered, these cuts are minimal, since we wished to avoid sculpting the background. An event with a dijet mass of 408 GeV/c^2 that passes all kinematic and tagging requirements is shown in Figure 4.12.

The b-tagging efficiency for the degraded Monte Carlo is plotted as a function

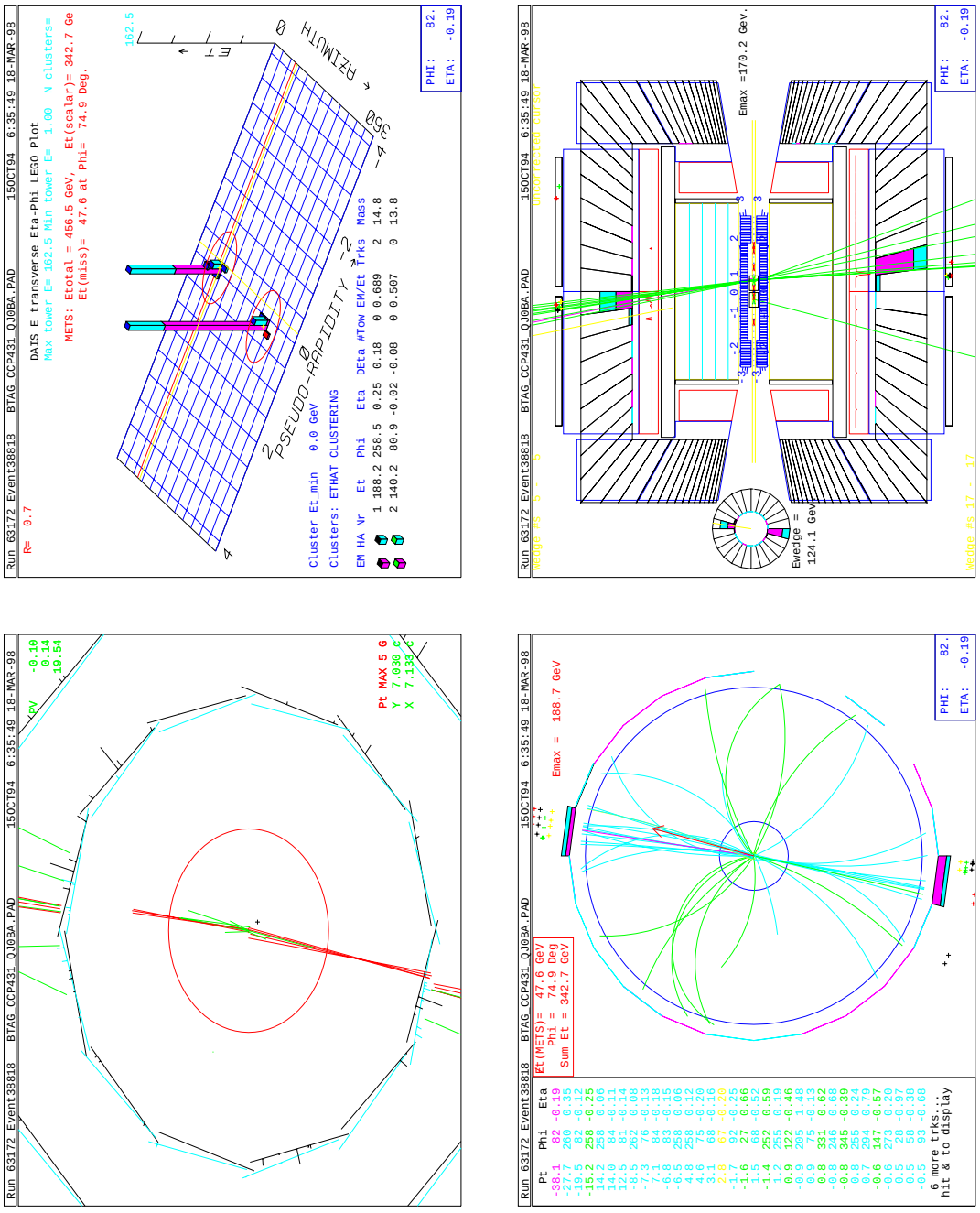

Figure 4.12

Display of a double tagged dijet event with dijet mass of 408 GeV. Upper Left: The primary and secondary event vertices and their associated tracks. For scale, the beam pipe is 1 cm in diameter. The innermost layers of silicon can be seen on the edges of the panel. Lower Left: Reconstructed tracks in the Central Tracking Chamber which has an outer radius is 1 m. Upper Right: The transverse energy and the $\eta - \phi$ location of the two jets. Lower Left: A cross sectional view of the event in the CDF detector.

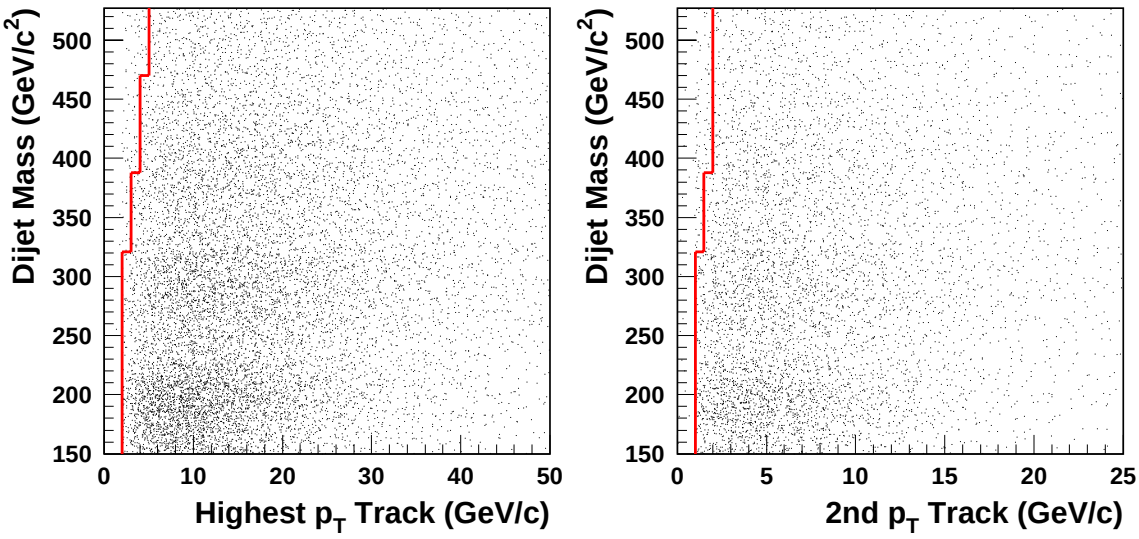

Figure 4.13

For single tagged Monte Carlo $Z' \to b\overline{b}$ events, the p_T of the highest p_T (left) and second highest p_T (right) track is shown versus dijet mass.

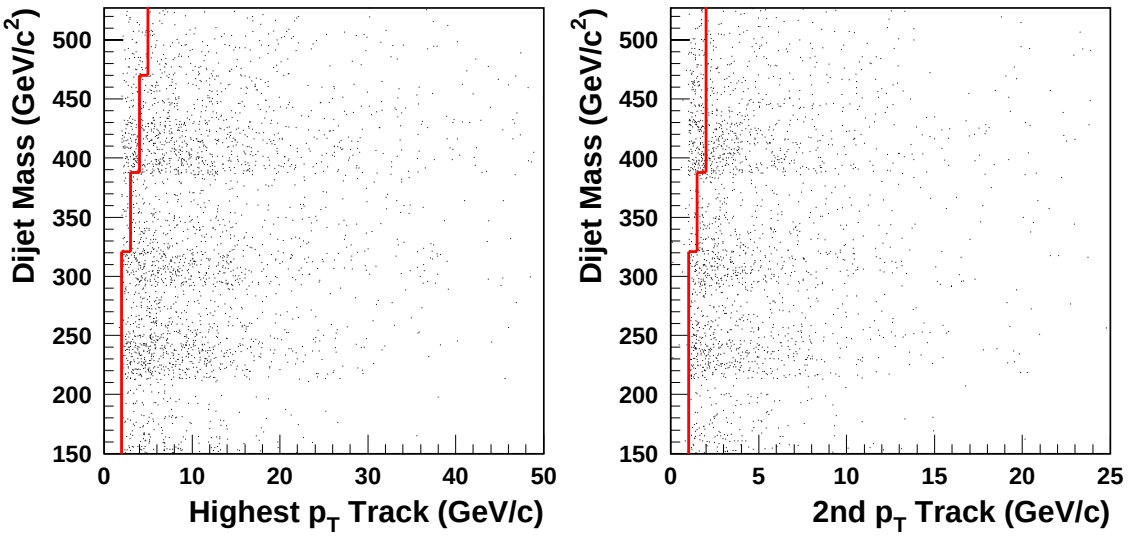

Figure 4.14

For single tagged jet data events, the p_T of the highest p_T (left) and second highest p_T (right) track is shown versus dijet mass.

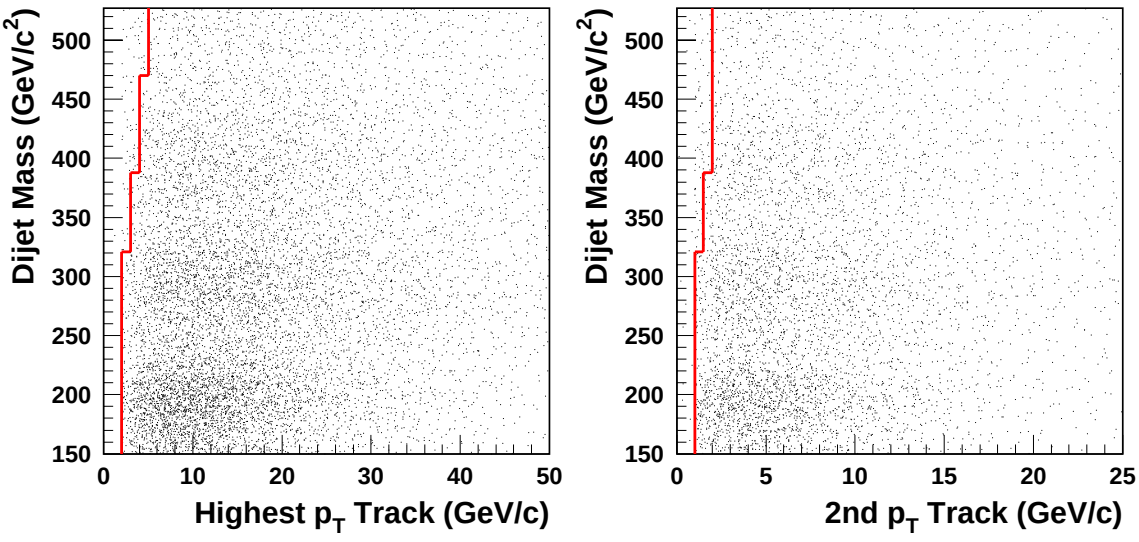

Figure 4.15

For double tagged Monte Carlo $Z' \to b\overline{b}$ events, the p_T of the highest p_T (left) and second highest p_T (right) track is shown versus dijet mass.

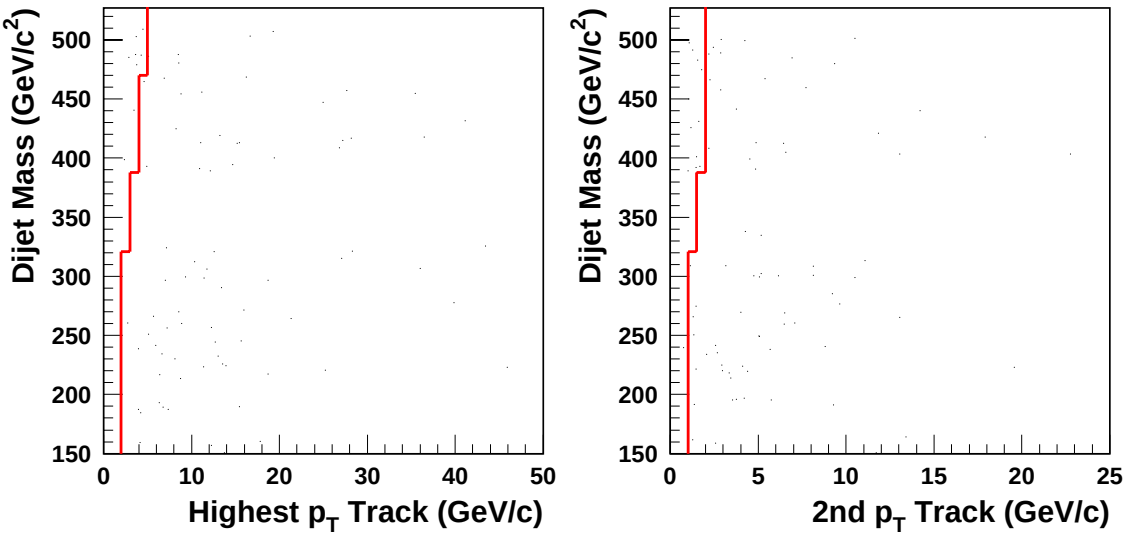

Figure 4.16

For double tagged jet data events, the p_T of the highest p_T (left) and second highest p_T (right) track is shown versus dijet mass.

	Single Tags		**Double Tags**	
Mass bin	Default p_T cuts	Tightened p_T cuts	Default p_T cuts	Tightened p_T cuts
150-163	68	68	2	2
163-180	59	59	0	0
180-198	35	35	3	3
198-217	31	31	0	0
217-241	362	362	7	7
241-265	216	216	4	4
265-292	137	137	3	3
292-321	391	391	4	4
321-353	227	196	1	1
353-388	152	127	0	0
388-427	607	426	7	5
427-470	309	220	5	1
470-517	195	131	6	2
517-568	100	75	2	1
568-625	62	40	2	1
625-688	14	10	0	0
688-756	7	6	0	0
756-832	4	3	0	0
832-915	3	2	0	0
915-1007	0	0	0	0
1007-1108	1	1	0	0

Table 4.1

The number of single (double) tagged events in the spectrum with default SECVTX p_T cuts compared to tightened SECVTX p_T cuts.

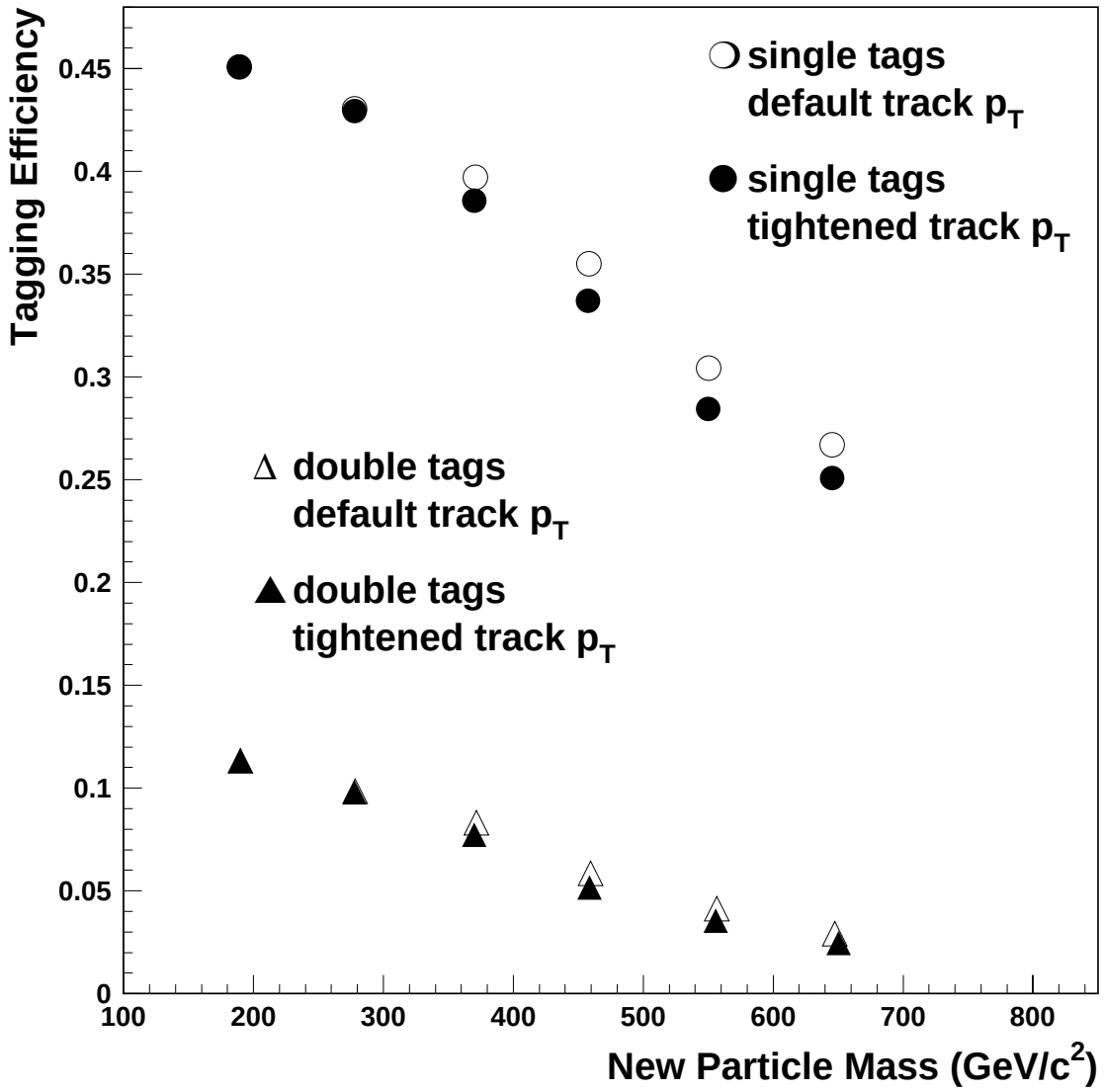

Figure 4.17

The b-tagging efficiency as a function of dijet mass for double tags with (hollow triangles) and without (shaded triangles) tightened p_T requirements. Also shown for comparison is the b-tagging efficiency for single tags with (hollow circles) and without (shaded circles) tightened p_T requirements.

Dijet Mass	3 Track Vertex		2 Track Vertex	
	Highest p_T track	Other tracks	Highest p_T track	Other tracks
150-321 GeV	2.0 GeV	0.5 GeV	2.0 GeV	1.0 GeV
321-388	3.0	0.5	3.0	1.5
388-470	4.0	0.5	4.0	2.0
470-up	5.0	0.5	5.0	2.0

Table 4.2

Minimum p_T requirement for tracks used in a reconstructed vertex tag.

of dijet mass in Figure 4.17. The generated events were required to pass the same kinematic and tagging cuts required for the real data, therefore the efficiencies shown in Figure 4.17 reflect the total tagging efficiency for all events passing the Z-vertex cut, not just the the efficiency for events that are SVX fiducial. The tagging efficiencies are shown for both the default SECVTX cuts and the tightened p_T from Table 4.2 that are used in this analysis. After the application of the track p_T cuts, the tagging efficiencies remain smooth as a function of mass, and the impact of the tightened cuts are shown to be minimal for heavy particle decays. The distribution of the p_T of SECVTX tagged tracks in data and Monte Carlo for single and double tagged tracks are shown in Figures 4.15 - 4.16, where the solid lines show the track p_T cuts. Taken together, these cuts provide powerful background suppression.

	Data		Monte Carlo	
Parameter	Value	Error	Value	Error
A	8713.0×10^9	7411.0×10^9	4312.9×10^9	103.56×10^9
p	5.1601	0.901×10^{-1}	5.2267	0.401×10^{-3}
N	12.556	6.6728	7.2899	0.21129
c	0.98564	0.253×10^{-3}	0.31526	0.498×10^{-1}

Table 4.3

The best fit to the parameters A, p, N, and c in Equation 3.11, for the double tagged data and direct $b\bar{b}$ Monte Carlo.

4.6 The $b\bar{b}$ Mass Spectrum

Once the dijet sample is b-tagged, the $b\bar{b}$ mass spectrum, the differential of the dijet cross-section with respect to dijet invariant mass is plotted with bin widths that are comparable to the dijet mass resolution ($\sim 10\%$), as shown by the circles in Figure 4.18. The plotted values of the cross section and their statistical errors, determined using Poisson statistics, along with the corresponding raw number of events in each bin, are listed in Table 4.4. The spectrum has been corrected for b-tagging efficiency using the values shown in Figure 4.17. The data is compared to a leading order simulation of the direct $b\bar{b}$ spectrum which is shown on the same plot by the squares. A renormalization scale of μ = m, where m is the mass of the system, was used in the simulation for running of α_s and the evolution of the parton distributions. This choice defines the overall normalization of the spectrum, however, the shape of the simulated spectrum is only sensitive to this choice at a

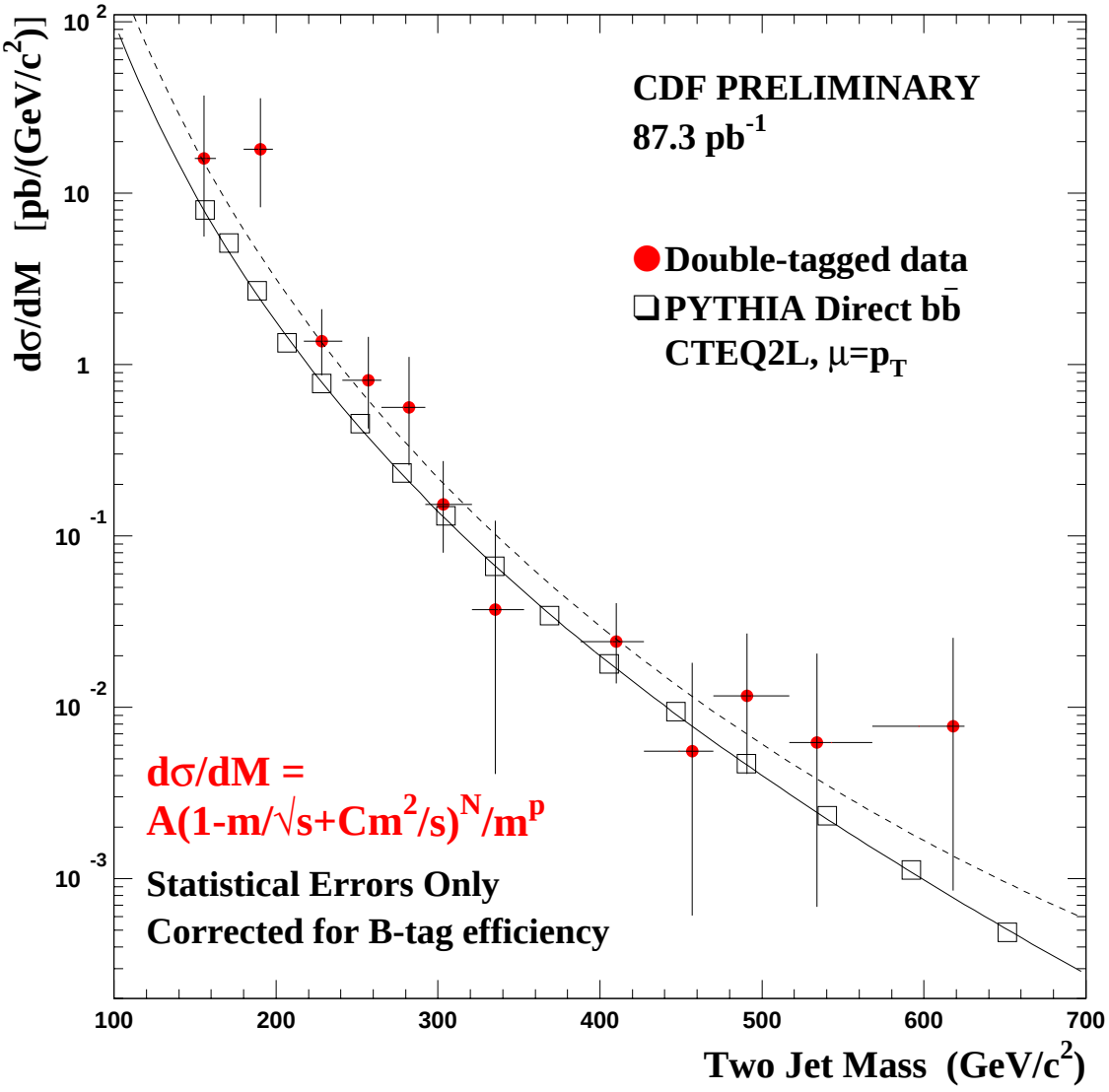

Figure 4.18

The CDF Run IB dijet mass spectrum with both jets b-tagged compared with PYTHIA direct $b\bar{b}$ Monte Carlo with the renormalization scale $\mu = m$ and CTEQ2L parton distribution functions. The spectra are fit to a smooth background parameterization of the form $d\sigma/dm = A\,(1 - m/\sqrt{s} + cm^2/s)^N/m^p$. The mass bins with zero events are not shown on the log plot.

Trigger	Mass bin GeV/c^2	Mean Mass (GeV/c^2)	Number of Events	Cross-section (pb/GeV) ± statistical errors
JET 20	150-163	155.4	2	$1.9^{+2.5}_{-1.2}$
	163-180	171.5	0	$0.0^{+1.3}_{-0.0}$
	180-198	190.3	3	$2.1^{+2.0}_{-1.1}$
	198-217	207.5	0	$0.0^{+1.2}_{-0.0}$
JET 50	217-241	228.1	7	$(1.5^{+0.8}_{-0.5}) \times 10^{-1}$
	241-265	257.0	4	$(8.2^{+6.5}_{-3.9}) \times 10^{-2}$
	265-292	282.2	3	$(5.5^{+5.3}_{-3.0}) \times 10^{-2}$
JET 70	292-321	303.2	4	$(1.4^{+1.1}_{-0.7}) \times 10^{-2}$
	321-353	335.2	1	$(3.2^{+7.3}_{-2.8}) \times 10^{-3}$
	353-388	370.5	0	$(0.0^{+5.4}_{-0.0}) \times 10^{-3}$
JET 100	388-427	410.1	5	$(1.6^{+1.1}_{-0.7}) \times 10^{-3}$
	427-470	456.9	1	$(2.9^{+6.6}_{-2.6}) \times 10^{-4}$
	470-517	490.7	2	$(5.2^{+6.9}_{-3.4}) \times 10^{-4}$
	517-568	534.0	1	$(2.4^{+5.5}_{-2.2}) \times 10^{-4}$
	568-625	617.9	1	$(2.2^{+4.9}_{-1.9}) \times 10^{-4}$
	625-688	656.5	0	$(0.0^{+3.6}_{-0.0}) \times 10^{-4}$
	688-756	722.0	0	$(0.0^{+3.3}_{-0.0}) \times 10^{-4}$

Table 4.4

For each bin in the b-tagged dijet mass distribution, the mean mass, the raw number of events, and the cross section ± statistical errors are given.

level of 1%. We only compare the spectra to seek any fluctuation in the shape that could be consistent with a resonance, thus, the choice of renormalization scale is somewhat arbitrary.

Both spectra are parameterized using Equation 3.11, the same equation that was used in Section 3.6 to characterize the shape of the dijet mass distribution. The parameters which give the best fit to the double tagged spectrum and the Monte Carlo direct $b\bar{b}$ spectrum are shown in Table 4.3. The shape of the data agrees well with the shape of the direct $b\bar{b}$ simulation, except for the overall normalization. In order to compare the shape of the Monte Carlo spectrum to the data, we first fit the Monte Carlo $b\bar{b}$ spectrum with the parameterization of Equation 3.11. The fit results for p, N, and c yield the shape of the smooth curve in Figure 4.19 while the normalization, A, is determined by the data. The inset shows the fractional difference between the data and the fit on a linear scale by dividing the difference between the data and the fit by the fit. The fit gives a $\chi^2/d.f.$ of 0.61.

It is also instructive to compare the double tagged dijet mass spectrum to the spectra of single tagged and untagged events for two reasons. First, if there is an upward fluctuation in one of the distributions, it is interesting to note whether it is reflected in all three. If so, this could indicate that either there is just a statistical fluctuation in the jet data that is propagated to the $b\bar{b}$ spectrum, or, in the case that there is a real new particle resonance, whether it is coupled preferentially to the third generation. Second, the $b\bar{b}$ may include background from common dijets or dijets containing heavy flavor in only one jet, thus the shape of the background contribution may be inferred from the relative shapes of the spectra. The double tagged spectrum is shown in Figure 4.20 along with the untagged dijet and the single tagged dijet spectra (note that the b-tagged spectra are not corrected for tagging efficiency). The number of events in each bin are listed for each of the

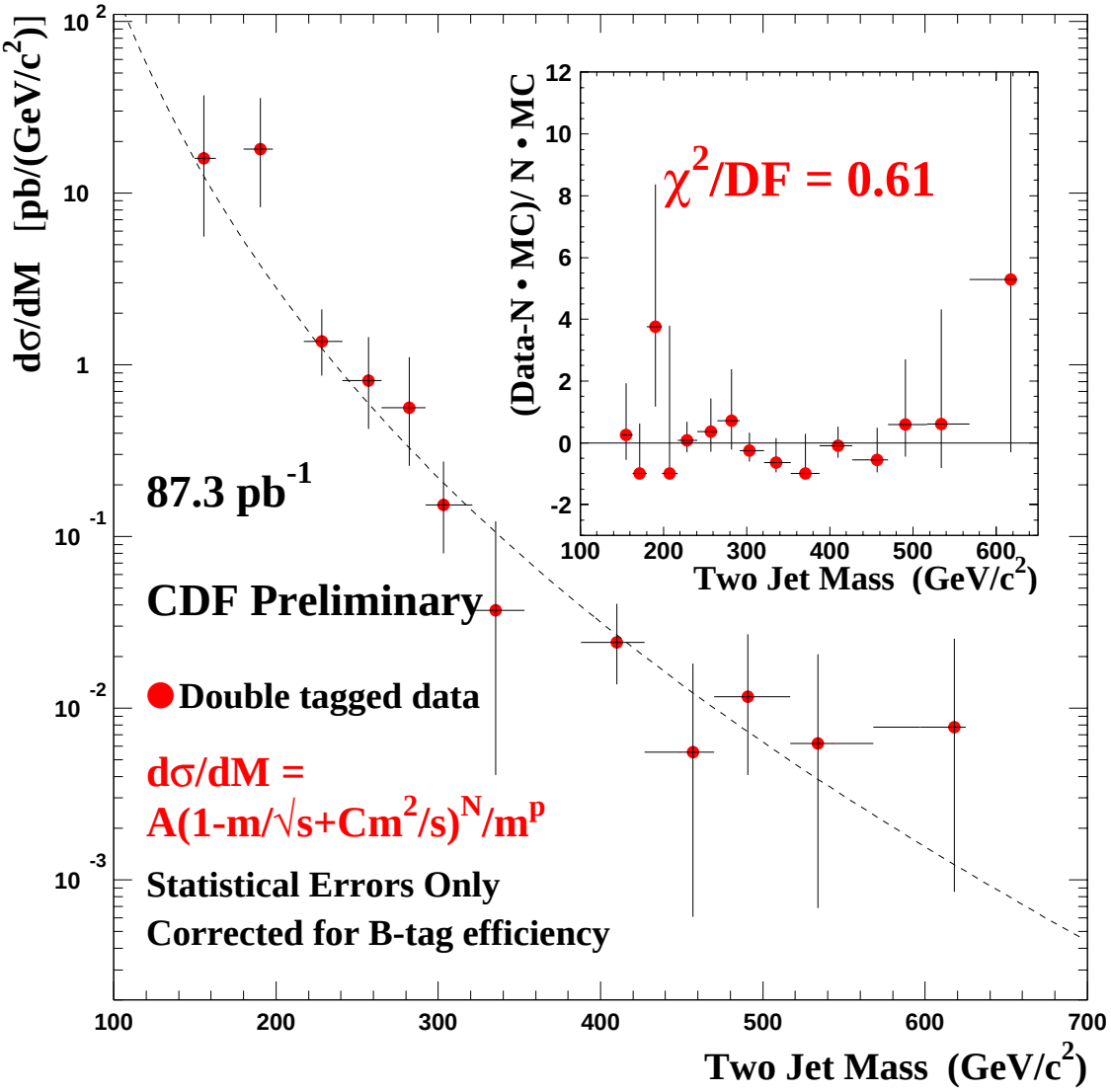

Figure 4.19

The Run IB double b-tagged spectrum fit to the direct $b\bar{b}$ Monte Carlo spectrum normalized by a factor N. The inset shows the fractional difference between the data and the normalized Monte Carlo.

spectra are listed in Table 4.5. Once corrected for b-tagging efficiency, the shape of double-tagged spectrum agrees with the shape of the untagged spectrum (except for a normalization, of course). A direct comparison of the shape of the untagged spectrum by fitting the $b\bar{b}$ to the parameterization of the untagged spectrum, but letting the normalization float, yields a fit with $\chi^2/d.f.$ of 0.61.

The $b\bar{b}$ spectrum appears to be both smooth steeply falling and agrees with Monte Carlo simulations of direct $b\bar{b}$ production to within our statistical errors, however, in order to make a quantitative statement about the inclusion or exclusion of new physics in our spectrum, we must first study how such a resonance would effect the distribution. In the following chapter, we describe simulations of new particle resonances as they would appear in the CDF detector.

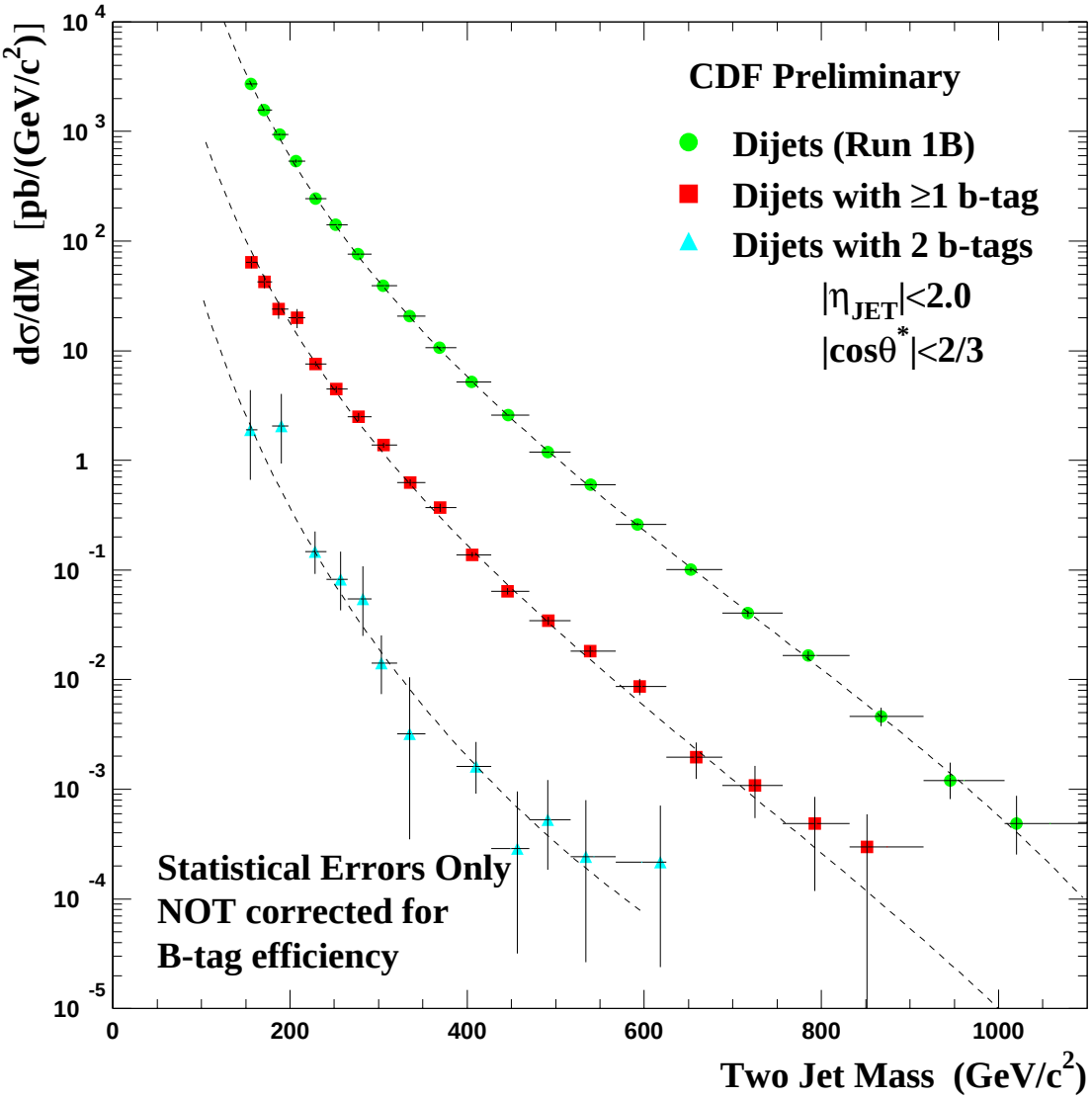

Figure 4.20

The CDF Run IB dijet mass spectrum with both jets b-tagged (triangles), as compared to the untagged spectrum (circles) and the single tagged spectrum (squares). The spectra are fit to a smooth background parameterization of the form $d\sigma/dm = A\,(1 - m/\sqrt{s} + Cm^2/s)^N/m^p$.

Trigger	Mass bin GeV/c^2	Untagged Dijet	b-tagged Dijet	Double Tagged
JET 20	150-163	2875	68	2
	163-180	2166	59	0
	180-198	1374	35	3
	198-217	825	31	0
JET 50	217-241	11592	362	7
	241-265	6831	216	4
	265-292	4165	137	3
JET 70	292-321	11046	391	4
	321-353	6440	196	1
	353-388	3649	127	0
JET 100	388-427	16010	426	5
	427-470	8921	220	1
	470-517	4537	131	2
	517-568	2492	75	1
	568-625	1209	40	1
	625-688	517	10	0
	688-756	222	6	0
	756-832	102	3	0
	832-915	31	2	0
	915-1007	9	0	0
	1007-1108	4	0	0

Table 4.5

Number of events in each bin in the dijet, b-tagged dijet, and double-tagged distribution.

5. RESONANCE SIMULATIONS

Now that we have a $b\bar{b}$ mass spectrum, we must study how the presence of a new particle would modify the mass distribution in order to make a quantitative statement about the inclusion or exclusion of new physics. Since we wish to set a cross section upper limit on the production of a new particle, we parameterize the shape by simulating the dijet mass distribution using a Monte Carlo, then divide the cross section in each bin by the total cross section in the resonance peak. This gives the fraction of the signal in each bin, which can then be multiplied by the theoretical production cross section, giving the expected dijet mass distribution for a particular particle. We use PYTHIA to simulate the new particle signal with the B-mesons redecayed by QQ, and QFL' to simulate the effects of detector smearing. A description of the Monte Carlo packages and how they were used can be found in Appendix B.

We use the $b\bar{b}$ mass spectrum to set limits on a variety of new particles. First, we seek particles which would produce a resonance that is narrower than the dijet mass distribution. In this case, the dijet mass resolution, which is $\sim 10\%$ will dominate the shape of the resonance, thus, the shape of all such new particle resonances (although not the cross section) will be the same after detector smearing. Also, we apply the same kinematic cuts to the Monte Carlo simulations as we did to the data so the kinematic acceptance is already taken into account. Therefore, we only simulate one narrow resonance distribution, and the cross section limits obtained will be applicable to any narrow particle. We also seek topgluons, which have a width

that is not tightly constrained by the theory, although, according to Equation 1.36, the theory favors a relatively wide width to provide the top quark with it's observed heavy mass. Since the dijet mass resolution will not likely dominate the shape of a topgluon resonance, we must do a separate simulation for each width we seek. The cross section upper limit obtained for topgluons will therefore be a function of the width as well as the mass.

5.1 Narrow Resonances

To parameterize the shape of narrow resonances we simulate the decay $Z' \to b\overline{b}$ for new particle masses of 200, 400, 600, and 800 GeV. A lower mass cut was placed on the generated mass at 80% of the nominal value. The events were then processed in the same manner as the data, only we have used jet corrections that are specifically designed for Monte Carlo events, which account for the differences between the detector simulation and the real detector performance. The shape of a narrow resonance after detector smearing is shown in Figure 5.1. The parameterization is given as the fraction of the signal in each bin width divided by the width of the bin, Δm. The tail at low mass results from semileptonic b decays and QCD radiation off the final state.

5.2 Topgluon Resonances

The phenomenology of topgluons combined with a lack of theoretical constraints make the topgluon simulation much more challenging. First, Equation 1.35 provides for a mixing between topgluons, g_T, and ordinary gluons, g, such that they will interfere destructively on the high mass tail of the resonance mass distribution. Therefore, we cannot simply model the resonance but we instead model a topgluon

resonance superimposed on a rapidly falling spectrum, $q\bar{q} \rightarrow (g + g_T) \rightarrow b\bar{b}$, then separately model the spectrum from direct lowest order $b\bar{b}$ production, $q\bar{q} \rightarrow g \rightarrow b\bar{b}$ and $gg \rightarrow b\bar{b}$. The contribution from direct $b\bar{b}$ production is then subtracted from the $q\bar{q} \rightarrow (g + g_T) \rightarrow b\bar{b}$ distribution. Second, since we do not know the fractional width of the topgluon, we must simulate the resonances at various width and masses in order to scan the mass-width plane. The width, as given by equation 1.36, is dependent on the parameter θ, which will change at the kinematic threshold for the topgluon decay to $t\bar{t}$. For the purpose of this search, we simulate topgluons along lines of constant width (since this is the experimentally observable variable), thus we hold the parameter θ constant through the $t\bar{t}$ threshold. We are effectively doing a scan of the available parameter space along lines of constant , .

To model topgluons, we again use PYTHIA to model $b\bar{b}$ production via an intermediate gluon, $q\bar{q} \rightarrow g \rightarrow b\bar{b}$, with a subroutine that allowed us to modify the shape of the cross section to correspond to Equation 1.35. To model the $b\bar{b}$ background, we use the same simulated spectrum shown in Figure 4.18. We simulate topgluons at masses of 200, 400, 600, and 800 GeV at fractional widths of , $/M = 0.3$, 0.5, and 0.7. These were chosen since the large mass of the top quark requires a large θ, so we do not expect the topgluon to be much narrower than , $/M = 0.3$, and our sensitivity degrades as the width increases, thus we cannot exclude a resonance with a larger width than , $/M = 0.7$.

The topgluon mass distribution is shown in Figure 5.2 at parton level and Figure 5.3 after detector smearing. In each of these Figures, the topgluon resonances at various widths superimposed on $b\bar{b}$ background are shown in the upper left, with the solid line indicating the level of the background. The upper right panel shows the net cross section from topgluon production after the background has been subtracted. On the lower left, the fractional contribution from topgluon production, obtained by

dividing the net topgluon production cross section by the $b\bar{b}$ background, is shown. Finally, the topgluon cross section is parameterized in the lower right as the fraction of the topgluon signal in each bin.

Because the parton distribution functions rapidly increase as the mass decreases, the cross section for topgluons continually increases as you move toward the low mass tail, even as the contribution to the cross section from topgluons relative to the background is decreasing! The cross section is therefore only clearly defined in a mass window, so we normalize the fractional parameterization to 1 in a window between $\pm 50\%$ of the generated topgluon mass. This choice of mass window was chosen to correspond to the mass interval where the topgluon contributes a significant cross section relative to QCD. This again allows us to simply multiply by a theoretical cross section (the cross section within $\pm 50\%$ of the topgluon mass) and get the correct effect on the observed spectrum. The parameterized topgluon shapes are shown in Figure 5.4.

We now have all of the information needed to set limits on resonances in the $b\bar{b}$ spectrum. The results of the search are presented in the next chapter.

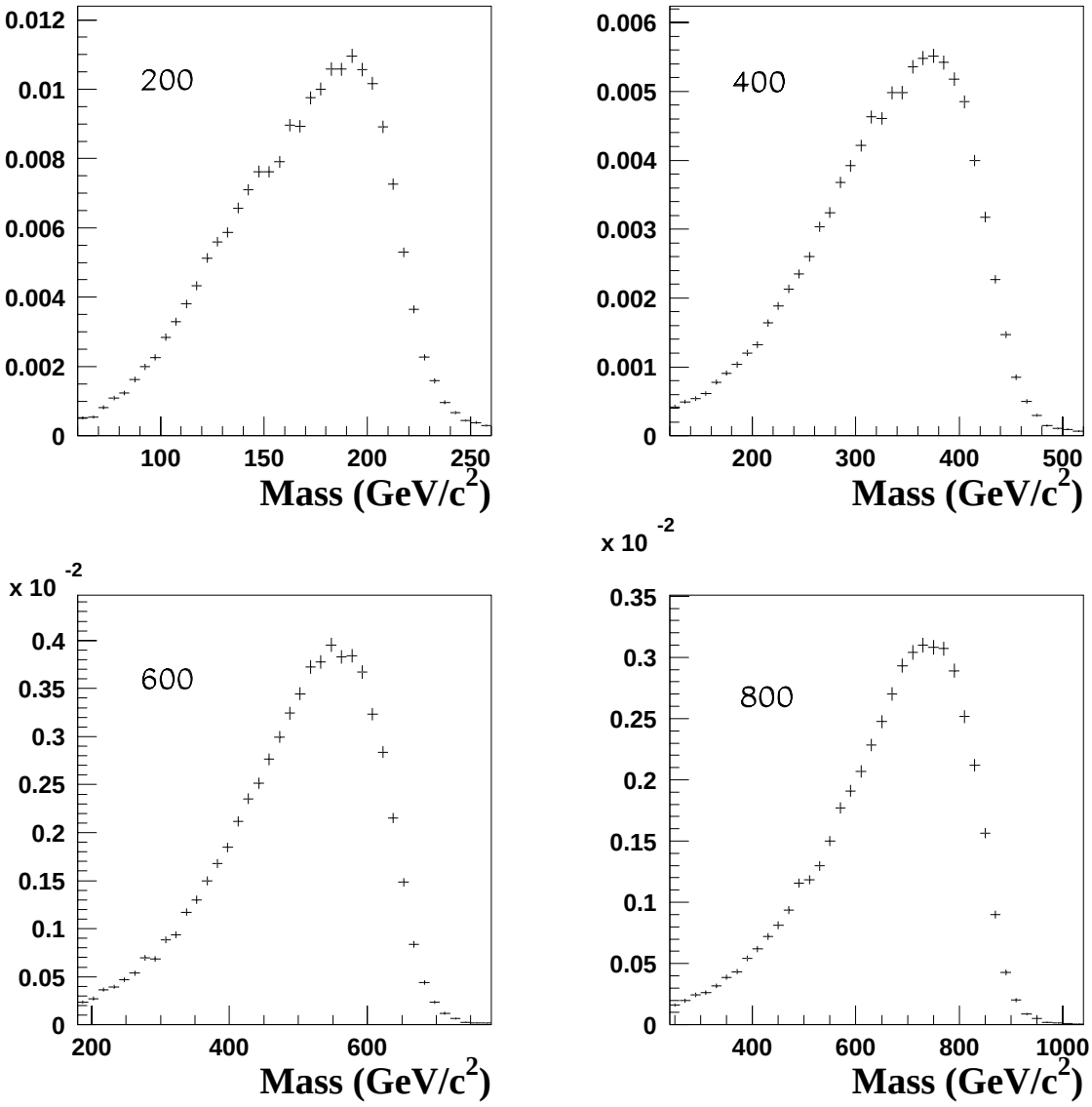

Figure 5.1

The dijet mass distribution of a narrow particle decay to $b\bar{b}$, parameterized by the fraction of the cross section in each mass bin. The tail at low mass results from semileptonic b decays and QCD radiation off the final state.

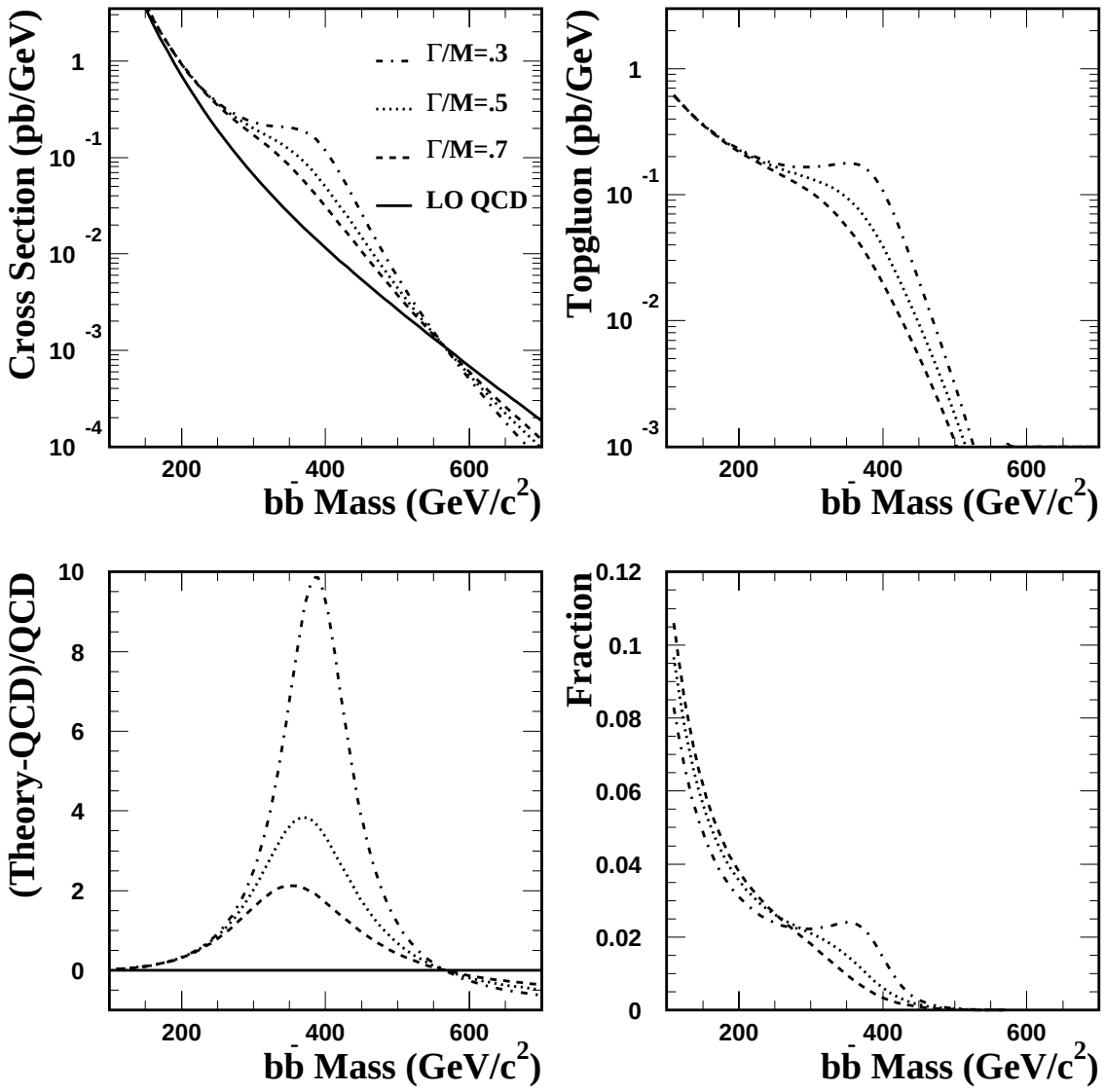

Figure 5.2

The shape of a 400 GeV topgluon resonance at parton level. (a) shows the resonance plus a smoothly falling $b\bar{b}$ background, (b) shows the resonance after the background has been subtracted, (c) shows the fractional difference between the resonance and the smooth background, and (d) shows the fraction of the (positive) signal in each data bin.

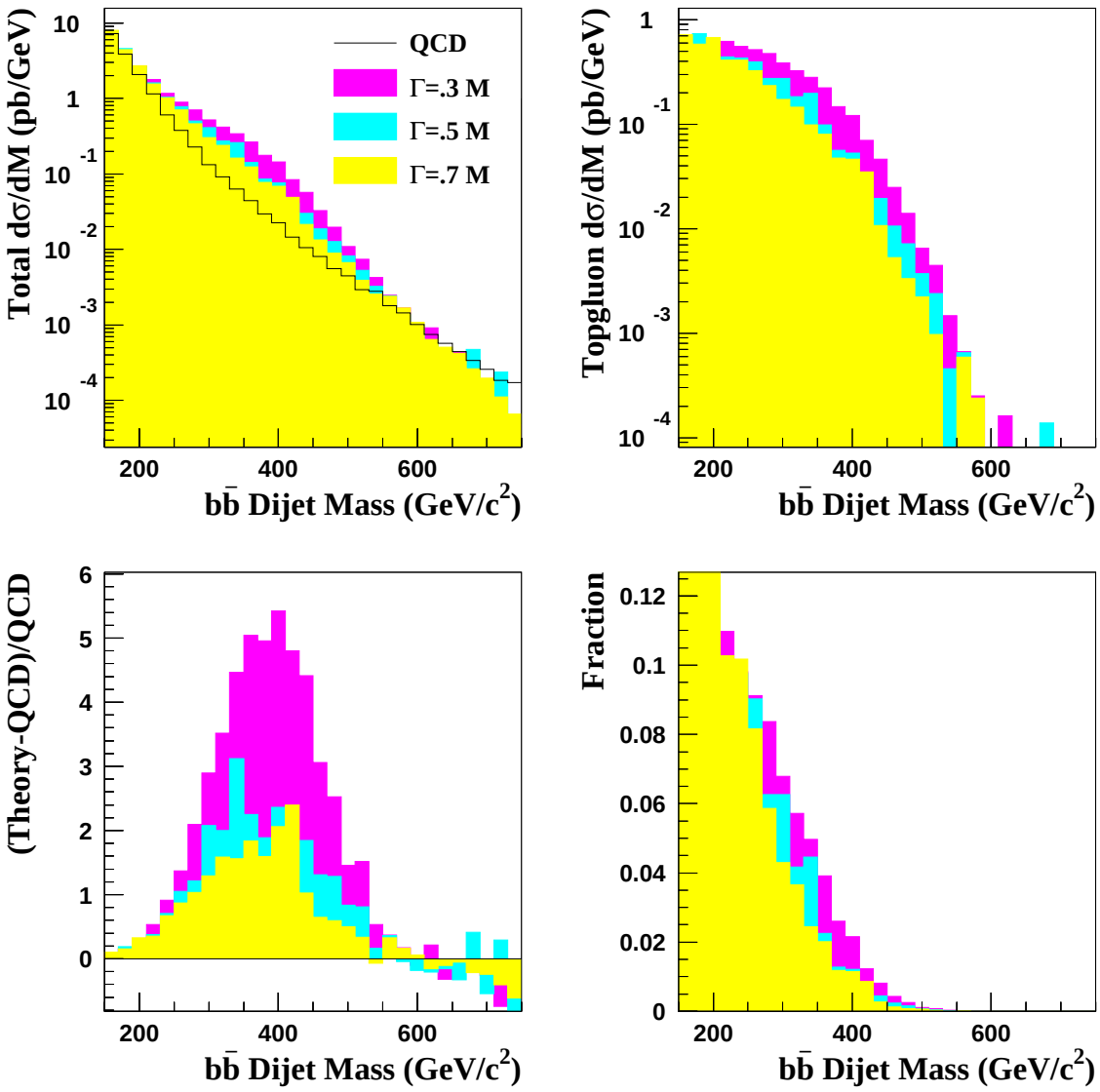

Figure 5.3

The shape of a 400 GeV topgluon resonance after detector smearing. (a) shows the resonance plus a smoothly falling $b\bar{b}$ background, (b) shows the resonance after the background has been subtracted, (c) shows the fractional difference between the resonance and the smooth background, and (d) shows the fraction of the (positive) signal in each data bin.

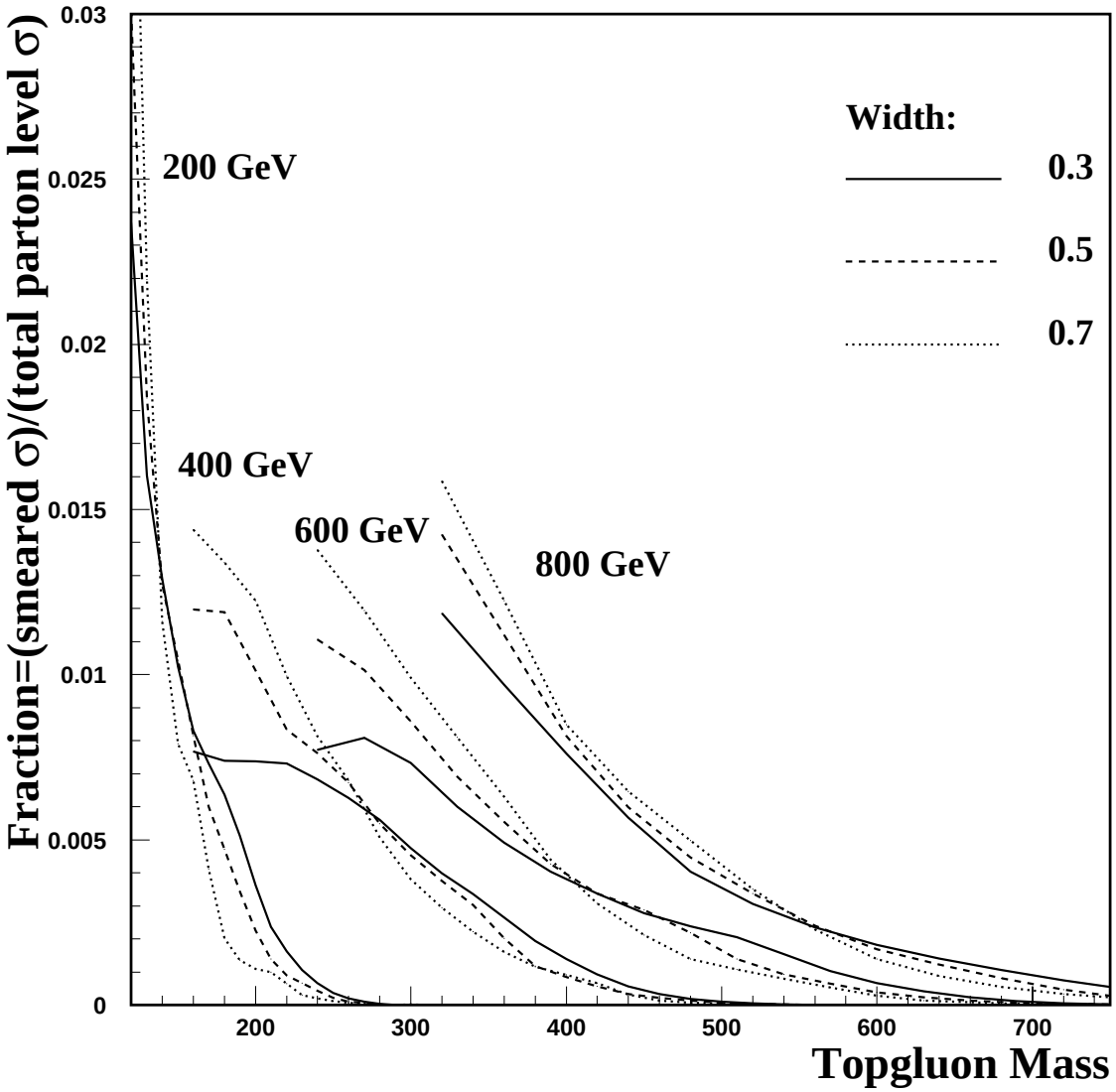

Figure 5.4

The fraction of the theoretical cross section of a predicted topgluon resonance in each bin after detector smearing for various topgluon masses and widths. The solid, dashed, and dotted lines show the fraction for topgluon widths of , = 0.3, 0.5, and 0.7 respectively.

6. LIMITS

Now that we have reconstructed the $b\bar{b}$ mass spectrum and simulated the $b\bar{b}$ mass distribution that would be produced by a new particle, we can use these distributions, along with the calculated efficiencies, to determine whether a new physics process is present in our spectrum. We use a simple technique: we allow the normalization of the background parameterization given in Section 4.6 to float, and vary the signal cross-section to find the best fit to the signal plus background. This is done in steps of 50 GeV/c^2 to obtain a cross section limit as a function of resonance mass.

6.1 Predicted Number of Events

To determine the number of events in our data that come from new physics processes, we assume that any given bin of our spectrum contains contributions from both the background $b\bar{b}$ continuum and a new particle resonance. For any physical process, the mean number of $b\bar{b}$ events expected is given by:

$$\mu = A\epsilon\mathcal{L}\sigma \cdot Br(X \to b\bar{b}) \tag{6.1}$$

where A is the acceptance of our topological cuts (on η and $\cos\theta^*$), ϵ the overall efficiency of our detector for the signal ($\epsilon = \epsilon_{btag} \cdot \epsilon_{trigger} \cdot \epsilon_{z\,cut}$), $\mathcal{L}$ the integrated luminosity of the sample, and $\sigma \cdot Br(X \to b\bar{b})$ the expected cross section times branching fraction to $b\bar{b}$. Since we applied the same topological cuts to the Monte Carlo as to the data, and only decays to $b\bar{b}$ were simulated, the acceptance and branching fraction is incorporated into the calculations, therefore, the number of

events expected in the ith bin of the $b\overline{b}$ spectrum is:

$$\mu_i = \mathcal{L} \cdot \epsilon \cdot [\alpha \cdot \mu_{Si} + \mu_{Bi}]. \tag{6.2}$$

where μ_B is the mean number of background events, μ_S the mean number of signal events, and α an additional parameter used to vary the cross section of the signal.

The number of background events in each bin μ_{Bi} is simply calculated by integrating $\frac{d\sigma}{dm}$ as parameterized by Equation 3.11 over the mass bin. Since we wish to vary the amount of signal in order to set an upper limit, we need a similar parameterization for the resonance so that we can retain the appropriate shape while varying the actual cross section. We obtained such a parameterization in Chapter 5, when we made the fractional response curves by dividing the number of signal events in each bin, Δm, of the resonance mass distribution by the total number of signal events and by Δm. We can therefore simply multiply a theoretical cross section by a fractional response curve, $f_i/\Delta m$, and get the cross section in each bin, $\frac{d\sigma}{dm}$, while preserving the resonance shape. The fractional response curves for narrow resonances is shown in Figure 5.1 and in Figure 5.4 for topgluon resonances. Thus, using these two parameterizations, we can calculate the expected cross section in each bin.

To obtain actual number of events observed in the spectrum, we must also determine the detector efficiency. The efficiency of the z-vertex cut was determined in Section 3.5 to be 93%. The other efficiencies are a function of mass. The efficiency of our b-tagging requirements as a function of dijet mass for events passing the z-vertex cut is plotted in Figure 4.17, while the efficiency of the jet triggers as a function of dijet mass is shown for each trigger in Figure 3.2. The efficiency is determined for each mass bin of the distribution by interpolating between the measured values.

6.2 Binned Maximum Likelihood Fit

We then proceed to refit the spectrum to a resonance of a given mass and width superimposed on a smooth background of the form in Equation 3.11. The probability of observing n_i events when μ_i are predicted is given by Poisson statistics:

$$P_i\left(n_i;\mu_i\right) = \frac{\mu_i^{n_i}\, e^{-\mu_i}}{n_i!} \tag{6.3}$$

We define the likelihood [63] as the product of the P_i over all the bins in the mass spectrum:

$$L = \prod_i P_i\left(n_i;\mu_i\right) = \prod_i \left[\frac{\mu_i^{n_i}\, e^{-\mu_i}}{n_i!}\right] \tag{6.4}$$

The best fit is found when the likelihood function is maximized, or equivalently when the negative of the logarithm of the likelihood function:

$$-\ln L = \sum_i \mu_i - \sum_i \left[n_i \ln \mu_i\right] + \text{constant} \tag{6.5}$$

is minimized. The minimization is performed with respect to the normalization of the background spectrum, A, and the cross-section of the signal, which is varied using α. The parameters which determine the shape of the background and resonance mass distributions are fixed to the values obtained from the simulations.

The minimization is done using the CERN library routine, MINUIT [64]. Once we find the best fit to the signal plus background, the normalization is frozen, and we plot the likelihood as a function of α as shown in Figure 6.1. The limit at the 95% confidence level is defined to be that value of α for which 95% of the area under the likelihood curve is between 0 and α, thus, there is only a 5% probability of observing a value greater than α.

Figure 6.1 shows the likelihood distributions for a 600 GeV/c^2 narrow resonance and a 600 GeV/c^2 topgluon of fractional width , $/M = 0.5$. The area under the curves between 0 and the 95% cross section limits are shaded. The likelihood distribution for the narrow resonance is peaked at $\approx$ 1 pb, indicating the a small

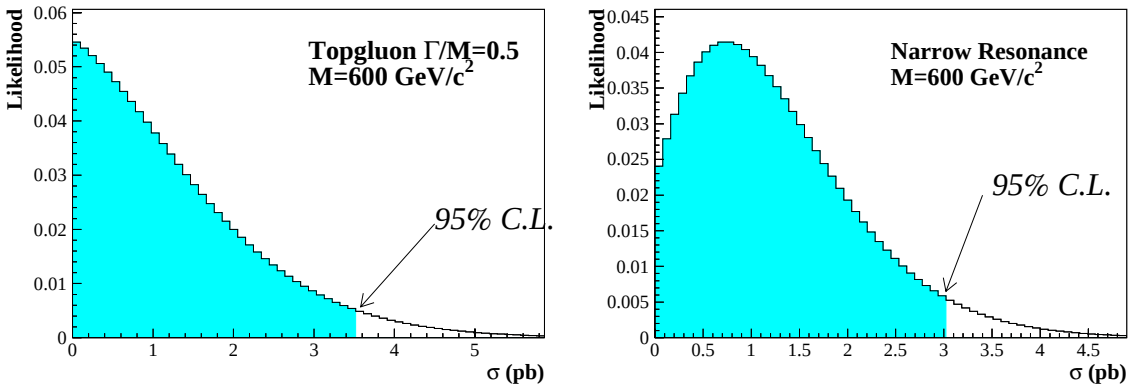

Figure 6.1

The likelihood functions for the resonance cross section for a 600 GeV/c^2 topgluon of fractional width , /M = 0.5 (left) and a 600 GeV/c^2 narrow resonance (right). The likelihood distribution for a narrow resonance is peaked at ≈ 1 pb while the likelihood for a topgluon resonance is peaked at zero.

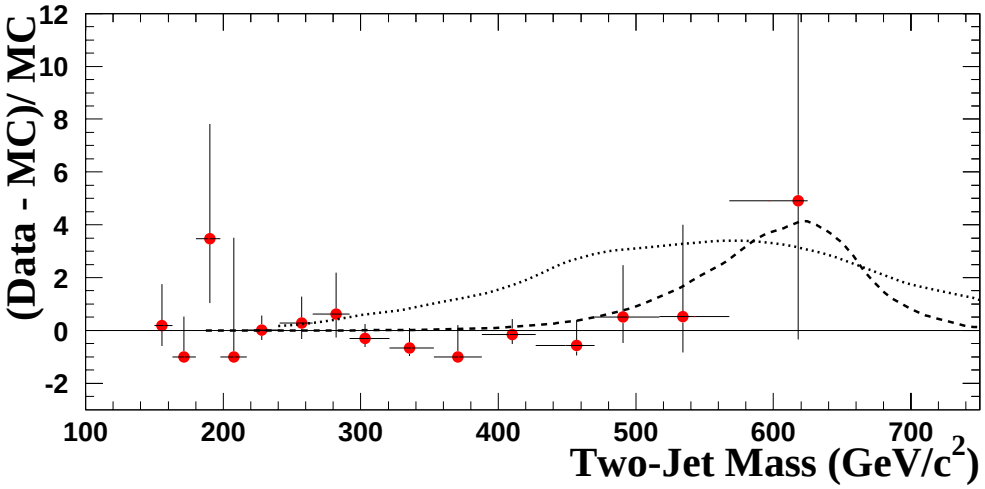

Figure 6.2

The fractional difference between the data and the fit compared to the shape of a narrow 600 GeV/c^2 new particle resonance (dashed line), and the shape of a 600 GeV/c^2 topgluon resonance of width , /M = 0.5 (dotted line).

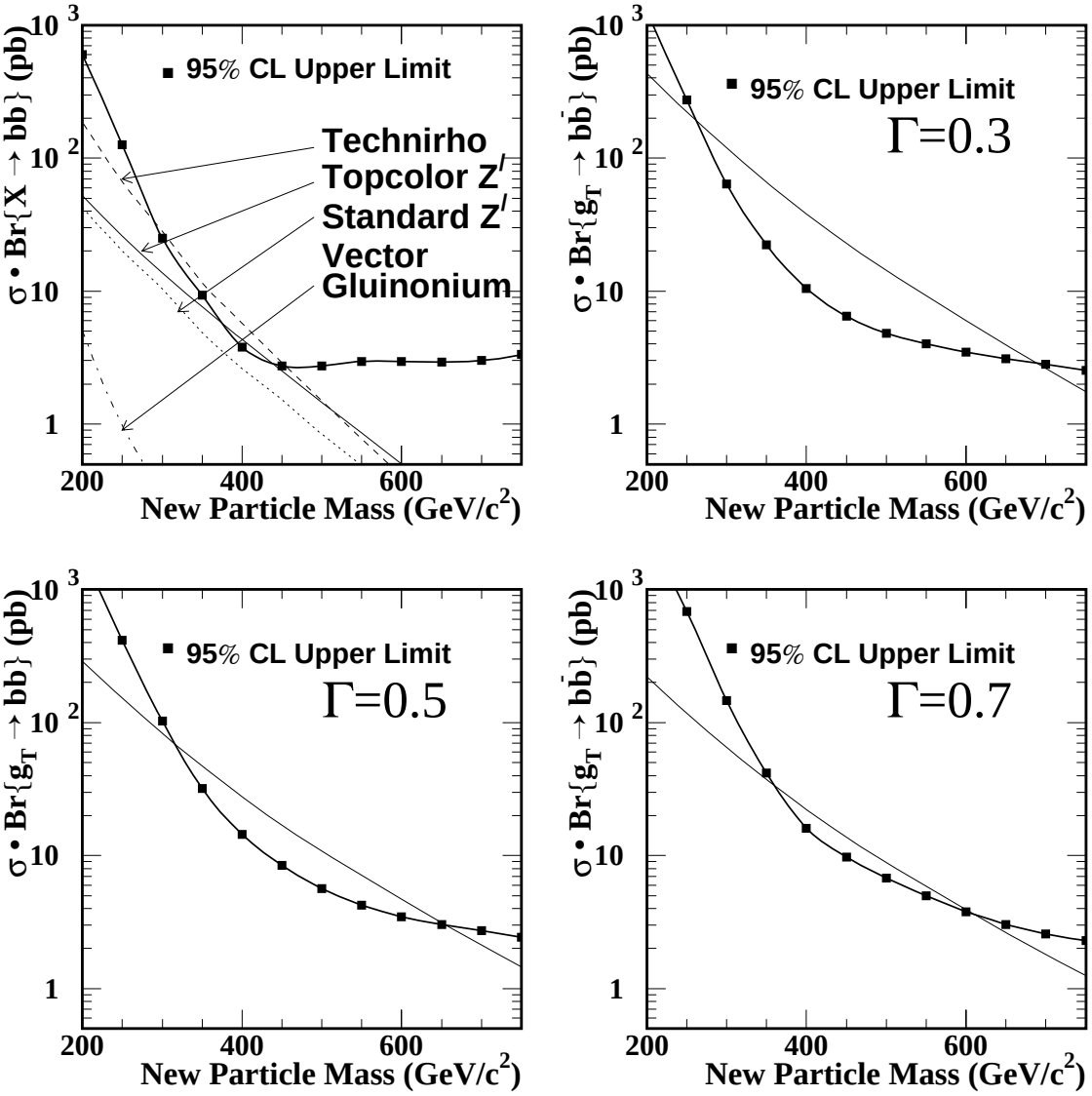

Figure 6.3

The 95% confidence level upper limits on new particle cross sections with statistical errors only. The curves show the theoretical predictions of the cross section times branching fraction to $b\overline{b}$ for our chosen kinematic cuts.

resonance can be fit to the distribution at that point, while the distribution for the topgluon resonance is peaked at 0. Figure 6.2 compares the $b\bar{b}$ mass distribution for the two resonances with the fractional difference between the data spectrum and the background fit. The spectrum is not consistent with a wide 600 GeV/c^2 resonance, while it will easily accommodate a small narrow resonance.

This process is repeated once for each new particle width and mass tested. We fit for a new particle resonance every 50 GeV/c^2 between 200 and 750 GeV/c^2. The cross section limits, as a function of new particle mass is shown for each simulated resonance width in Figure 6.3. Also plotted in the same figure are the theoretical cross section times branching fraction to $b\bar{b}$ for each particle sought. These limits include the effect of statistical uncertainties only. The sources of systematic uncertainty and a procedure for incorporating their effect into the limits are discussed below.

6.3 Systematics

The systematic uncertainties considered here can effect the result in two different ways: they can effect the shape of the mass distribution of either the background or a new particle resonance, or they that effect the overall rate. For those that effect the overall shape of the distribution, we apply the $\pm 1\sigma$ systematic directly to the data and recalculate the limit, since their effect may change the optimal value of the fit parameters. For those that effect the overall rate (such as the luminosity), the systematic is incorporated directly, without refitting. The sources of systematic uncertainty and the method for calculating their impact on the limit are described in detail below.

6.3.1 Sources of Systematic Uncertainty

6.3.1.1 Absolute Jet Energy Scale

Uncertainties in calorimeter response, jet fragmentation, underlying event, and the stability of the calorimeter each contribute to an overall uncertainty in the average measured jet E_T produced by jets of a particular true E_T. The fractional uncertainty in the absolute jet energy scale can be parameterized by:

$$1\sigma \text{ uncertainty} \approx \pm\sqrt{(0.02)^2 + \left(0.022 + \frac{0.6}{E_T}\right)^2} \tag{6.6}$$

for jets clustered with a cone size of 0.7 [65, 66]. The dominant contribution to the energy scale systematic comes from the uncertainty in the single pion response when convoluted with the jet fragmentation function [43].

6.3.1.2 Relative Jet Energy Scale

In addition to the uncertainty in the absolute jet energy scale, there is also an uncertainty associated with the calorimeter response and resolution as a function of detector η. The procedure for correcting for the variations in detector response as a function of detector η, discussed in Section 3.2, is to compare the calorimeter measurement of the two jets in dijet events that contain at least one central jet. Momentum conservation guarantees that the jets in a dijet should balance back-to-back in p_T, thus, dijet events can be used to determine the detector response as a function of detector η with respect to an equivalent central jet. While this correction compensated for variations in calorimeter response across the detector, it does not address the effects of energy resolution smearing.

To study what effect the resolution may have on the relative jet energy scale, QCD dijets were generated at parton level, then using a parameterized jet simulation that used a response map determined from the jet balancing procedure, the

generated partons were degraded, and the jets were then corrected using the default jet corrections described in Section 3.2. The jet balancing procedure was then applied to the simulated dijets in each of four calorimeter regions:

- the ninety degree crack ($|\eta_d| < 0.15$),
- the central calorimeter ($0.15 < |\eta_d| < 0.9$), which is taken as the standard,
- the thirty degree crack ($0.9 < |\eta_d| < 1.4$), at the joint between the central and the endplug calorimeters,
- and the endplug calorimeter ($|\eta_d| > 1.4$).

(see the cross sectional view of the calorimeters in Figure 2.3). A distribution was then made of fractional difference in the jet response between each of these regions and the central region of the calorimeter, and found to be approximately gaussian. The mean, μ, and standard deviation, σ, of the gaussian fit to the distribution for each detector region as a function of jet p_T were then compared. Tuning the simulation to match the resolution in the data resulted in an energy shift between the jets in the dijet, which is taken to be the systematic uncertainty, which is shown in Table 6.1.

	$\|\eta_d\| < 0.15$	$0.15 < \|\eta_d\| < 0.9$	$0.9 < \|\eta_d\| < 1.4$	$\|\eta_d\| > 1.4$
$M_{jj} < 517$ GeV/c^2	3%	2%	4%	2%
$M_{jj} > 517$ GeV/c^2	6%	2%	4%	2%

Table 6.1

The systematic uncertainty in the jet energy scale as a function of detector eta.

This systematic is applied to the data directly by changing the four momentum of each corrected jet up and down by the percentages shown. The limits are then

recalculated using the resulting spectrum. The systematic error in the limit is then taken to be the maximum deviation from the default limit.

6.3.1.3 Final State Radiation

In Figure 6.4 the dijet mass distributions for a simulated narrow resonance are shown superimposed on a gaussian fit to the high mass side of the distribution. When the fit is extrapolated to low mass, a large discrepancy between the distribution and the fit, the result of energy losses from radiation off the final state, is apparent. At the energies studied here, the emission of quarks and gluons from the final state can produce jets that are narrow enough to be clustered as distinct from the dijet. As the energy increases, so too does the importance of this phenomenon relative to fragmentation. This produces the observed tail on the gaussian dijet mass distribution at low mass which degrades the resolution.

The resolution could be improved by removing all events containing third jet with a p_T greater than 5% of the dijet invariant mass, as shown in Figure 6.5, however, such a requirement would severely reduce the efficiency. Since we do not place a cut to remove the tail, the uncertainty on the simulated shape of the resonance is included in the systematics by refitting for a particle resonance using the nearly gaussian resonance shapes in Figure 6.5, which include essentially no hard gluon radiation. The 1σ systematic is taken to be one half of the difference in the limits, since the scenario with no radiation corresponds to a nearly 2σ uncertainty.

6.3.1.4 Jet Energy Resolution

Another systematic in the shape of the resonance arises from a 1σ uncertainty of 10% in the RMS of the gaussian dijet mass resolution [67]. To study the effect

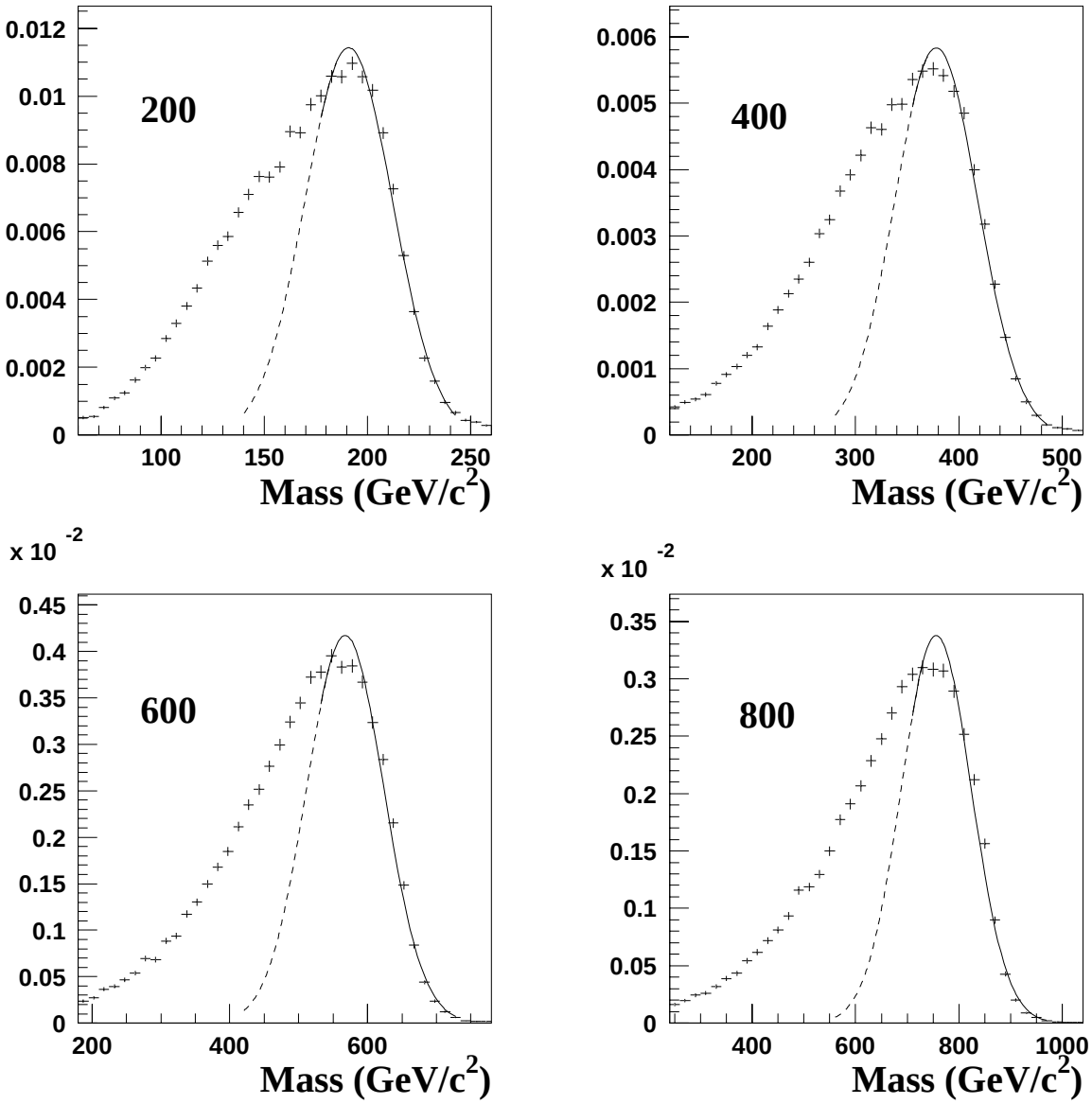

Figure 6.4

The dijet invariant mass distributions for 200, 400, 600, and 800 GeV/c^2 $Z' \to b\overline{b}$ as simulated in the detector using PYTHIA + QFL. A gaussian is used to fit the high mass side of the distribution (solid line), and the fit is extrapolated to low mass (dashed line). The difference between the distribution and the fit at low mass is the result of losses from initial and final state radiation.

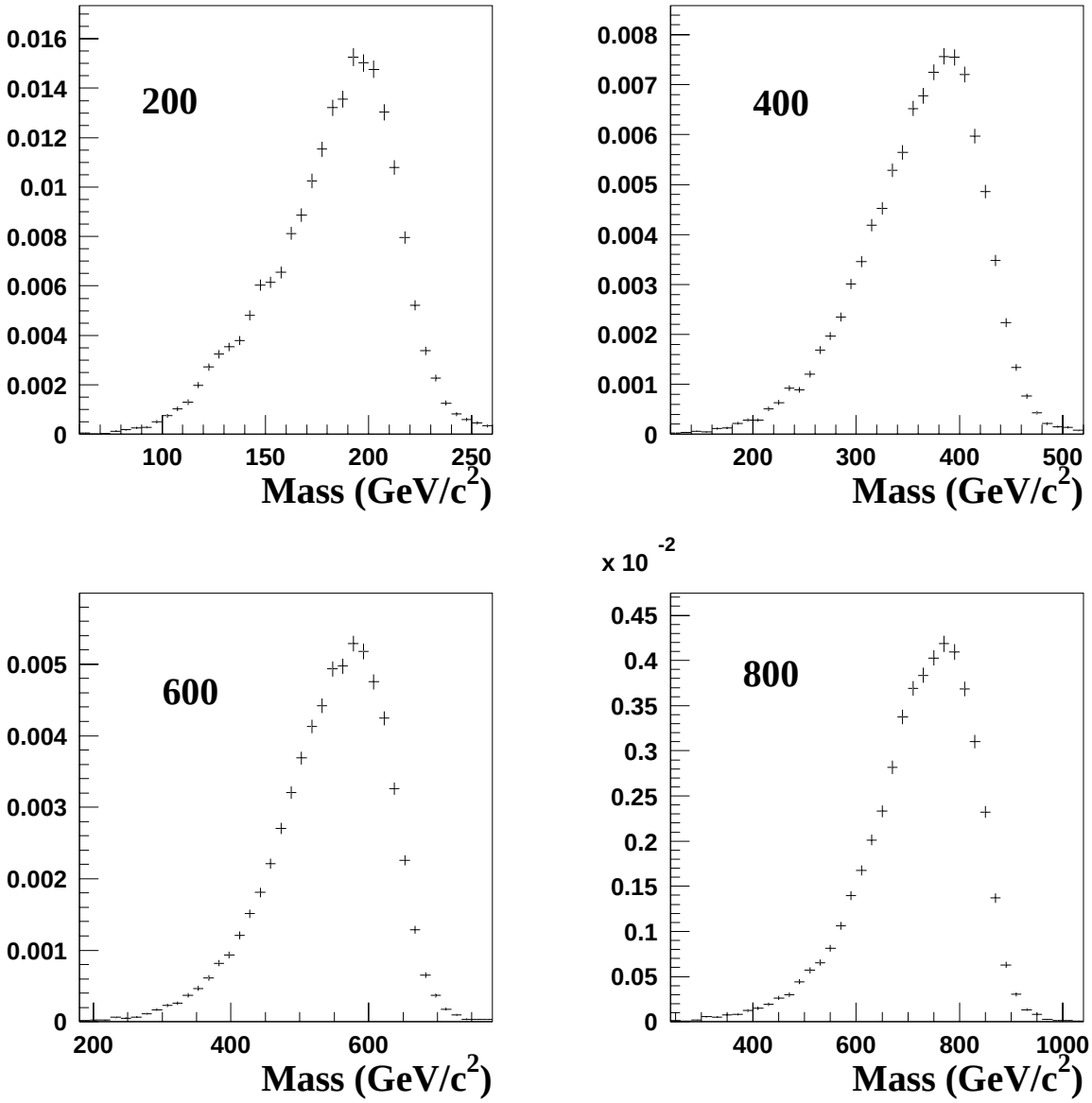

Figure 6.5

The dijet mass distributions for 200, 400, 600, and 800 GeV/c^2 $Z' \to b\overline{b}$ as simulated in the detector with no third jet with a transverse momentum greater than 5 % of the dijet invariant mass.

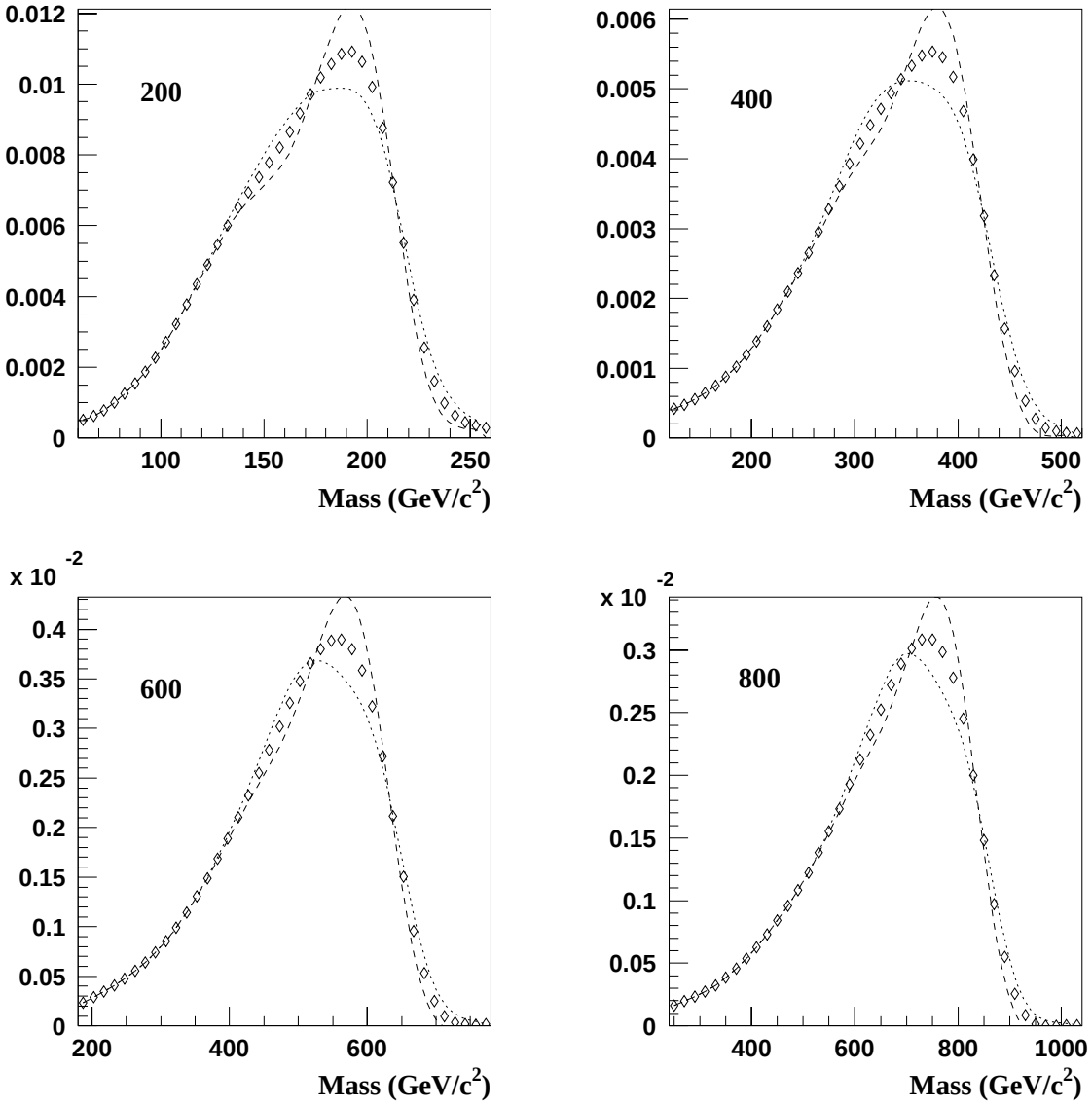

Figure 6.6

The dijet mass distributions for 200, 400, 600, and 800 GeV/c^2 $Z' \rightarrow b\overline{b}$ after detector smearing (diamonds). The dashed (dotted) line shows the resonance shape with the gaussian RMS reduced (increased) by 10 %.

of this systematic on the shape of a mass resonance, we take the gaussian fits from Figure 6.4 and vary the width, σ, by 10% while holding the mean mass, μ_m, and the normalization, A, constant.

$$G_{sys}(m, \mu_m, \sigma) = A \exp\left[-\frac{1}{2}\left(\frac{m-\mu_m}{\sigma \pm 0.1\sigma}\right)^2\right] \tag{6.7}$$

The resulting curves are then normalized to the same integrated area as the original gaussian, and the radiated tail is added to get the variation in the shape of the resonance as shown in Figure 6.6, where the diamonds show the original distribution and the dashed (dotted) line shows the shape with σ decreased (increased) by 10%.

For each of the systematics in the shape of the resonance (the radiated tail and the gaussian shape), the systematic uncertainty in the limits are determined by recalculating the fit of the spectrum to a resonance superimposed on the background using the procedure outlined in Section 6.2 while substituting the line shapes in Figures 6.6 and 6.5 to parameterize the shape of the resonance.

This systematic is only considered for narrow resonances because topgluons would produce a resonance much wider than the mass resolution of the detector.

6.3.1.5 Background Parameterization

We have investigated two sources of uncertainty in our simulation of the shape of the $b\bar{b}$ spectrum; the renormalization scale, and the parton distribution functions. The default value of the renormalization scale used in this analysis is the mass of the system, $\mu = m$. We have raised this value to $\mu = 2m$ and lowered it to $\mu = m/2$, and although this resulted in a significant change in the overall normalization of the spectrum, the resulting change in the shape was found to be only 1%. The default parton distribution functions used in this analysis is CTEQ2L. Since the simulations for this analysis were generated, the parton distribution functions used here have

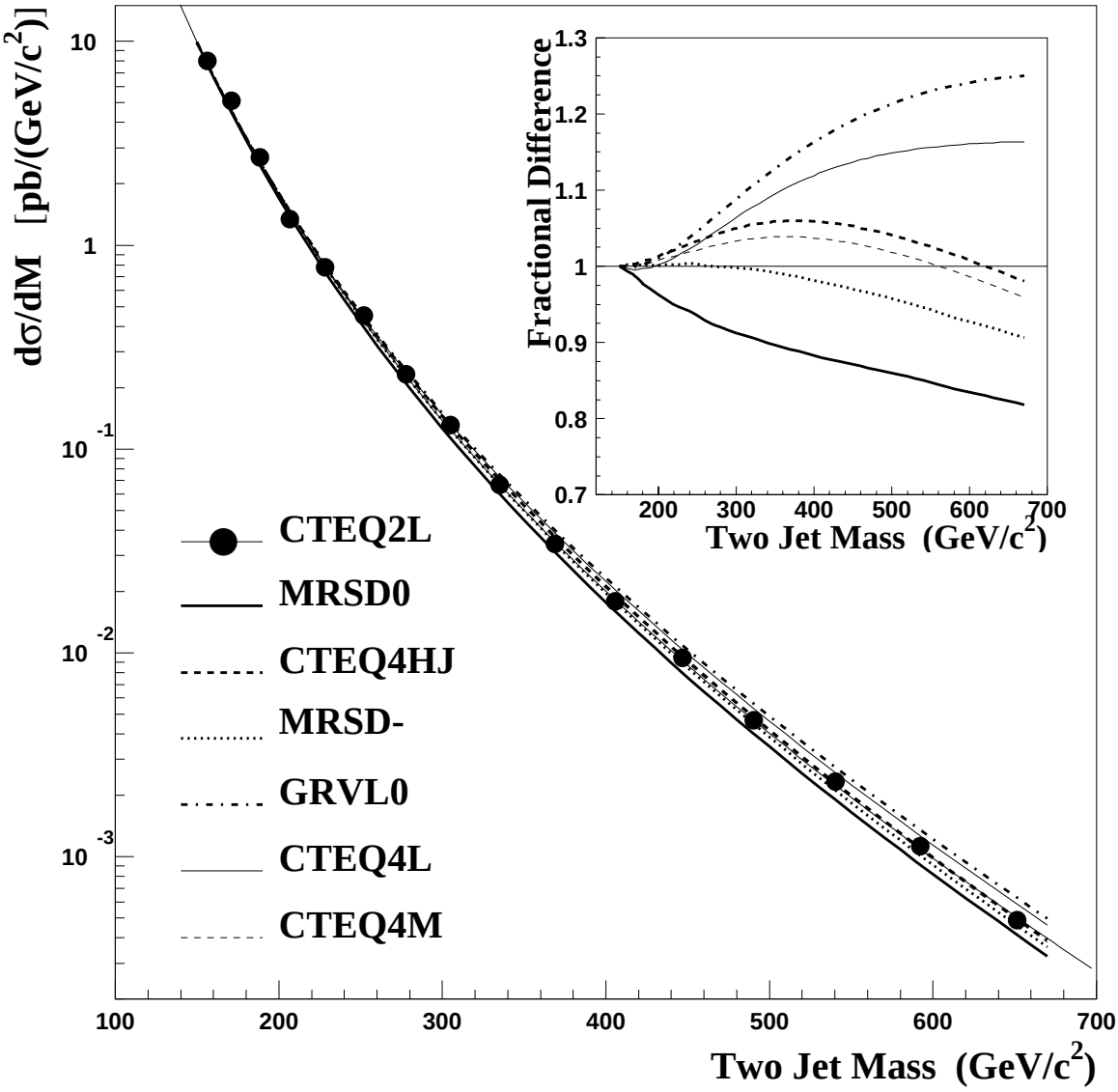

Figure 6.7

The shape dependence of the mass spectrum of directly produced $b\bar{b}$ pairs on the parton distribution functions. CTEQ2L is used as the default. The inset shows the fractional difference between the spectrum generated with CTEQ2L versus other pdf's.

been revised to agree with new experimental measurements which have recently become available. In addition, we compare the distribution given by CTEQ sets to those given by pdf sets from other collaborations. A brief discussion of parton distribution functions and the particular sets considered here is included in Appendix C. Figure 6.7 shows a comparison of the shape of the distributions generated using different parton distribution functions. When normalized to CTEQ2L at 150 GeV/c^2, they give a maximum deviation of +24% (GRVLO) and -16% (MRSD0) at 600 GeV/c^2. We therefore neglect the renormalization scale since the variation in the parton distribution functions is our dominant systematic on the shape of the spectrum.

The limits were recalculated using shape of the spectra given by GRVLO and MRSD0 which gave the maximum deviation from the default. At each new particle mass, the maximum deviation from the default limit was taken as the systematic.

6.3.1.6 Trigger Efficiency

The uncertainty in the calculation of the trigger efficiency discussed in Section 3.3 is simply given by the statistical uncertainty in each mass bin in Figure 3.2. The maximum statistical uncertainty in the trigger efficiency is $\approx$ 2% in the turn on region. We therefore conservatively take this systematic uncertainty as 2% everywhere. The impact on the limit is investigated by refitting the spectrum with the trigger efficiency set higher and lower by 2% .

6.3.1.7 *b*-tagging Efficiency

Uncertainties in the *b*-tagging efficiency could come from a number of sources including:

- the uncertainty in the b lifetime
- the uncertainty in the resolution of the silicon vertex detector
- the uncertainty in the b-fragmentation properties and the B-decay
- the uncertainty in the tracking efficiency

The first the three sources of uncertainty in the b-tagging efficiency were studied and found to be negligible [58]. Changing the b lifetime by $\pm 10\%$ resulted in only a 1% change in the tagging efficiency, while Monte Carlo studies of the b-fragmentation and B decay were used to estimate that these sources again contributed about a 1% change in the b-tagging efficiency. The distributions of the impact parameter, σ_d, and the impact parameter significance, $\frac{d}{\sigma_d}$, (see Chapter 4) were found to agree between data and the detector simulation to better than 5%. A 5% uncertainty in the resolution translates to only $\approx 1\%$ in the b-tagging efficiency.

The largest source of uncertainty in the b-tagging efficiency arises from the uncertainty in the tracking efficiency. A comparison of the track multiplicity in b-jet candidates in the inclusive electron data (which is enriched with b-jets from semileptonic b-decays, as explained in Section 4.2) with a $b\bar{b}$ Monte Carlo sample generated with the tracking degradation code described in Section 4.3 found a disagreement of ± 0.07 in the track multiplicity in the two samples [59]. We translate the 7% uncertainty in the tracking efficiency into the corresponding systematic on the b-tagging efficiency by rerunning SECVTX on Monte Carlo events with the probability for finding a track with a particular value of Q set 7% higher or lower and recalculating the b-tagging efficiency, therefore calculating a mass dependent estimate of the uncertainty in the b-tagging efficiency. The default b-tagging efficiency and its systematic errors are shown in Figure 6.8.

This uncertainty is incorporated into the limit by recalculating the limits with the b-tagging efficiency set at it's higher and lower bounds and taking the percent

maximum deviation from the default limit.

6.3.1.8 Luminosity

The luminosity at CDF is monitored by two sets of 16 scintillators, "beam-beam counters", arranged around the beampipe with one set upstream and one set downstream from the interaction region [31]. The coincidence rate of the two sets of counters, where only one scintillator on each side is required to fire within a 15 ns window centered on the beam crossing time, is proportional to the luminosity, however, the beam-beam counters saturate above a Tevatron luminosity of about $5 \times 10^{30}\text{cm}^{-2}\text{s}^{-1}$, necessitating a correction to the luminosity of the beam-beam counters to account for multiple interactions. Cross checks have shown this correction to be low, resulting in a Run IB integrated luminosity value that is 3-8% lower than the actual value. The uncertainty in luminosity for Run IB is therefore conservatively estimated to be 8% [68].

The uncertainty in the luminosity will not change the shape of the distribution, but will instead effect the overall rate. The number of events contributed to the spectrum by background ($N_{bb} = \mathcal{L}\sigma_{bb}$) and the number of events contributed by new particles ($N_{np} = \mathcal{L}\sigma_{np}$) are both linear functions of the luminosity. Therefore, to incorporate the uncertainty in the luminosity, we add include a constant factor of 8%, and do not refit the spectrum.

6.3.2 Total Systematic Uncertainty

The systematic uncertainties are expressed as the percent change in the 95% confidence level upper limit as a function of new particle mass as shown in Figure 6.9 for narrow resonances and in Figure 6.10 for topgluon resonances. The dominant

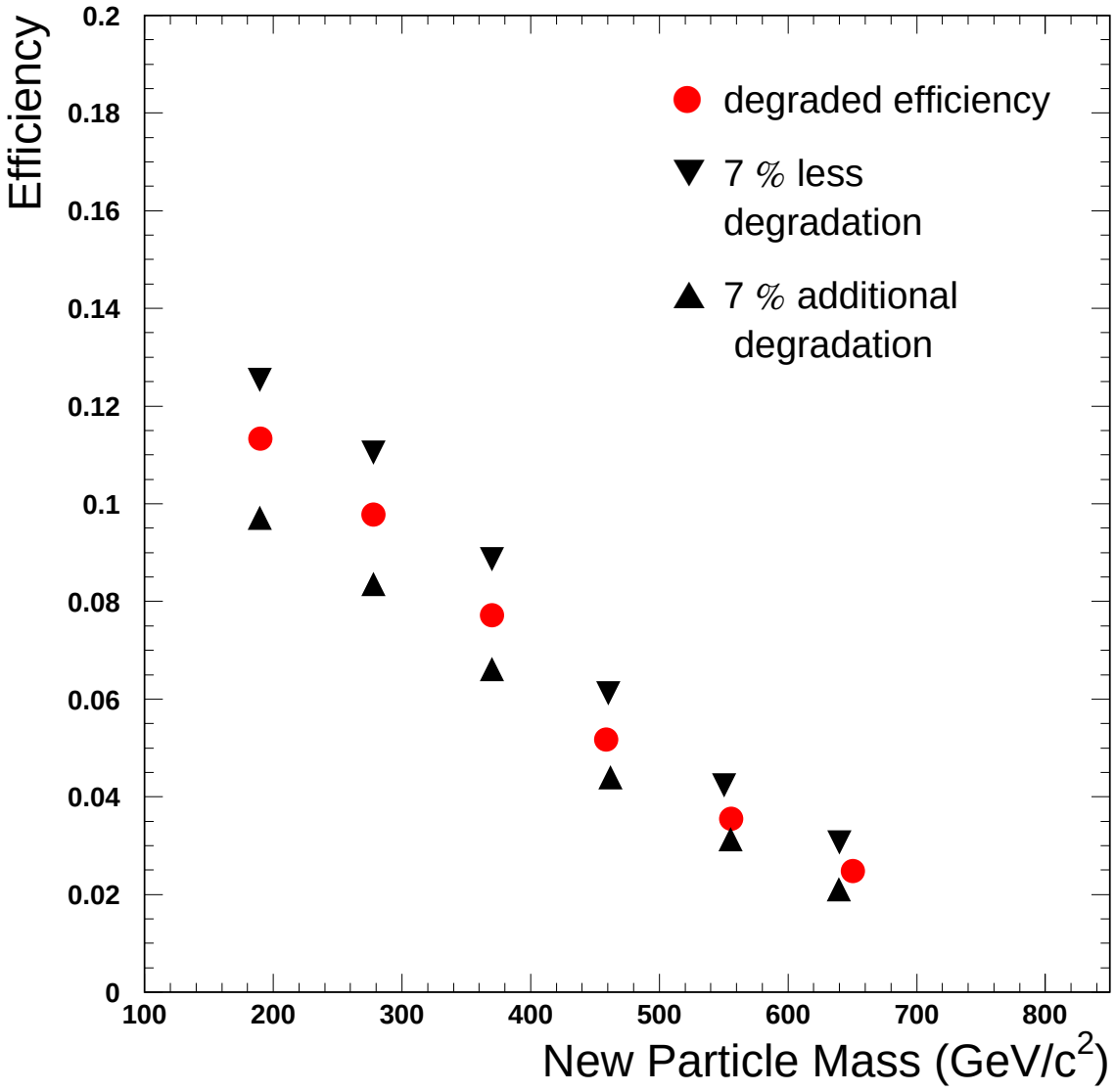

Figure 6.8

The triangles show the upper and lower errors on the double b-tagging efficiency obtained by running SECVTX on Monte Carlo events with the tracking efficiency set 7% higher than the default tracking efficiency, and with the tracking efficiency set 7% lower. The b-tagging efficiency calculated with the default tracking efficiency is shown by the circles.

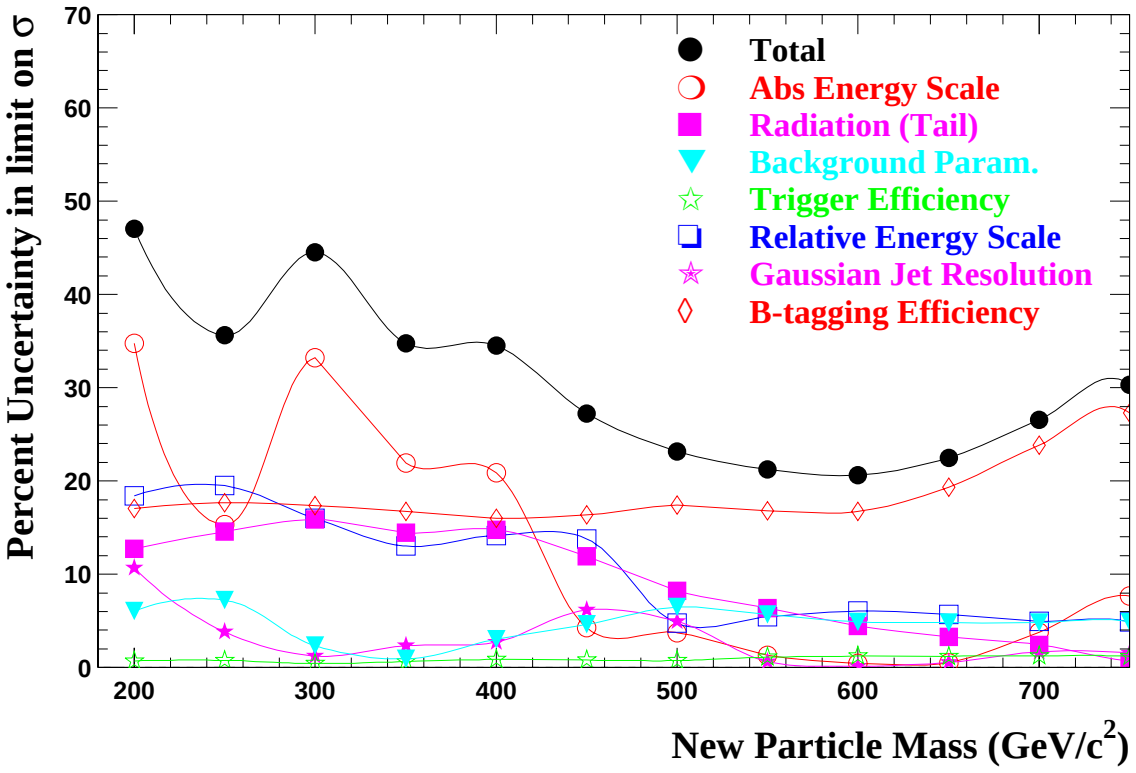

Figure 6.9

Systematic uncertainties on narrow resonances. The total systematic uncertainty is shown by the solid circles.

source of systematic uncertainty at low mass is the absolute energy scale, while the dominant source of systematic uncertainty at high mass is the b-tagging efficiency. The individual sources of systematic uncertainty are added in quadrature to obtain the total systematic uncertainty in the cross section limits, $\Delta\alpha$, which is shown by the solid circles in Figures 6.9 and 6.10. The total systematic uncertainty varies between 20 and 50%.

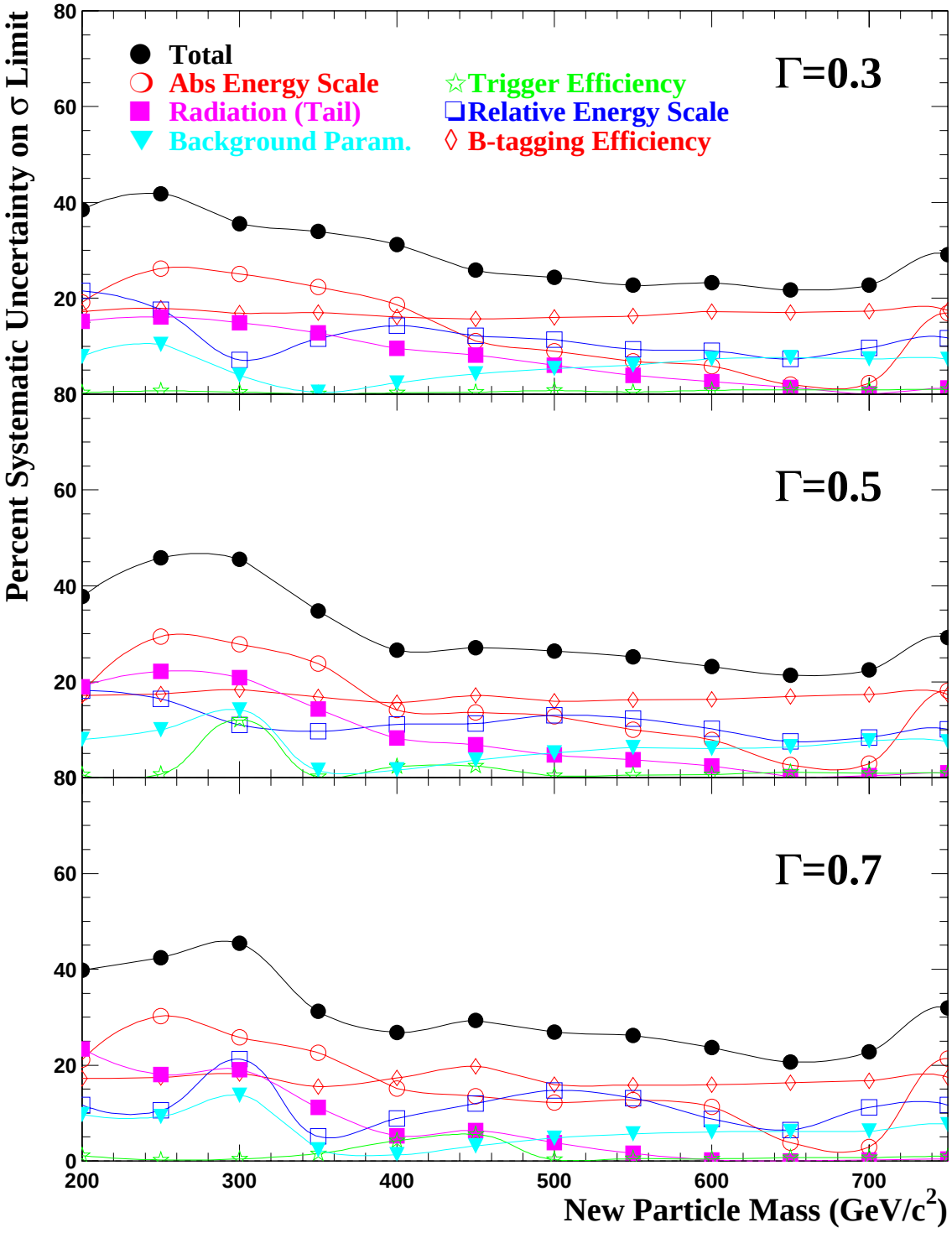

Figure 6.10

Systematic uncertainties on topgluon resonances. The total systematic uncertainty is shown by the solid circles.

6.3.3 Convolution of Limits with Systematics

In order to incorporate the systematic uncertainties into the limits, we smear the likelihood functions, such as the ones shown in Figure 6.1 with a gaussian with standard deviation of $\sigma = \Delta\alpha$:

$$L(\alpha) = \int_0^\infty L(\alpha')\, G(\alpha - \alpha', \Delta\alpha)\, d\alpha' \tag{6.8}$$

A comparison of the likelihood distributions before and after smearing is shown in Figures 6.11- 6.14. The 95% confidence level with systematics is again taken to be that value of α for which 95% of the area under the likelihood function is between 0 and α, only now we calculate this value by integrating the smeared likelihood function.

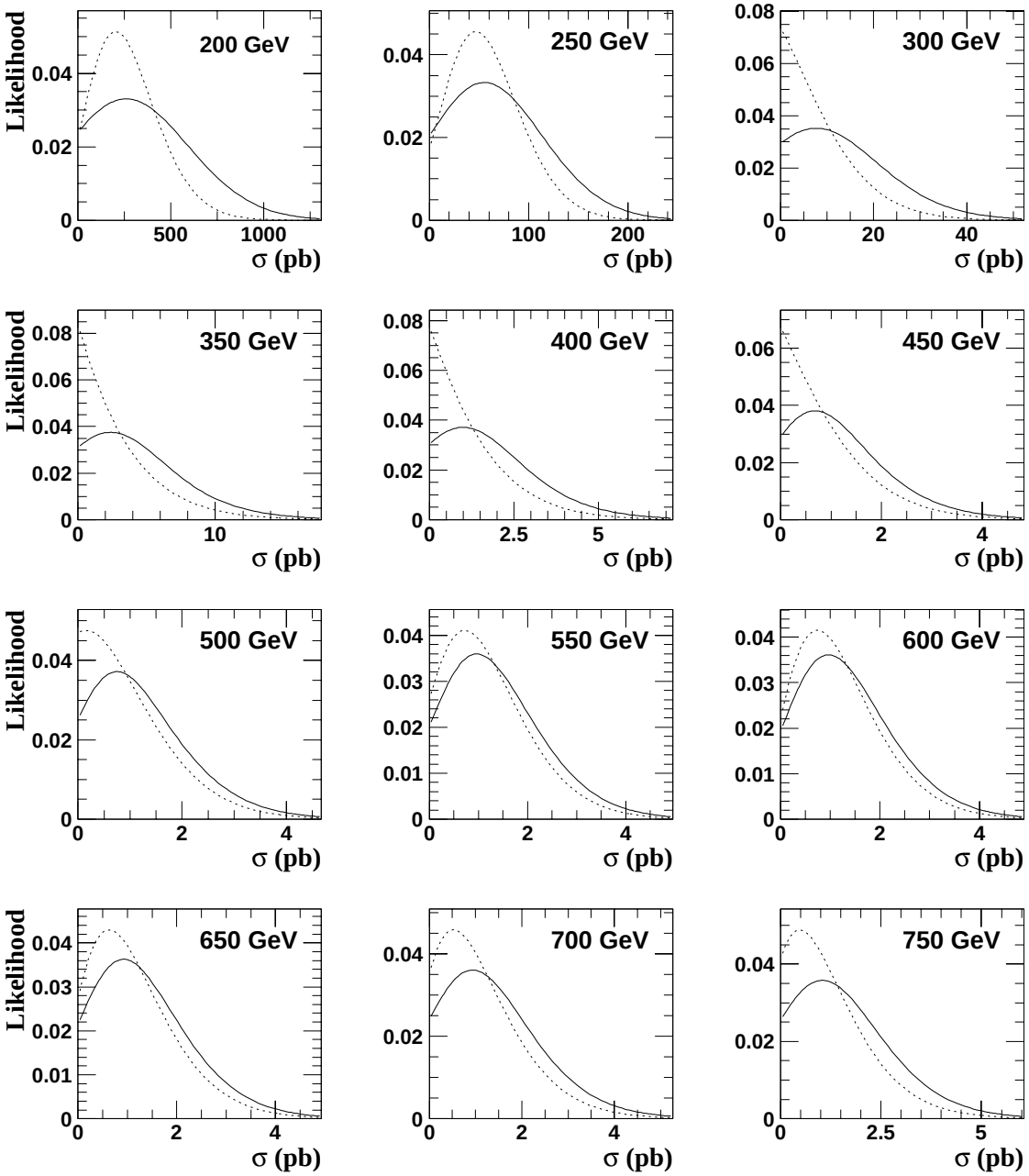

Figure 6.11

The likelihood function for a narrow resonance is shown with statistical uncertainties only (dotted lines) and with the gaussian convoluted with the systematic uncertainties (solid lines).

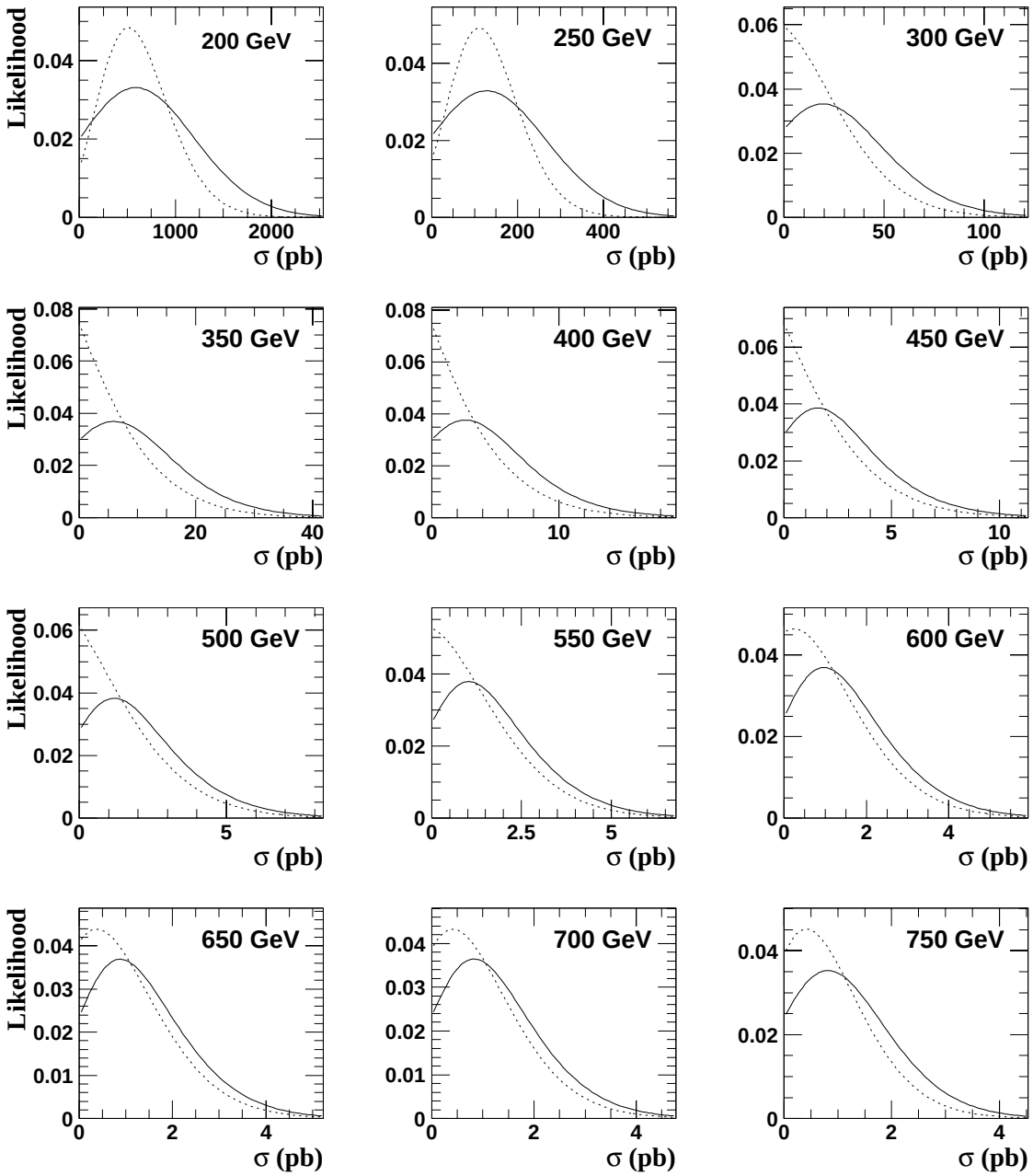

Figure 6.12

The likelihood function for a topgluon resonance of width , /M = 0.3 is shown with statistical uncertainties only (dotted lines) and with the gaussian convoluted with the systematic uncertainties (solid lines).

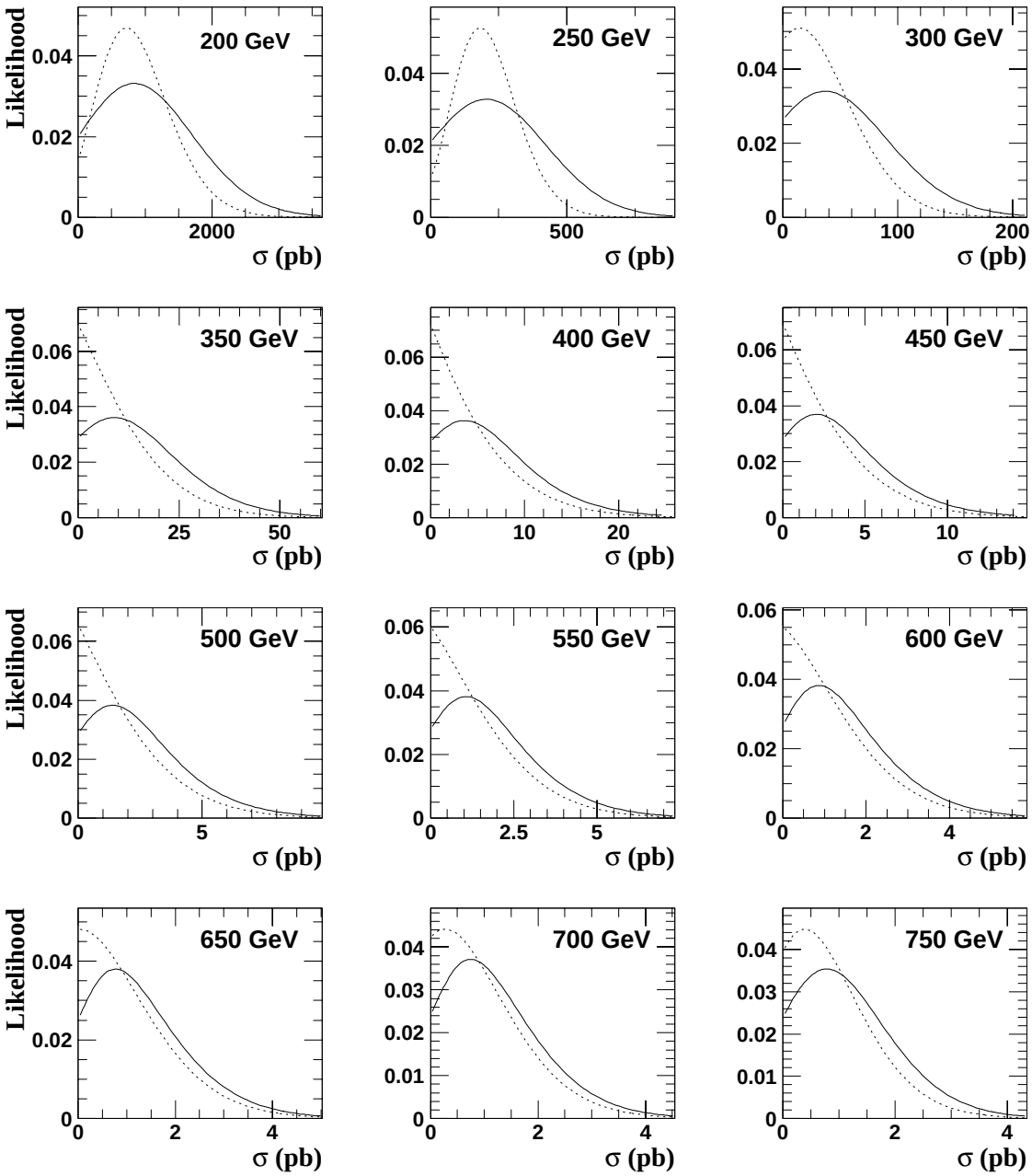

Figure 6.13

The likelihood function for a topgluon resonance of width , /M = 0.5 is shown with statistical uncertainties only (dotted lines) and with the gaussian convoluted with the systematic uncertainties (solid lines).

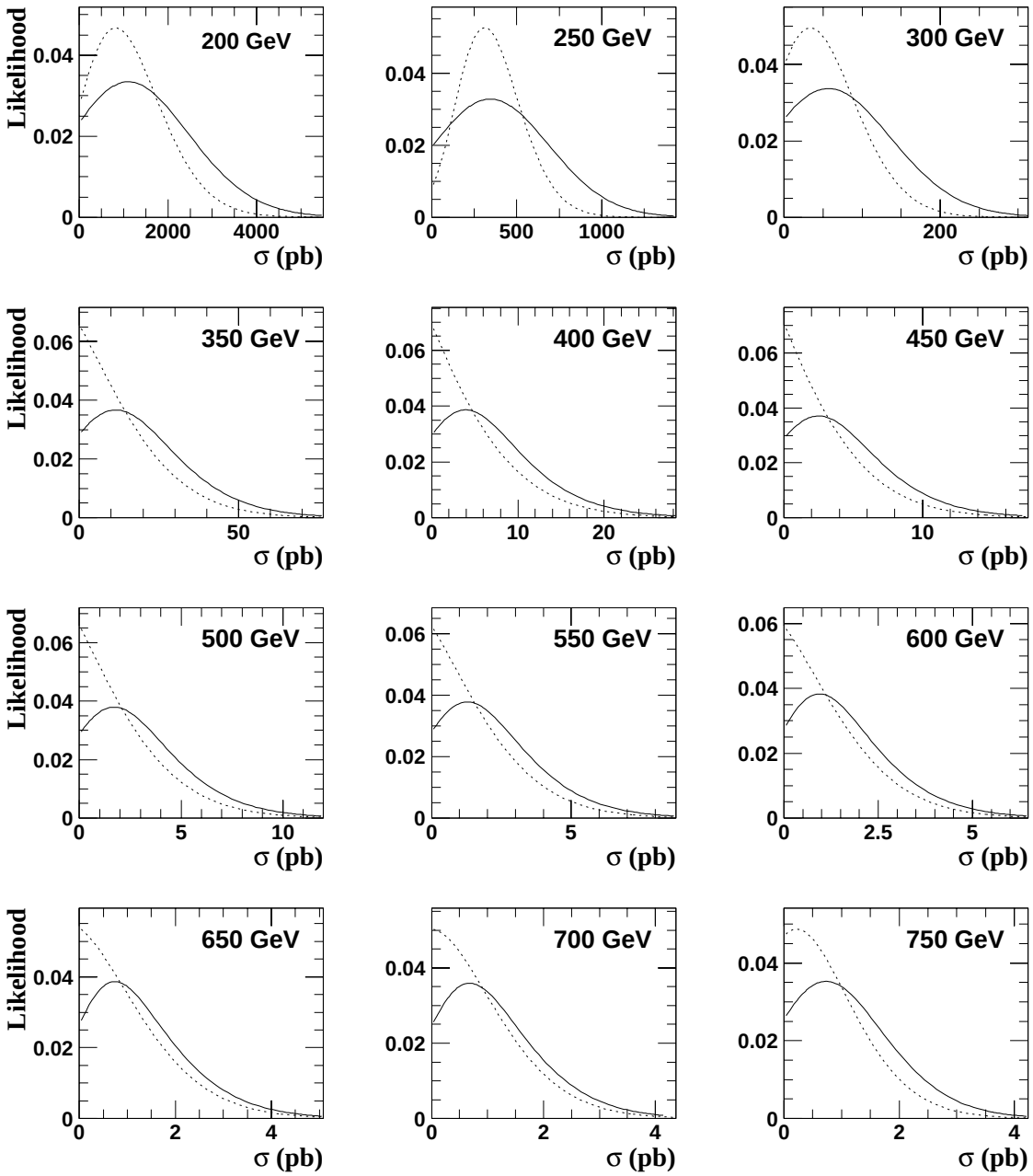

Figure 6.14

The likelihood function for a topgluon resonance of width , /M = 0.7 is shown with statistical uncertainties only (dotted lines) and with the gaussian convoluted with the systematic uncertainties (solid lines).

6.4 Results

The 95% confidence level upper limits on the cross section of a new particle resonance including the effects of systematic uncertainties are shown in Figure 6.15. The limits without systematics are shown in the same figure to illustrate their impact. The cross section upper limits for narrow resonances exclude the color-octet technirho between 350 and 440 GeV/c^2. The limits for narrow resonances, however, are completely general, and can be compared to the cross section times branching fraction for any new particle with a width narrower than the dijet mass distribution.

The exclusion region for topgluons is dependent on the fractional width as well as the mass. We exclude topgluon in the mass regions:

$$, /M = .3 \quad 280 < M < 670 \text{ GeV}/c^2$$

$$, /M = .5 \quad 340 < M < 640 \text{ GeV}/c^2$$

$$, /M = .7 \quad 375 < M < 560 \text{ GeV}/c^2$$

These are the first limits from a direct search for Topcolor.

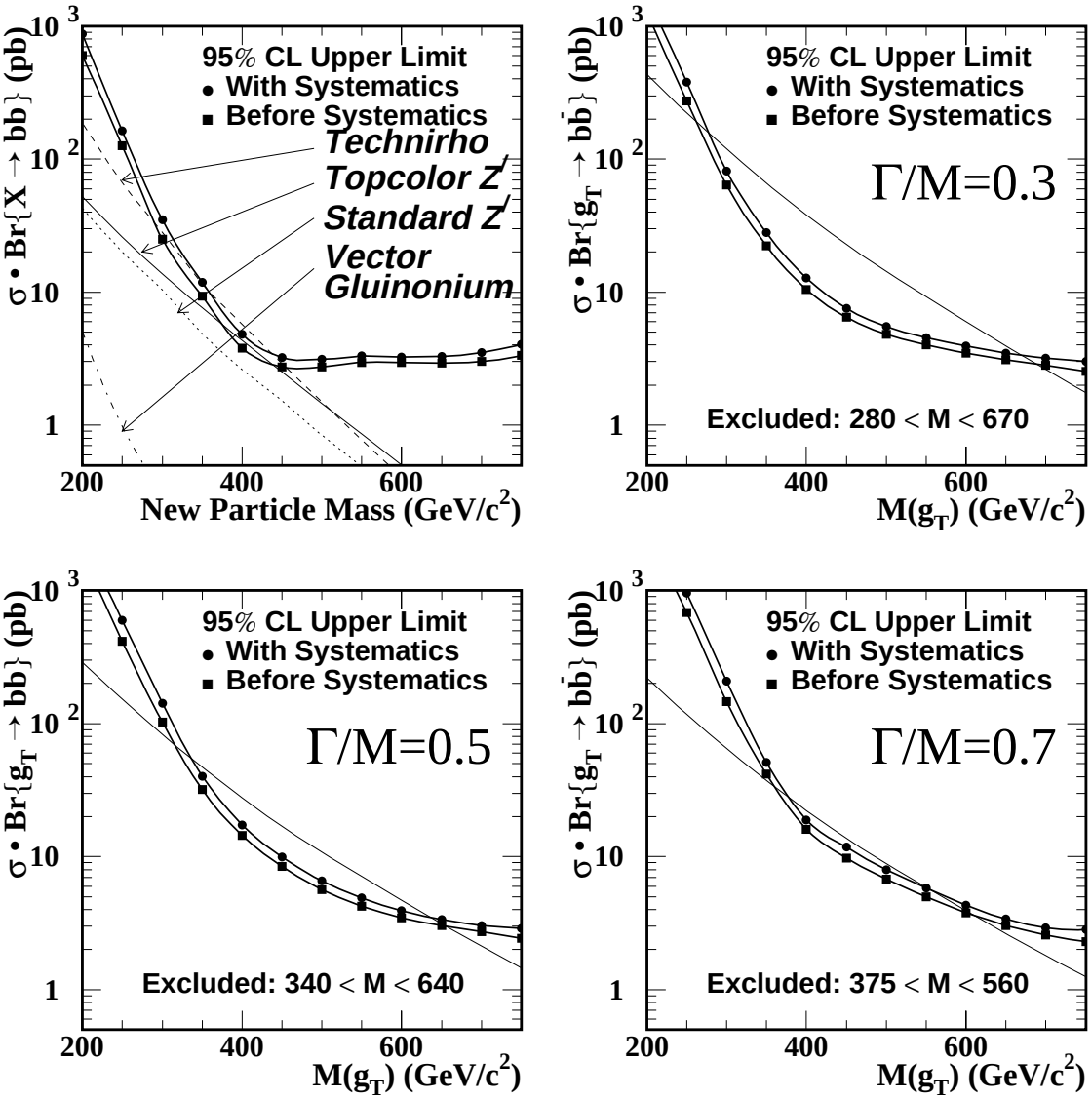

Figure 6.15

The 95% confidence level upper limits on new particle cross sections with systematic errors (circles). Also shown are limits with statistical errors only (squares). The lines show the theoretical predictions of the cross section times branching fraction to $b\overline{b}$ for our chosen kinematic cuts.

7. CONCLUSION

We have reconstructed the $b\bar{b}$ mass distribution from 87 pb^{-1} collected at the Fermilab Tevatron and it is found to be a smoothly falling spectrum that is in good agreement with simulations of direct $b\bar{b}$ production. Using these results we exclude topgluons, a new massive color octet boson from models of Topcolor, which invokes a $t\bar{t}$ condensate to generate the large mass of the top quark, in the mass and width ranges:

$$, \; /M = .3 \quad 280 < M < 670 \text{ GeV}/c^2$$

$$, \; /M = .5 \quad 340 < M < 640 \text{ GeV}/c^2$$

$$, \; /M = .7 \quad 375 < M < 560 \text{ GeV}/c^2$$

The exclusion region for topgluons in the mass-width plane is shown in Figure 7.1. These are the first direct limits from a Topcolor model. An analysis of the $t\bar{t}$ mass distribution for evidence of Topcolor is currently underway. We also set cross section upper limits on narrow resonances which exclude the color octet technirho from a model of walking Technicolor in the mass region from $350 < M < 440$ GeV/c^2. Furthermore, the cross section limits on narrow resonances are applicable to any particle with a width narrower than the $b\bar{b}$ resolution of the CDF detector.

The Tevatron will remain the world's highest energy accelerator until the Large Hadron Collider comes online in the next decade. Preparations are underway for a high luminosity run of the Tevatron, to commence in 1999, that is expected to collect 2 fb^{-1} of data at an increased center-of-mass energy of 2 TeV, while upgrades of the Collider Detector's tracking system are expected to increase the double b-tagging

efficiency by a factor of two. As we continue to scan energies near the electroweak scale, it is hoped that a clearer picture of the mechanisms responsible for electroweak symmetry breaking, and the large mass of the top quark will emerge.

	Narrow	**Topgluons**		
Mass	, $/M < 0.1$	, $/M = 0.3$	, $/M = 0.5$	, $/M = 0.7$
(GeV)	σ limit (pb)	σ limit (pb)	σ limit (pb)	σ limit (pb)
200	8.7×10^2	1.7×10^3	2.4×10^3	3.7×10^3
250	1.6×10^2	3.8×10^2	6.0×10^2	9.6×10^2
300	3.5×10^1	8.1×10^1	1.4×10^2	2.1×10^2
350	1.2×10^1	2.8×10^1	4.0×10^1	5.1×10^1
400	4.8	1.3×10^1	1.7×10^1	1.9×10^1
450	3.2	7.6	9.9	1.2×10^1
500	3.1	5.5	6.6	8.0
550	3.3	4.5	4.9	5.8
600	3.3	4.0	3.9	4.3
650	3.3	3.5	3.4	3.4
700	3.5	3.2	3.0	2.9
750	4.0	3.0	2.9	2.8

Table 7.1

The 95% CL upper limit on the cross section for new particles decaying to $b\bar{b}$ as a function of new particle mass for narrow resonances and for topgluons of three different widths.

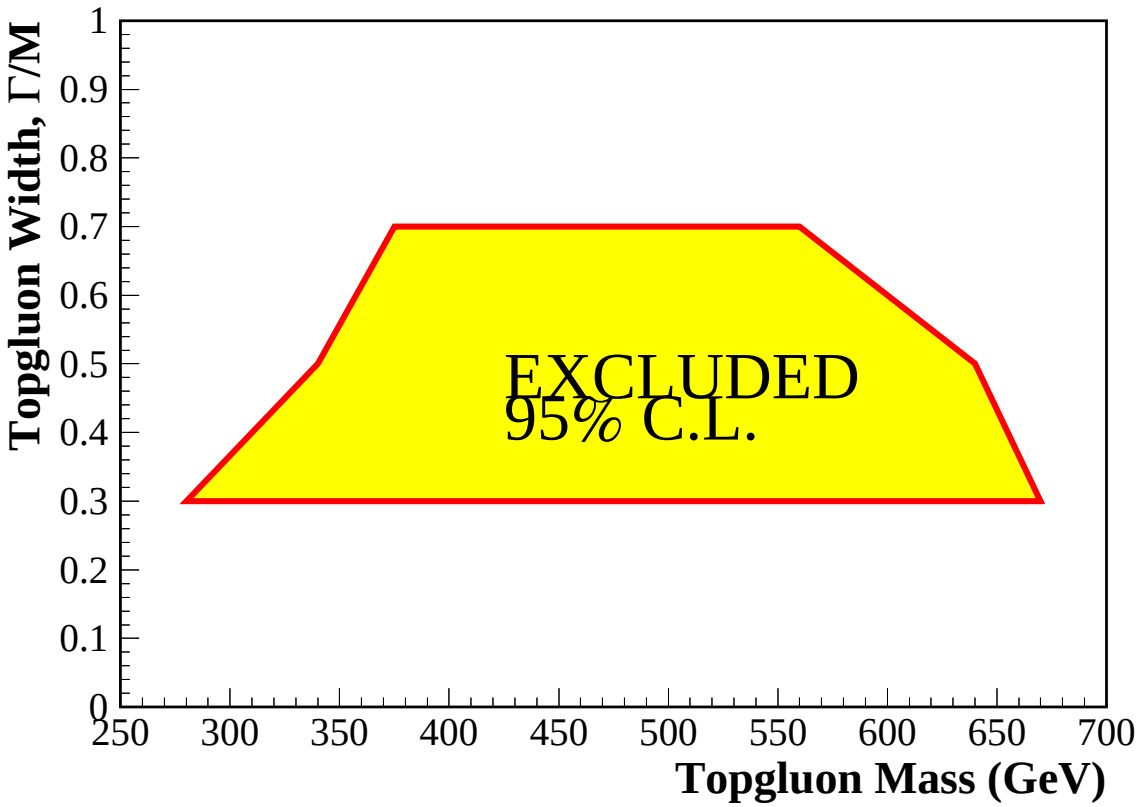

Figure 7.1

The excluded region for topgluons in the mass-width plane.

BIBLIOGRAPHY

BIBLIOGRAPHY

1. E. Eichten and K. Lane. Multiscale Technicolor and Top Production. *Phys. Lett. B*, **327**:129, 1994.

2. Discussed in numerous texts on particle physics and field theory, see for example; F. Halzen and A. Martin, *Quarks & Leptons: An Introductory Course in Modern Particle Physics*, John Wiley & Sons, 1984 ; T. Cheng and L. Li, *Gauge Theory of Elementary Particle Physics*, Oxford University Press, 1984.

3. F. Abe et al. Observation of Top Quark Production in $\overline{p}p$ Collisons with the Collider Detector at Fermilab. *Phys. Rev. Lett.*, **74**:2626, 1995.

4. F. Abachi et al. Observation of the Top Quark. *Phys. Rev. Lett.*, **74**:2632, 1995.

5. L3 ALEPH, DELPHI and OPAL Collaborations. Lower bound for the Standard Model Higgs Boson Mass from combining the results of the four LEP experiments. CERN preprint cern/ep-98-053, 1998.

6. C. Quigg. Supercollider physics. Invited talk at 8th Les Rencontres de Physique de la Vallee d'Aoste: Results and Perspectives in Particle Physics, La Thuile, Italy, 1994.

7. S. Dawson. SUSY and such. Lectures given at NATO Advanced Study Institute on Techniques and Concepts of High-energy Physics, St. Croix, U.S. Virgin Islands, 1996.

8. H. E. Haber and G. L. Kane. The Search for Supersymmetry: Probing Physics Beyond the Standard Model. *Phys. Rep.*, **117**:75, 1985.

9. Physical Review D, Particles and Fields, Review of Particle Properties, Volume 54, 1 July 1996, page 562.

10. E. Chikovani V. Kartvelishvili R. Shanidze and G. Shaw. Bound states of two gluinos at the Fermilab Tevatron and CERN LHC. *Phys. Rev. D*, **53**:6653, 1996.

11. F. Abe et al. Search for Gluinos and Squarks at the Fermilab Tevatron Collider.

Phys. Rev. D, **79**:1357, 1997.

12. K. Lane. An Introduction to Technicolor. Boulder 1993, Proceedings, *The building blocks of creation*, 1993.

13. L. Susskind. The Gauge Hierarchy Problem, Technicolor, Supersymmetry, and all that. *Phys. Rep.*, **104**:181, 1984.

14. S.F. King. Dynamical Electroweak Symmetry Breaking. *Rep. Prog. Phys.*, **58**:263, 1995.

15. E. Eichten et al. Super Collider Physics. *Rev. Mod. Phys.*, **56**:655, 1984.

16. Kenneth Lane. Technicolor. hep-ph/9501249, 1994.

17. K. Lane and R. V. Ramana. Walking Technicolor Signatures at Hadron Colliders. *Phys. Rev. D*, **44**:2678, 1991.

18. F. Abe et al. Search for New Particles Decaying to Dijets at CDF. *Phys. Rev. D*, **55**:5263, 1997.

19. T. Handa et. al. Search for Technicolor Particles in W+2jet with b-tag Channel at CDF. Published Proceedings Workshop on Physics at the First Muon Collider and at the Front End of a Muon Collider, Fermi National Accelerator Laboratory, Batavia, IL, 1997.

20. F. Abachi et al. Measurement of the Top Quark Mass. *Phys. Rev. Lett.*, **80**:2767, 1998.

21. C. T. Hill. Topcolor Assisted Technicolor. *Phys. Lett. B*, **345**:483, 1995.

22. E. Eichten and K. Lane. Electroweak and flavor dynamics at hadron colliders. published in Snowmass 1996, New Directions for High Energy Physics, Proceedings of the 1996 DPF/DPF Summer Study on High Energy Physics, 1996.

23. F. Abe et al. Search for new gauge bosons decaying into dileptons in $p\overline{p}$ collisions at $\sqrt{s} = 1.8$ TeV. *Phys. Rev. Lett.*, **79**:2192, 1997.

24. F. Abe et al. Measurement of dijet angular distributions at cdf. *Phys. Rev. Lett.*, **77**:5336, 1996.

25. F. Abe et al. Inclusive jet cross-section in $p\overline{p}$ collisions at $\sqrt{s} = 1.8$ TeV. *Phys.*

Rev. Lett., **77**:438, 1996.

26. Yumian Su, Gian Franco Bonini, and Kenneth Lane. Tevatron constraints on topcolor assisted technicolor. *Phys. Rev. Lett.*, **79**:4075, 1997.

27. The DØ Collaboration. Search for Heavy Neutral Gauge Bosons at CDF. Paper contributed to the XVII International Symposium on Lepton Photon Interactions, Hamburg, Germany, 1997.

28. Some accelerator parameters can be found on the WWW at the URL address: http://www-fermi3.fnal.gov/.

29. A www primer on the Fermilab accelerator complex, *Concepts Rookie Book*, can be found at the URL address: http://www-bd.fnal.gov/operations/-rookie_books/concepts/ conceptstoc.html.

30. A www primer on antiproton production and cooling, *Pbar Rookie Book*, can be found at the URL address: http://www-bd.fnal.gov/operations/rookie_books/-pbar_book/ contents.html.

31. F. Abe et al. The CDF Detector: an overview. *Nucl. Inst. Meth. Phys. Res.*, **A271**:387, 1988.

32. D. Amidei et al. SVX′: The New CDF Silicon Vertex Detector. *Nucl. Inst. Meth. Phys. Res.*, **A360**:137, 1995.

33. B. Todd Huffman, personal communication, May 20, 1997.

34. F. Bedeschi et al. Design and construction of the CDF Central Tracking Chamber. *Nucl. Inst. Meth. Phys. Res.*, **A268**:50, 1988.

35. L. Balka et al. The CDF Central Electromagnetic Calorimeter. *Nucl. Inst. Meth. Phys. Res.*, **A267**:272, 1988.

36. Y. Fukui et al. The CDF End Plug Electromagnetic Calorimeter Using Conductive Plastic Proportional Tubes. *Nucl. Inst. Meth. Phys. Res.*, **A267**:280, 1988.

37. S. Bertolucci et al. The CDF Central and Endwall Hadron Calorimeter. *Nucl. Inst. Meth. Phys. Res.*, **A267**:301, 1988.

38. J. Jackson and J. Crawford, Fermilab's Collider Run I, FermiNews, Volume 19, No. 5, page 6, March 8, 1996.

39. D. Amidei et al. A Two Level Fastbus Based Trigger System for CDF. *Nucl. Inst. Meth. Phys. Res.*, **A269**:51, 1988.

40. Robert Harris, personal communication, May 7, 1996.

41. T. Akesson et. al. Direct evidence for the emergence of jets in events triggered on large transverse energy in pp collisions at $\sqrt{s} = 63$ GeV. *Phys. Lett. B*, **118B**:185, 1982.

42. M. Banner et. al. Observation of very large transverse momentum jets at the CERN $p\bar{p}$ collider. *Phys. Lett. B*, **118B**:203, 1982.

43. F. Abe et al. Topology of three-jet events in $p\overline{p}$ collisions at $\sqrt{s} = 1.8\,\mathrm{TeV}$. *Phys. Rev. D*, **45**:1448, 1992.

44. Nathan Eddy. New Relative Jet Corrections for Run IA and IB data. CDF/ANAL/JET/CDFR/3534, 1996.

45. Brenna Flaugher and Louis Keeble. New Jet Correction Function QDJSCO Version 2.0. CDF/ANAL/JET/CDFR/1513, 1991.

46. W.-M. Yao et al. Studies of the gluon radiation systematic with $b\overline{b}$ events and a proposal for a jet energy correction based on multiple underlying events. CDF/ANAL/TOP/CDFR/3257, 1995.

47. F. Abe et al. Measurement of Dijet Angular Distributions at CDF. *Phys. Rev. Lett.*, **77**:5336, 1997.

48. Anwar Bhatti. A few more studies for the Inclusive Jet Cross Section from the 1992-1993 data set. CDF/ANAL/JET/CDFR/3003, 1995.

49. R.K. Ellis, W.J. Stirling and B.R. Webber, *QCD and Collider Physics*, Cambridge University Press, 1996, page 254.

50. F. Abe et al. Dijet Angular Distributions from $p\overline{p}$ Collisions at $\sqrt{s} = 1.8\,\mathrm{TeV}$. *Phys. Rev. Lett.*, **62**:3020, 1989.

51. V. Barger and R. Phillips, *Collider Physics*, Addison Wesley Publishing Company, 1987, page 298.

52. R.K. Ellis, W.J. Stirling and B.R. Webber, *QCD and Collider Physics*, Cambridge University Press, 1996, page 248.

53. H. Wenzel. The Primary Interaction Vertex. CDF/ANAL/SECVTX/-CDFR/4066, 1997.

54. B-Tag Working Group. Update of SECVTX Tagging in Run 1B Data. CDF/DOC/SEC_VTX/CDFR/3178, 1995.

55. B-Tag Working Group. A Seed Vertexing b-Tag Algorithm for Top. CDF/DOC/SEC_VTX/CDFR/2716, 1994.

56. B-Tag Working Group. Top Search in Lepton + jets with SECVTX. CDF/DOC/TOP/CDFR/2989, 1995.

57. A. Yagil A. Caner, A. Mukherjee. Tracking Efficiency for Soft Lepton Tagging. CDF/DOC/TOP/CDFR/2363, 1993.

58. G. Unal. Tracking Efficiency and SVX scale factor. CDF/DOC/TOP/CDFR/-3563, 1995.

59. C. Miao and W. Yao. SECVTX tagging study with track-finding degradation. CDF/ANAL/TRACKING/CDFR/3542, 1996.

60. Physical Review D, Particles and Fields, Review of Particle Properties, Volume 54, 1 July 1996, pages 31-35.

61. P. Koehn. Measurement of the Heavy Flavor Content of Jets in $p\overline{p}$ Collisions at $\sqrt{s} = 1.8$ TeV. Ph.D. thesis, University of Rochester, 1996.

62. M. L. Mangano and S. Frixione. Heavy Quark Jets in Hadronic Collisions. *Nucl. Phys. B*, **483**:321, 1997.

63. For a detailed discussion of the maximum likelihood method, see for example; Louis Lyons, *Statistics for nuclear and particle physics*, Cambridge University Press, 1986.

64. F. James. MINUIT Version 94.1 Function Minimization and Error Analysis. CERN Program Library Long Writeup D506, 1994.

65. E. Buckley-Geer. Measurement of the fully corrected ΣE_T^{jet} cross-section using the full Run 1 data sample. CDF/DOC/JET/CDFR/3995, 1997.

66. S. Behrends. A Plot of the Sytematic Uncertainty on Jet E_T. CDF/ANAL/-JET/CDFR/3550, 1996.

67. S. Behrends and A. Garfinkel. Xt Scaling (Updated): Comparison of Jet Production at $\sqrt{s} = 546$ and 1800 gev. CDF/ANAL/JET/CDFR/1650, 1992.

68. C. Grosso-Pilcher. Luminosity for Run 1B: how well do we know it? CDF/PHYS/CDF/CDFR/4350, 1997.

69. F. Abe et. al. Search for New Particles Decaying to Dijets at CDF. *Phys. Rev. D*, **55**:5263, 1997.

70. Torbjörn Sjöstrand. PYTHIA 5.6 and JETSET 7.3: Physics and manual. CERN-TH-6488-92, 1993.

71. Jonathan Lewis, personal communication, June 26, 1998.

72. M. Shapiro et. al. A beginners guide to QFL. CDF 1810, 1992.

73. B-Tag Working Group. The SVX' MC simulation. CDF/TOP/DOC/-PUBLIC/2946, 1995.

74. H.L. Lai et. al. (the CTEQ Collaboration). Global QCD Analysis and the CTEQ Parton Distributions. *Phys. Rev. D*, **51**:4763, 1995.

75. H.L. Lai et. al. (the CTEQ Collaboration). Improved Parton Distributions from Global Analysis of Recent Deep Inelastic Scattering and Inclusive Jet Data. *Phys. Rev. D*, **55**:1280, 1997.

76. F. Abe et al. Inclusive jet cross section in $p\bar{p}$ collisions at $\sqrt{s} = 1.8$ TeV. *Phys. Rev. Lett.*, **77**:438, 1996.

77. A.D. Martin W.J. Stirling and R.G. Roberts. Parton distributions of the proton. *Phys. Rev. D*, **50**:6734, 1994.

78. M. Glück E. Reya and A. Vogt. Parton distributions for high-energy collisions. *Z. Phys. C*, **53**:127, 1992.

APPENDICES

APPENDIX A: DATA SAMPLE

For this analysis, we made a sample of events passed by the JET 20, 50, 70, and 100 triggers in Run 1B that we filtered to fit on 9 Gbytes of disk space. The entire sample of Run 1B jet data is available on 73 8 mm tapes. For each event the dijet mass, defined to be the mass of the two jets with the largest corrected E_T when clustered with a cone size of 0.7 using the four vector definition:

$$m = \sqrt{(E_1 + E_2)^2 - (\vec{P}_1 + \vec{P}_2)^2} \tag{A.1}$$

and $|\cos\ \theta^*|$, where

$$\cos\ \theta^* \equiv\ \tanh\ \eta^* =\ \tanh\left(\frac{\eta_{jet_1} - \eta_{jet_2}}{2}\right), \tag{A.2}$$

was calculated. To allow flexibility, the cuts placed on these variables when compiling the data sample were roughly 10% lower than the cuts we anticipated using in the analysis. Those events satisfying:

- $|\cos\ \theta^*| < 0.70$
- minimum dijet mass:
  - 130 GeV for Jet 20
  - 217 GeV for Jet 50
  - 263 GeV for Jet 70
  - 349 GeV for Jet 100

were written to disk.

As a cross check of this data sample, we reproduced the Run 1B dijet mass spectrum used in a similar search for particles decaying to (untagged) dijets [69] from this data sample. The total number of events in the two spectra agreed to within 1.4%, where the spectrum generated from the data sample described here had the greater number of events.

APPENDIX B: MONTE CARLO PROGRAMS

The simulation of physics processes requires the evaluation of integrals with large numbers of variables which make it impossible to simulate events from first principles. Event generation for comparisons between theory and experiment are thus made by computer programs which are tuned on existing data and use as an input everything we know about parton distributions, fragmentation, scattering, and initial and final state radiation. Many event generators are available for the simulation of hadron collisions, which differ in their treatment of some of the more poorly understood ingredients in the calculation, such as fragmentation. Unless otherwise stated in the text, all simulations appearing in this document were generated using PYTHIA where the CLEO Monte Carlo, QQ, was used to decay heavy flavor quarks and a CDF detector simulation, QFL, was used to simulate the detector response. A brief description of each of these packages is given below.

PYTHIA

PYTHIA [70] is an event generator based on the Lund, or "string model" of fragmentation which includes color coherence effects. We use PYTHIA version 5.6.

QQ

QQ is a Monte Carlo developed for the CLEO experiment to simulate the decay of bottom and charmed hadrons. It is tuned on CLEO measurements of the $\Upsilon(4S)$ and is found to accurately reproduce the particle multiplicity and momentum spectra in heavy flavor decays [71]. To use it here, we remove all of the particles in the decay chain of a B-hadron from the event history and subsequently redecay it using QQ. Here we use QQ version 901.

QFL

QFL is a detector simulation package which parameterizes detector response instead of deriving it from first principles [72]. This saves considerable CPU time, making it ideal for high statistics studies.

The SVX Monte Carlo

The simulation of the silicon vertex detector [73] is based on a response parameterization derived from real data, which is found to accurately reproduce low level quantities used in signal formation such as pulse height and charge profiles (the distribution of charge among firing readout strips in a hit). Variations within the detector are determined from a database of actual noise values, hardware threshhold settings and a list of dead, inefficient, and noisy channels.

APPENDIX C: PARTON DISTRIBUTION FUNCTIONS

In order to simulate the physics of hadron collisions, it is first necessary to know the probability of finding a parton within the hadron carrying a fraction x of the parton momentum. The absolute normalization of these functions is not constrained by perturbative QCD, but if the distribution can be determined at one value of the 4-momentum-transfer, Q, they can be calculated at other values by evolution. Several collaborations have attempted to parameterize these functions by fitting to experimental results, generally using functions of the form

$$f(x;\mu) = Ax^B(1-x)^C F(x) \tag{C.1}$$

that are constrained to obey flavor and momentum sum rules, where there is one function for each type of parton, and $F(x)$ is a smooth function of x. These parton distribution functions are constantly being revised as new data becomes available, and new "sets" are calculated.

CTEQ[74] (The CTEQ collaboration) CTEQ2L is the default set of parton distributions used in this analysis ("L" indicates a leading order calculation and "M" a next-to-leading order calculation.). The CTEQ2 set was the second to come from the CTEQ collaboration. The first, CTEQ1, was based on data available at the end of 1992. The CTEQ2 analysis was performed in response to new data from HERA which extended the measured range of x by two orders of magnitude. CTEQ4 [75] is the latest set, released in 1996, to come from the CTEQ collaboration. CDF recently observed an excess of high E_T jets [76]. This prompted the CTEQ collaboration to attempt a new fit giving additional weight to the high E_T jet data to see if an underestimate of the gluon density at high x could explain the discrepancy between the high E_T jets and the data. The result of that effort is the CTEQ4HJ parton distributions.

For comparison, we also use parton distribution sets from other collaborations: **MRS**[77] (Martin, Roberts, and Stirling), **GRV**[78] (Glück, Reya, and Vogt). The distribution of the up quark momentum as parameterized by several different sets is shown in Figure C.1

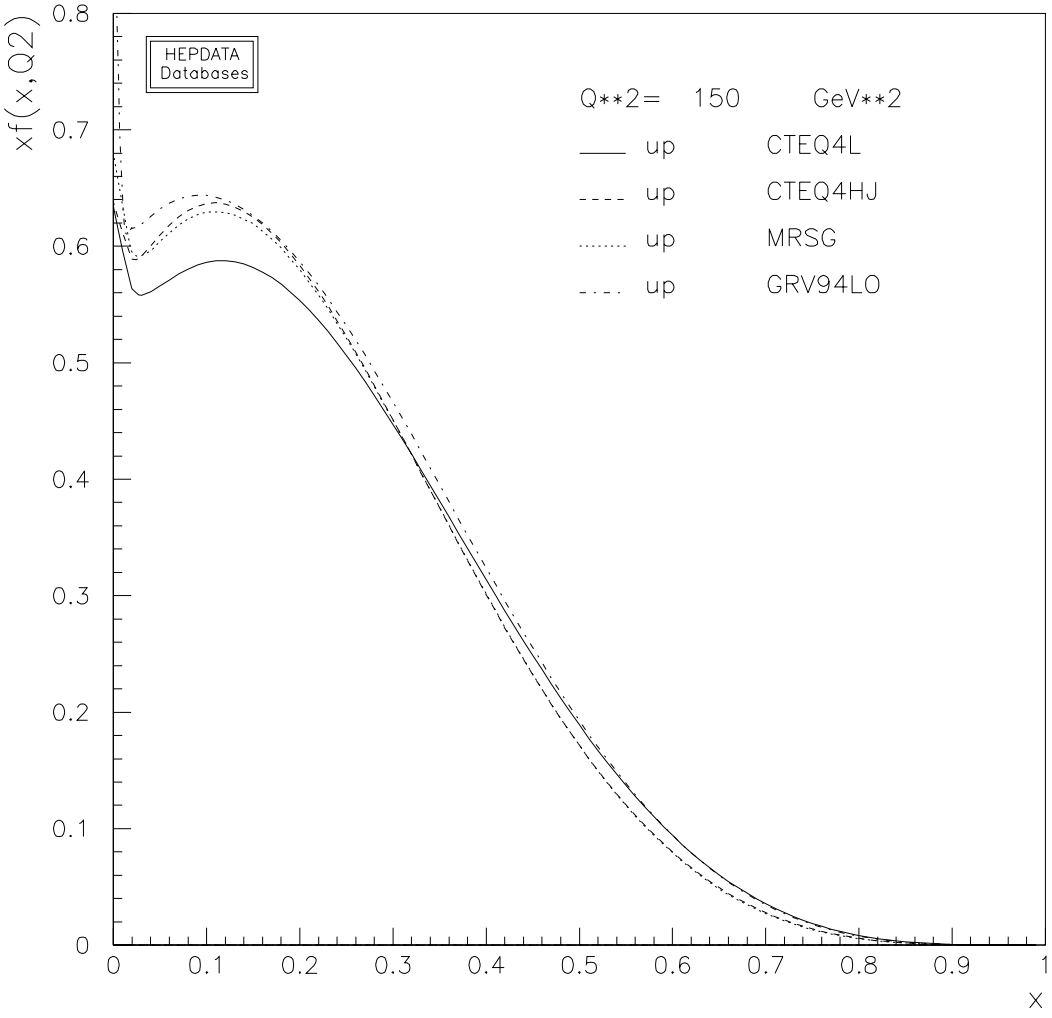

Figure C.1

A comparison of the parameterization of the momentum distribution up quarks in a proton expressed as a fraction of the proton's total momentum, x, using fits from different collaborations. Note that the distribution has a slightly different shape for each.

VITA

VITA

Kara Hoffman was born December 4, 1970 in Cincinnati, Ohio, and was raised in Miami, Florida and Lexington, Kentucky. She graduated from Tates Creek High School, Lexington, Kentucky, in 1988. She attended the University of Kentucky from 1988-1992 where she worked as a research assistant in the electrical engineering and physics departments while studying for a B.S. in physics. She subsequently accepted a fellowship to pursue graduate study in physics at Purdue University where she received her M.S. in 1994 and her Ph.D. in experimental high energy physics in 1998.